UNIVERSIDAD DE GRANADA

Tesis doctoral

Julio 2010

High angular resolution study of the earliest stages of star formation

[PhD THESIS]

Carlos Carrasco González

Instituto de Astrofísica de Andalucía (CSIC)

Memoria de Tesis

presentada en la Universidad de Granada

para optar al grado de Doctor en Física

Director de tesis:

Guillem Anglada Pons

A mis padres.

Agradecimientos

El trabajo de Tesis que aquí se presenta es el resultado de 4 años de trabajo. Afortunadamente, durante todo este tiempo nunca he estado solo. Muchas personas han participado de este trabajo. Algunas las he ido encontrando en el camino, otras siempre han estado ahí. A todas estas personas les agradezco sinceramente todo el apoyo que me han brindado.

A mi director de Tesis, Guillem Anglada, por haberme introducido en el mundo de la radioastronomía, por todos los conocimientos que me ha transmitido, y por la inmensa ayuda que me ha prestado en todo momento durante la realización de este trabajo, que es tan suyo como mío.

A Luis Felipe Rodríguez, con quien he tenido la gran suerte de trabajar estrechamente, por hacer tan fáciles, cosas que parecían tan complicadas.

A todas las personas que, con su colaboración, han hecho posible la escritura de muchas de las páginas de esta Tesis: Antxon Alberdi, José Fco. Gómez, Rosario López, Josep Martí, Mayra Osorio, José María Torrelles.

A mis compañeros del IAA; A los miembros del Triunvirato: Darío, Dani y Miguel Ángel, por todas las discusiones "científicas" que hemos tenido, siempre, en la barra de un bar, siempre, sobre "la vida"; A Omaira, por seguir estando ahí; A las niñas del 547: Yoli y Tere (Amparito!!), por cuidarme a Gaby; A la (ahora) niña del 598: Martiña, por ser única. A Juanma, por compartir conmigo sus reflexiones sobre... sobre todo.

A toda las personas del CRyA, que me hicieron tan fácil el estar tan lejos de casa: Karla Álamo, Roberto Galván, Yolanda Gómez, Vicente Hernández, Jesús Toalá, Rosy Torres.

A mis padres, quienes, con su apoyo incondicional, son los verdaderos responsables de que yo esté escribiendo esto hoy. Y a mi hermanita!!, que creo que es la persona que más ha creido en mí.

Y por último, gracias a tí, Gabriela, por haberte cruzado en mi camino, por haber decidido recorrerlo conmigo haciéndolo infinitamente más fácil, por hacerme reír cuando lo necesito, y en definitiva, por hacerme tan feliz compartiendo tu vida conmigo.

<div align="right">

Carlos Carrasco González,

9 Julio de 2010

</div>

Resumen

En esta Tesis se presenta un estudio observacional con alta resolución angular de las primeras etapas de la formación estelar, con especial énfasis en el fenómeno de los jets y de los discos protoplanetarios. El estudio se ha realizado mediante observaciones obtenidas con los radiointerferómetros Very Large Array (VLA), Combined Array for Research in Millimeter-wave Astronomy (CARMA), y Sub-Millimeter Array (SMA). Se han estudiado cinco regiones de formación estelar: dos regiones de formación estelar de baja masa (L723 y HL/XZ Tau), una región de formación estelar de masa intermedia (NGC 2071) y dos regiones de formación de alta masa (W 75 N y HH 80-81).

Hemos llevado a cabo observaciones de alta resolución angular con el VLA a 3.6 cm y 7 mm hacia la región del flujo molecular multipolar en L723, donde hemos encontrado un sistema múltiple de objetos estelares jóvenes en una región con una extensión de sólo 1200 UA. Dos de estos objetos (VLA 2A y VLA 2B) forman un sistema binario con una separación de 90 UA. Hemos propuesto que el flujo molecular multipolar de CO observado en L723 podría ser el resultado de la superposición de, al menos, tres flujos bipolares independientes, impulsados por tres objetos jóvenes distintos. Nuestras observaciones sugieren que VLA 2A está asociada con un radiojet y que es la fuente que impulsa el sistema de objetos Herbig-Haro (HH) previamente detectado en la región, así como uno de los flujos moleculares de CO. Proponemos que VLA 2B es la fuente que impulsa el segundo flujo de CO. Finalmente, un tercer flujo de CO parece ser un flujo "fosil" cuya fuente de energía no ha estado muy activa en el pasado reciente.

Observamos la emisión de polvo a 7 mm asociada con la estrella joven HL Tau. Esta emisión parece provenir de un disco con un radio de $\sim$25 UA. En este disco, hemos detectado un hueco a un radio de $\sim$10-15 UA (similar al radio de la órbita de Saturno) que podría ser un signo de la formación de un protoplaneta. Estas observaciones también han puesto de manifiesto que la estrella joven XZ Tau, que había sido previamente identificada como un sistema binario con una separación de 42 UA, es realmente un sistema triple, ya que nuestras observaciones han resuelto una de las dos componentes en un sistema binario de 13 UA. Hemos propuesto que la eyección de gas observada con el HST en esta estrella puede estar relacionada con el paso por el periastro de las componentes del nuevo sistema binario.

Estudiamos la emisión en el rango centimétrico (libre-libre) y milimétrico (polvo) de las fuentes infrarrojas en el centro de la región de formación estelar NGC 2071. La emisión de la fuente IRS 1 presenta una morfología alargada con protuberancias en ambos extremos. Hemos interpretado esta fuente como un radiojet que interacciona fuertemente con el medio o, alternativamente, como dos radiojets impulsados por un sistema binario. Nuestras observaciones de mayor resolución angular del centro de la emisión muestran un indicio de una fuente doble, lo que sugiere la posible presencia de un sistema binario. La emisión en el centimétrico de la fuente IRS 3 en NGC 2071, traza un radiojet ionizado, mientras que la emisión en el milimétrico traza un disco circunestelar orientado perpendicularmente al jet. Esta orientación de la emisión milimétrica coincide con la orientación de los máseres previamente observados por Torrelles et al., y que fueron interpretados como un disco de acreción circunestelar. Hemos modelado la

emisión del polvo del disco de acreción, lo que nos ha permitido restringir el radio y la tasa de acreción del disco, así como la masa de la estrella central.

Hemos estudiado la naturaleza y el entorno de las fuentes de radio en la región W 75N. Nuestros resultados apoyan fuertemente que la fuente VLA 3 es un radiojet asociado con un objeto estelar joven. Hemos detectado importantes variaciones en la densidad de flujo, morfología y posición de la fuente Bc, lo que sugiere que esta radiofuente no está trazando una estrella independiente, sino que es realmente un objeto HH impulsado por VLA 3. Si nuestra interpretación es correcta, éste es uno de los objetos HH radio más intensos conocidos hasta ahora. Nuestras observaciones de la emisión molecular de amoníaco a gran escala muestran que la formación estelar en W 75 N podría estar desencadenada por la colisión de dos nubes moleculares filamentarias.

Hemos observado la fuente que impulsa el jet HH 80-81 con el VLA y el SMA. Hemos detectado emisión de la molécula de SO que sugiere la presencia de gas molecular orbitando en torno a ella. A partir de estas observaciones, estimamos un límite inferior de 17 $M_\odot$ para la masa central. La densidad de flujo y morfología cuadrupolar de la emisión a 7 mm asociada con la fuente de energía del jet, sugiere que es una combinación de emisión libre-libre del radiojet y emisión de polvo de un disco circunestelar perpendicular al jet. Hemos modelado con éxito la emisión a 7 mm como un disco de acreción con un radio de 420 UA, una tasa de acreción de 7×10^{-6} $M_\odot$ yr^{-1} y una masa de 14 $M_\odot$ orbitando alrededor de una estrella de 10 $M_\odot$.

Hemos realizado observaciones de muy alta sensibilidad a 6 cm del jet de HH 80-81 que revelan que la emisión en los lóbulos del jet situados a $\sim$0.5 pc de la fuente central, está linealmente polarizada, confirmando su naturaleza como radiación sincrotrón, lo que implica la presencia de electrones relativistas y un campo magnético asociado con el jet. A partir de nuestras observaciones hemos podido inferir la estructura del campo magnético en el jet de HH 80-81, de modo análogo a como se hace en los jets extragalácticos, que se caracterizan por su intensa emisión sincrotrón. Nuestro descubrimiento de radiación sincrotrón en un jet asociado a una estrella joven representa un paso importante en la unificación del fenómeno de los flujos colimados observado que se observa en muchos contextos astrofísicos.

Summary

In this thesis, we present an observational, high angular resolution study of the earliest stages of the star formation process, with a special emphasis in the phenomena of jets and protoplanetary disks. This study has been performed mainly from observations carried out with the radio interferometers Very Large Array (VLA), Combined Array for Research in Millimeter-wave Astronomy (CARMA), and Sub-Millimeter Array (SMA). We have studied five star-forming regions: two regions of low-mass star formation (L723 and HL/XZ Tau), one region of intermediate-mass star formation (NGC 2071), and two regions of massive star formation (W 75N and HH 80-81).

We carried out VLA high angular resolution continuum observations at 3.6 cm and 7 mm towards the core of the L723 multipolar outflow. We found a multiple system of four radio sources suspected to be young stellar objects (YSOs) in a region of only 1200 AU in extent. Two of these objects (VLA 2A and VLA 2B) form a close binary system of YSOs with a separation of ∼90 AU. We propose that the multipolar CO molecular outflow observed in L723 could result from the superposition of at least three independent bipolar outflows, driven by three different YSOs. Our observations suggest that VLA 2A is associated with an ionized radio jet, and that it is the driving source of the system of Herbig-Haro (HH) objects, as well as of one of the bipolar CO outflows. We propose VLA 2B as the driving source of the second CO outflow. Finally, the third CO outflow, seems to be a "fossil" outflow whose exciting source has not been very active in the recent past.

We observed the dust emission at 7 mm associated with the young star HL Tau. This emission seems to be arising in a clumpy disk with radius of ∼25 AU. We found a density gap in the disk at a radius of ∼10-15 AU (similar to the radius of the orbit of Saturn) that may be the signpost of a growing protoplanet. Our observations also show that the young star XZ Tau, known to be a binary with 42 AU separation, is actually a triple star system. We propose that the remarkable ejection of gas from the XZ Tau system observed with the HST may be related to a periastron passage of our newly discovered close binary system.

We studied the centimeter (free-free) and millimeter (dust) emission of the IR sources at the center of the NGC 2071 star-forming region. The centimeter emission of source IRS 1 presents an elongated morphology with protuberances at both edges. We interpret this source as a radio jet with strong interactions with the ambient medium or, alternatively, as two radio jets emerging from a close binary. Our highest angular resolution image of the core of the emission shows a hint of a double source, suggesting that a binary system could be present. The centimeter emission of source IRS 3 in NGC 2071 traces an ionized radio jet, while the millimeter emission traces a circumstellar disk of dust oriented perpendicular to the jet. The orientation of the millimeter emission coincides with that of the maser spots previously observed by Torrelles et al., that were also interpreted as tracing a circumstellar accretion disk. A modelling of the dust emission as an accretion disk allowed us to constrain the radius and accretion rate of the disk and the mass of the central star.

We studied the nature and molecular environment of the radio sources in the W 75N region.

Our results strongly support that source VLA 3 is a radio jet associated with a YSO. We detect important changes in total flux density, morphology, and position in the source Bc, suggesting that it is not tracing an independent star but actually is a radio HH object powered by VLA 3. If our interpretation is correct, this is one of the brightest radio HH objects known so far. Our observations of the large-scale molecular ammonia emission show that the star formation in W 75 N could be triggered by the collision of two filamentary molecular clouds.

We observed the driving source of the HH 80-81 jet with the VLA and the SMA. We detected SO emission that suggests the presence of molecular gas orbiting around the driving source of the jet. From these observations, we estimate a lower limit to the central binding mass of 17 $M_{\odot}$. We interpreted the 7 mm emission associated with the driving source of the HH 80-81 jet as a combination of free-free emission from the radio jet, and thermal dust emission from a perpendicular, circumstellar disk. After substraction of the free-free emission, we successfully modeled the 7 mm emission as arising from an accretion disk with a radius of 420 AU, an accretion rate of 7×10^{-6} $M_{\odot}$ yr^{-1}, and a mass of 14 $M_{\odot}$, orbiting around a 10 $M_{\odot}$ protostar.

We performed sensitive observations at 6 cm wavelength of the HH 80-81 jet revealing that the emission in the jet lobes, at $\sim$0.5 pc from the driving source, is linearly polarized. The detection of linearly polarized emission confirms its synchrotron nature, implying the presence of relativistic electrons and a magnetic field associated with the radio jet. Following procedures similar to those used for extragalactic radio jets, that are characterized by strong synchrotron emission, we inferred the structure and strength of the magnetic field in the HH 80-81 jet. Our discovery of synchrotron radiation in a jet from a YSO represents an important step in the unification of the collimated outflow phenomena observed in many astrophysical contexts.

.

Index

8 Conclusions 101

.

1

Introduction

Stars are formed in the coldest and densest regions of the interestellar medium, the molecular clouds, which consist of dust and gas. Due to the high extinction in these regions, the process of star formation cannot be observed by optical telescopes. It is for this reason that most of the advances in its study have been carried out in the last few decades, when a important improvement of the techniques of observation at radio and infrared wavelengths took place.

Stars form via gravitational collapse of fragments of the molecular cloud. A dense central object is then formed, the protostar, which continues accreting material from its surrounding envelope. Surprisingly, this process has proven to be much more complex and dynamic than expected beforehand, with an important interaction between the star and its surroundings. The consequences of this interaction are reflected, for example, in the association of the young stellar objects with powerful collimated ejections of material (jets). Now, it is well known that these jets are a natural consequence of the star formation process. It is through these ejections of material that the protostar can remove the excess of angular momentum (consequence of the initial rotation of the cloud) which otherwise would make the star to rotate too fast and to disintegrate. Another consequence of the initial rotation is that part of the material will be accumulated in an equatorial disk orbiting around the star. These disks, which are intimately related to the presence of the jets, would be the precursors of the planetary systems. In this way, the interest in the star formation process have been displaced from the study of the protostar itself, towards the study of its environment: jets and protoplanetary disks.

1.1   The Current Picture of Star Formation

1.1.1   Low-Mass Star Formation

Low-mass stars appear to form from gravitationally bound cores in molecular clouds. The theoretical works of Shu (1977, 1987) described the formation of a star from the gravitational collapse of isothermal spherically symmetric cores. This theory is usually taken as an idealized scheme for the formation of a star. In Shu's theory, one assumes that the cores have initially a density distribution of a singular isothermal sphere, $\rho = c_s^2/(2\pi G r^2)$, where c_s is the sound

speed. The collapse is initiated at the center, and the point at which the gas begins to fall inward propagates outward at the sound speed as an expansion wave: $R_{ew} = c_s t$. This solution is therefore named as inside-out collapse. For $r \geq R_{ew}$, the density is that of a singular isothermal sphere, while for $r < R_{ew}$, the gas accelerates until it reaches free fall, with $v = (2Gm_*/r)^{1/2}$ and $\rho_0 \propto r^{-3/2}$. The infall rate for Shu's expansion wave solution is constant in time,

$$\dot{M}_{in} = 0.975 c_s^3/G = 1.54 \times 10^{-6}(T/10\,K)^{3/2}\,M_\odot\,\mathrm{year}^{-1}, \tag{1.1}$$

and it is characterized by a single parameter, the sound speed. At the center, the collapsed gas forms a protostellar core whose mass is linearly increased with time, $M_*(t) = \dot{M}t$. The infalling material is slowed and thermalized in an accretion shock at the surface of the protostellar core. As the material releases gravitational potential energy, the luminosity of the protostellar core is increased with time:

$$L_*(t) = \frac{GM_*(t)\dot{M}}{R_*}, \tag{1.2}$$

where R_* is the radius of the protostellar core, which is assumed to remain constant with a value $R \simeq 5R_\odot$.

In general, accretion will not be spherical since the initial turbulence in molecular clouds leads to rotation of the cores. The effect of the rotation is negligible at the external layers of the cloud, where the collapse remains parallel to the radial direction and indistinguishable from a non-rotating case. However, as the infalling material is closer to the center, due to conservation of angular momentum, the trajectories will be curved. Therefore, the material does not fall directly to the star, but it follows parabolic trajectories and incorporates to an equatorial disk from which the accretion continues (Terebey et al. 1984; Shu et al. 1987).

The scheme described above predicts that a stellar object when first formed has a very small mass ($\sim$0.05 $M_\odot$). This implies that the star must acquire most of its final mass by accretion from the envelope through the accretion disk. Then, the protostar will evolve from a situation in which it is surrounded by large amounts of gas and dust to a situation in which most of the envelope has been incorporated to the protostar.

Observationally, the mass and temperature distribution on both small and large spatial scales can be inferred by modeling the spectral energy distribution (SED). SEDs of YSOs are divided into four classes, that correspond to four different evolutionary stages (see Figure 1.1). Lada (1987) and Adams, Lada & Shu (1987) introduced three different classes (Classes I, II and III) based in the slope of the SED over the wavelength range between 2.2 μm and 10-25 μm,

$$\alpha_{IR} \equiv d\log(\lambda F_\lambda)/d\log\lambda, \tag{1.3}$$

Later, André, Ward-Thompson & Barsony (1993) introduced an additional class (Class 0) and suggested that represents a phase previous to Class I. Previous to these phases where a central object has been already developed, it has been identified a starless (pre-stellar) phase.

The characteristics of these four classes can be summarized as follows:

- **Class 0:** Sources that are extremely faint in the optical and near-IR and that have a significant submillimeter luminosity. Its SED is very similar to that of a black-body with a low temperature ($\sim$10-30 K). These characteristics suggests that we are observing a cold dusty envelope around the protostar. Protostars are believed to acquire a significant fraction, if not most, of their mass in this embedded phase.

- **Class I:** Sources characterized by a positive value of α_{IR}. Its SED is wider than that of a black-body, which suggests the presence of large amounts of circumstellar dust. Such sources are believed to be relatively evolved protostars with both circumstellar disks and envelopes.

- **Class II:** Sources with $-1.5 < \alpha_{IR} < 0$. Its SED is also wider than that of a black-body, with an IR excess, but their negative slope indicates that they are surrounded by considerably less circumstellar dust than Class I sources. The stars of this class are observable in the IR and optical. Its SED can be modeled as a pre-main sequence star with a dusty circumstellar disk (classical T-Tauri stars).

- **Class III:** Sources with $-3 < \alpha_{IR} < -1.5$. Its SED is similar to that of a black-body with a single temperature, consistent with observing the photosphere of a young star. They are observable at optical wavelengths and they present very little circumstellar dust. It is believed that they are pre-main sequence stars that are no longer accreting significant amounts of matter (weak-lined T-Tauri stars). The small amount of matter in the circumstellar disk may indicates that the formation of a planetary system is in an advanced phase.

At some point in the earliest stage of the formation (Class 0), a powerful collimated wind along the rotation axis is generated. This collimated wind stops the accretion through the poles and removes part of the excess of angular momentum from the system, allowing accretion to proceed to the protostellar core (see section 1.2).

This scheme decribes the collapse of a portion of molecular cloud to form a single star. However, stars do not form isolated, but in multiple systems (Duquennoy & Mayor 1991; Mathieu 1994), and it is expected that the different components interact between them during their formation. These interactions may imply interchange of material between them, making the evolution of a single protostar quite different from the isolated case. It has been proposed, for example, that close encounters between two protostars could lead to accretion bursts in one of the protostars (Pfalzner et al. 2008).

1.1.2   High-Mass Star Formation

The scheme discussed above is valid for the formation of low-mass stars ($M_* < 8\ M_\odot$). In principle, it is tempting to think of massive star formation simply as an extension of low
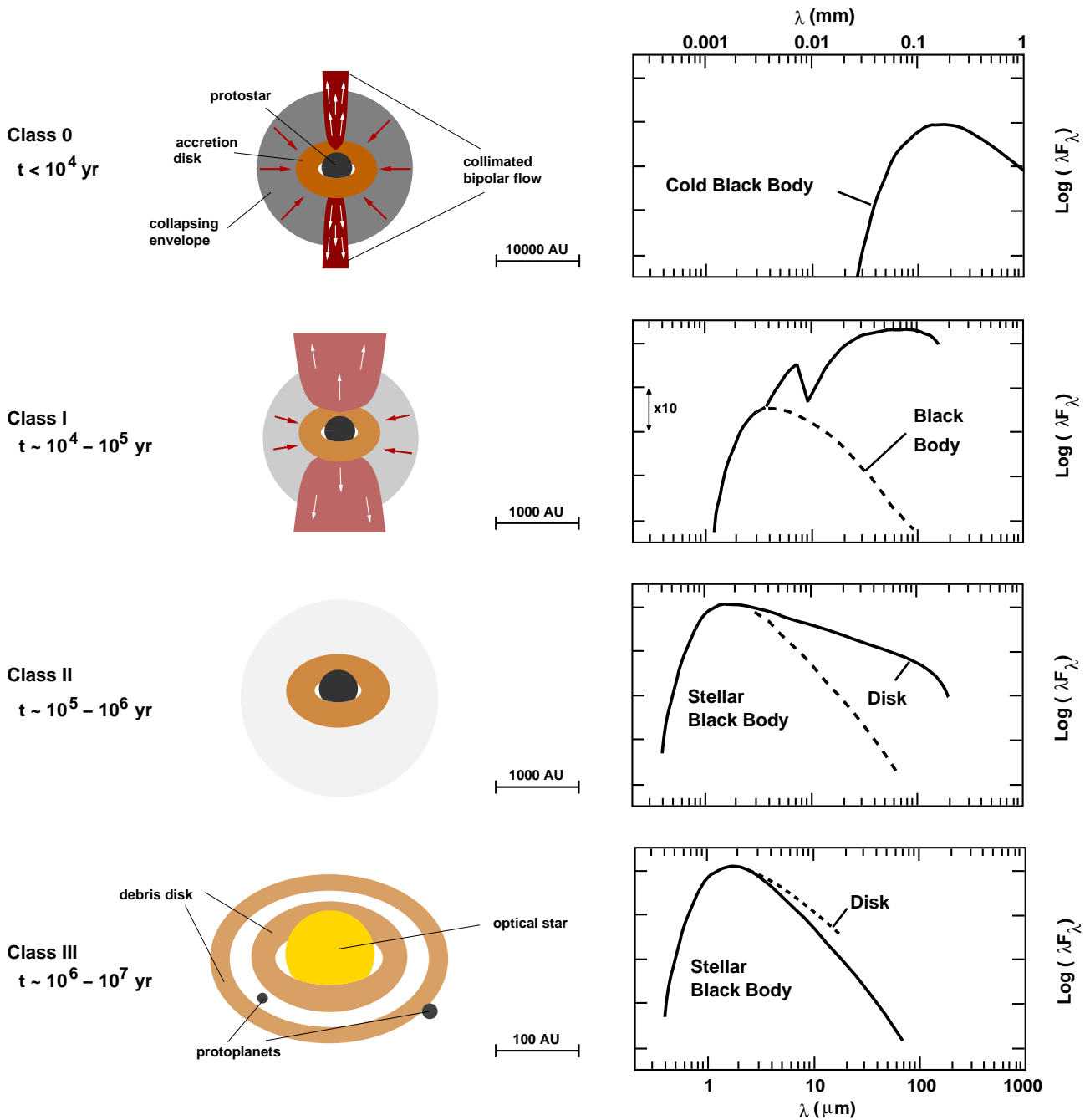
Figure 1.1 Observational classification of low-mass young stellar objects based in the shape of their SEDs. It is though that this classification represents an evolutionary scheme, and it is usually taken as a standard picture for the formation of a star. Thus, protostars would evolve from a phase in which they are surrounded by large amounts of material (Class 0) to a phase in which most of the material of the envelope has been incorporated to the star (Class III).

mass star formation. However, from a theoretical point of view, the formation of massive stars presents some differences. The main difference is that the formation of high-mass stars happens on much shorter time scales and that they reach the main sequence emitting an enormous amount of radiation before they have finished to accrete all their mass. Early spherically symmetric calculations show that the strong radiation pressure acting on dust grains can become large enough to reverse the infall of matter when the star reaches the mass of 8-10 $M_\odot$ (Wolfire and Cassinelli 1987). However, more recent calculations (Osorio et al. 1999) estimate that stars of up to $\sim$30 $M_\odot$ can be formed through this process.

Although, at present there is no clear evolutionary scheme for the formation of massive stars, several different stages have been observationally identified (Menten, Pillai & Wyrowski 2005; van der Tak & Menten 2005; Zinnecker & Yorke 2007):

- **Infrared Dark Clouds (Perault et al. 1996; Egan et al. 1998; Benjamin et al. 2003):** They are characterized by very high densities and very low temperatures. They are observed in absorption against mid-IR background emission. It is thought that these objects represent the initial conditions of high-mass star formation.

- **Hot Molecular Cores (Osorio et al. 1999; Kurtz et al. 2000; Cesaroni 2005):** They have large masses of warm and dense gas, and large abundances of complex organic molecules evaporated off dust grains. It is though that they may contain an embedded protostar, which even may have been initiated the nuclear reactions. This would represent a more advanced stage than the Infrared Dark Clouds, but they do not contain photoionized gas yet.

- **Hypercompact and Ultracompact HII Regions (Kurtz et al. 2005; Hoare et al. 2007):** They are characterized by the presence of photoionized gas that remains confined in the vicinity of the protostar. Whereas hypercompact HII regions probably represent individual photoevaporating disks (e.g., Keto 2007), ultracompact HII regions probably represent disk-less stars photoionizing their own cocoons and massive envelopes.

- **Classical HII Regions (Mezger et al. 1967; Yorke 1986):** They are characterized by gas photoionized globally, often by several ionizing sources. They expand hydrodynamically as a whole and disrupt the parent molecular cloud, revealing both the embedded high-mass and lower mass stellar populations for optical and near-IR observations (Carpenter et al. 1993; Zinnecker, McCaughrean & Wilking 1993).

Observational tests of models for the formation of high-mass protostars are even more difficult than in low-mass protostars. The reasons are their large distances (typically $\gtrsim$2 kpc), crowding, large extinctions, and the presence of nearby HII regions.

Currently three major theoretical descriptions of high mass star-formation have been proposed: monolithic collapse and disk accretion, competitive accretion, and stellar mergers (see e.g., Zinnecker & Yorke 2007):

- **Stellar Mergers:** This mechanism was proposed to overcome the radiation pressure problem. Massive stars would be formed through the collision and merging of several low-mass stars. However, stellar mergers will be rare and it is though that will be only relevant for the most massive stars in the richest young clusters (such as young globular clusters).

- **Competitive accretion:** Massive stars are mostly observed in clusters, where it is expected that stars interact dynamically. In isolated clouds, the star will accrete most of the mass of the parental cloud, which determines its final mass. In clusters, however, stars compete for cloud gas. The final mass of a star formed in a cluster depends on its accretion domain, i.e., the region from which gas can be gathered. Since the size of this domain depends on the mass of the stars, this will lead to runaway growth. Massive stars will accrete relatively more gas than low-mass stars and become even more massive, which will further increase their accretion domain. Stars formed at the center of the cluster are at an advantage, as gas falling into the potential well of the cluster increases the gas reservoir available to an individual star. Such stars become more massive than stars that form at the periphery of the cluster (e.g., Bonnell et al. 1997, 2004).

- **Monolithic collapse and disk accretion:** This would be a process similar to that described for low-mass stars: collapse of a dense core and subsequent accretion through a circumstellar disk. The difference would be that accretion is much more intense and continues after the star has reached the main-sequence. Some theoretical studies show that reduced dust opacities (Wolfire & Casinelli 1987; Osorio, Lizano, D'Alessio 1999), rotation (Nakano 1989; Yorke & Sonnhalter 2002) and/or very high accretion rates (Edgar & Clarke 2003) could overcome the radiation pressure problem. Observations of highly collimated jets and circumstellar disks in a few high-mass protostars (Martí et al. 1993; Patel et al. 2005; Rodríguez et al. 2005) also support the idea of formation through accretion disks as in the case of low-mass stars.

1.2 Mass ejection phenomena

As commented above, during the earliest stages of low-mass star formation a protostellar object builds up its mass through an accretion disk. It is observationally well established that this accretion of matter takes place simultaneously with violent ejections of matter. The most clear manifestations of outflowing gas associated with protostars are the pc-scale Herbig-Haro (HH) jets and the bipolar molecular outflows (see Figures 1.2 and 1.3).

HH objects were simultaneously discovered by Herbig (1951) and Haro (1952) as optical nebulosities in star-forming regions. They are observed in highly-excited molecular hydrogen (e.g., Eislöffel 2000), optical forbidden lines (e.g., Anglada et al. 2007), hydrogen Balmer emission lines (e.g., López 2009) and radio continuum (e.g., Pravdo et al. 1985; Torrelles et al. 1991; Martí et al. 1993). Proper motions studies of these objects reveal that they move away from a central protostar with velocities of $\sim$100-200 km s^{-1}. This indicates that they are

related to outflow phenomena. It is now widely accepted that HH objects are created when highly collimated jets driven by protostars collide with the surrounding material, generating strong shock waves that heat and ionize the gas (e.g., Reipurth & Bally 2001). Some HH objects appear with a clearly bow-shaped morphology, while in other cases they appear as a chain of optical knots. We use the term HH jets to refer to these structures. The base of these HH jets, i.e. the region closest (<100 AU) to the driving source, is usually highly extincted by circumstellar dust, and it is difficult to observe at optical or even at IR wavelengths. However, the free-free emission from ionized material of this region is frequently detectable at centimeter wavelengths (see Sect. 1.4).

Molecular outflows were first identified in the Orion A molecular cloud through CO line emission at millimeter wavelengths produced as a consequence of high-velocity molecular gas (Kwan & Scoville 1976; Zuckerman et al 1976). High-velocity CO emission was soon detected toward other objects, and the structure of the outflowing material was found to be bipolar (Snell et al 1980, Rodríguez et al 1980). Since the first surveys it was realized that these bipolar outflows are extraordinarily common around young stars (Rodríguez et al. 1982; Bally & Lada 1983; Edwards & Snell 1982, 1983, 1984). At present, at least 200 outflows have been cataloged (e.g., Wu et al. 1996).

A widely accepted interpretation is that molecular outflows are the result of the interaction of the jet with the ambient molecular gas (Raga et al. 1993). As the jet penetrates in the molecular cloud, the molecular gas is heated, dragged and pushed outwards. This gas is detected as high-velocity ($\sim$10 km s^{-1}) wings in the emission spectrum of molecular lines such as the CO. The emission at red wavelengths corresponds to gas moving away from the observer, while the emission at blue wavelengths corresponds to gas approaching to the observer.

Several studies suggest that the most powerful and most collimated outflows are related to the youngest protostars (Bontemps et al. 1996; Gueth & Guilloteau 1999; Wu et al. 2004). This indicates that, although molecular outflows are present through much of the embedded phase of protostars, outflow activity declines over the time.

Outflows are though to play an important role in star formation, since they probably remove the excess of angular momentum from the disks in order for the accretion to proceed. However, despite their importance and the extensive studies, there are still many open questions about the driving mechanism. The main reason for this is that the region where the gas is accelerated and collimated is located very near the star ($\sim$10 AU), and this region is highly obscured making its observation at optical or IR wavelengths not possible.

1.3 Disks

As commented in the previous section, a protostar acquires most of its mass through an accretion disk. The first observational signposts of disks around young stellar objects were the interestellar toroids of $\sim$0.1-1 pc detected in molecular line studies (Torrelles et al. 1983, 1994), the polarization of optical scattered light (perpendicular to the jets and outflows; Bastien & Menard 1988, 1990), and the IR excess (Strom 1995).
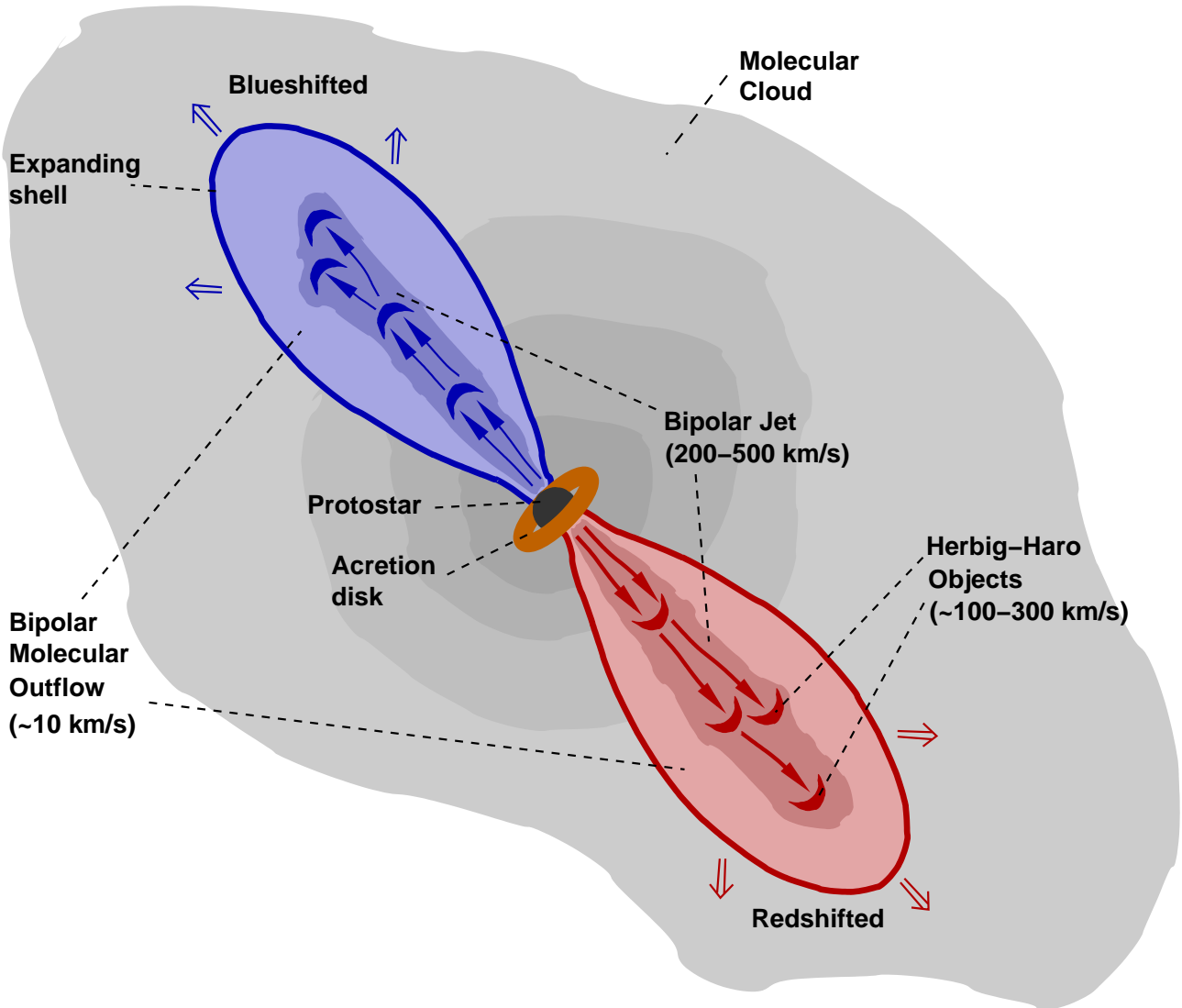
Figure 1.2 Schematic overview of the main mass ejection phenomena associated with the star formation and observed at large scales: Molecular Outflows, Collimated Jets and Herbig-Haro Objects.

With the advent of millimeter interferometers and the Hubble Space Telescope (HST), it became possible to obtain direct images of disk-like structures surrounding pre-main sequence objects. Observations of the classical T-Tauri star HL Tau at radio wavelengths resolved an elongated structure with a radius of 60-150 AU perpendicular to the optical jet (Rodríguez et al. 1992; Wilner, Ho, Rodríguez 1996). HST observations of Orion show disk-like structures seen in silhouette against the bright nebular background, with low-mass pre-main sequence stars at their centers (McCaughrean & O'Dell 1996). The HST has also imaged edge-on disks in HH 30 (Burrows et al. 1996) and HK Tau/c (Stapelfeldt et al. 1998); in these cases, the disk blocks out direct light from the star, but stellar light scattered by the disk curved atmosphere is seen as an extended nebula.

Theoretical calculations (e.g., Shu et al. 1987) predicted typical radii of the order of 100 AU, which are consistent with measured radii in Class I and Class II sources (e.g., Padgett et al. 1999; Kitamura et al. 2002). Some theoretical models suggests that Class 0 sources could
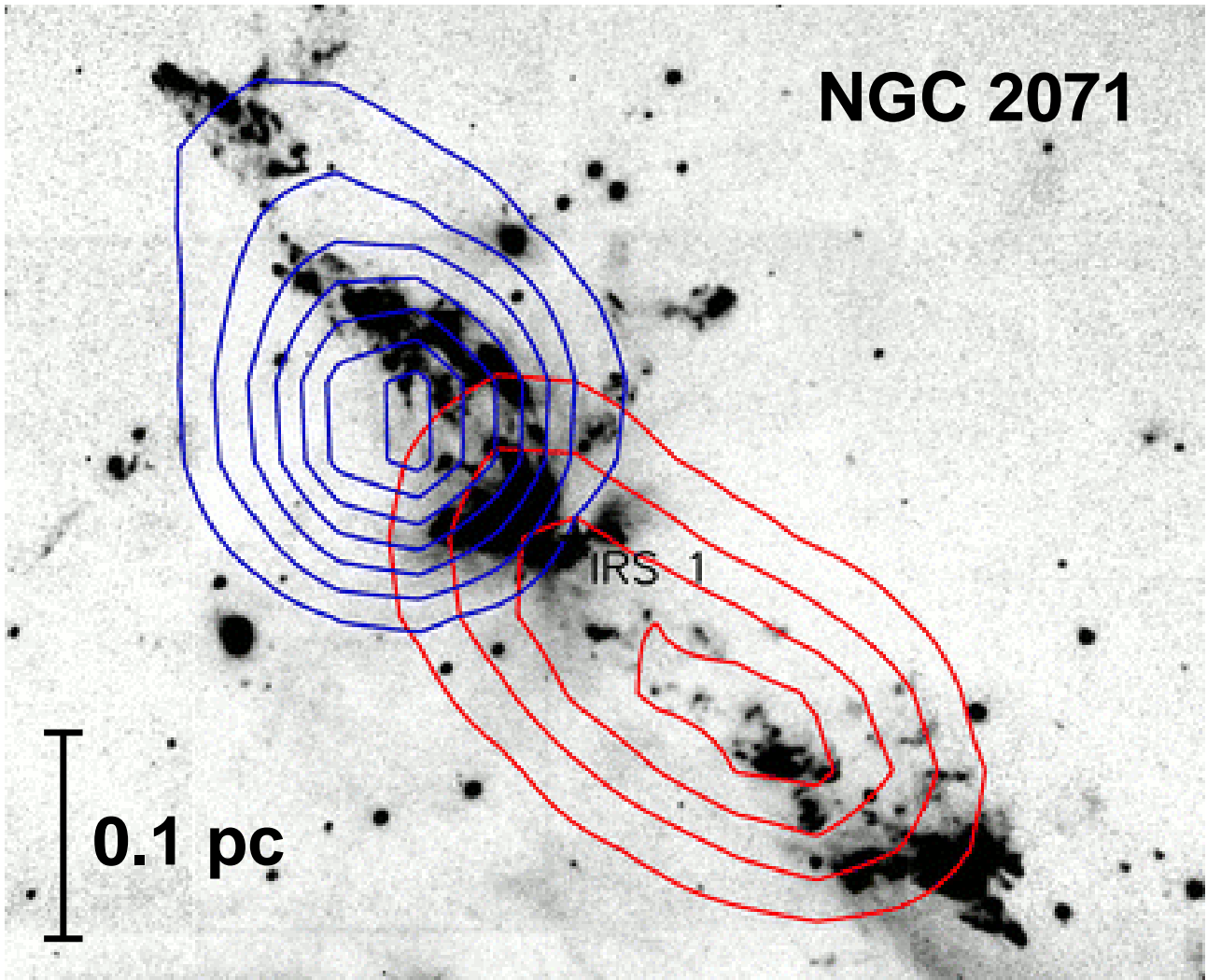
Figure 1.3 CO bipolar molecular outflow (blue and red contours indicates blushifted and red-shifted gas, respectively; Stojimirovic et al. 2008) and H_2 jet (grey scale; Eislöffel 2000) in the NGC 2071 star-forming region.

possess smaller disks (Terebey et al. 1984; Ruden & Lin 1986; Lin & Pringle 1990). However, little is known about the early stages of disk formation, largely because the disks develop deep within protostellar envelopes that are opaque except at long wavelengths. Only a handful of compact (i.e., with radii much smaller than 100 AU) disks have been imaged toward the young stars L1551 IRS 5 (Rodríguez et al. 1998; radii of 10 AU), L1527 (Loinard et al. 2002; radius of ∼20 AU), and SVS 13 (Anglada et al. 2004; radius of ∼30 AU). However, in these cases a nearby companion has always been found that could be making the disks small by tidal truncation. It is also noticeable that a circunbinary disk with a radius of ∼250 AU has been imaged in GG Tau (Guilloteau et al. 1999).

It is yet unclear if massive protostars also develop accretion disks similar to those of low-mass. Elongated structures have been detected toward several massive protostar, but with radii of several thousands of AU (Cesaroni 2005). So far, only a few compact accretion disks have been detected around massive protostars (Shepherd et al. 2001; Patel et al. 2005; Torrelles et al. 2007).
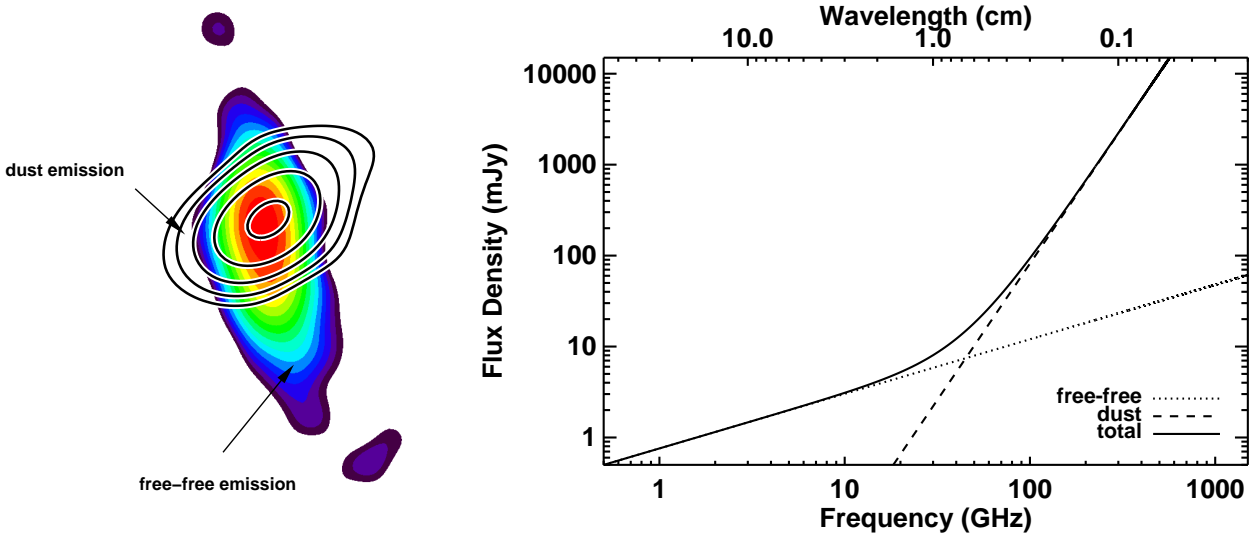
Figure 1.4 **(Left)** An image of the disk (contours) and radio jet (colors) associated with the YSO IRS3 in NGC 2071 (see Chapter 4). **(Right)** Typical spectral energy distribution of young stellar objects in the cm to sub-mm wavelength range. At cm wavelengths the emission is dominated by free-free thermal emission from the ionized gas in the jet. At mm and sub-mm wavelengths, the emission is dominated by thermal dust emission from the accretion disk.

1.4   Radio emission from ionized jets

In the last decades, radio continuum observations at centimeter and millimeter wavelengths have revealed as a powerful tool to study the phenomena of ionized jets and dusty disks in the earliest stages of star formation (see above). First, at these wavelengths no significant dust extinction is expected, even in the extremely dense environments where star formation takes place. Second, the high-angular resolution reachable with the large radio interferometers available at present allows the study the phenomena of disks and outflows at small scales of a few AU.

The spectral energy distributions (SEDs) of very young low-mass stellar objects (Class 0 and Class I) usually have two main contributions. At centimeter and longer wavelengths the emission is dominated by thermal free-free radiation from the ionized material in a jet, while at millimeter and shorter wavelengths it is dominated by thermal dust emission from a circumstellar disk (e.g., Rodríguez 1994; see Fig. 1.4). In several YSOs (mainly T-Tauri stars), non-thermal gyrosynchrotron emission has been detected at centimeter wavelengths (André et al. 1988, 1992; Philips, Lonsdale, & Feigelson 1993; Rodríguez, Anglada & Curiel 1999). Massive YSOs in the very early phases appear to follow a similar scheme, with a disk of dust and an ionized jet, but the number of examples is still very scarce (see next chapters). For massive YSOs in more advances stages (see Sect. 1.1.2) the centimeter emission is dominated by the strong free-free emission of the associated HII region.

The spectral index of the emission in a given wavelength range, defined as $\alpha = d \log S_\nu / d \log \nu$ ($S_\nu \propto \nu^\alpha$), where S_ν is the flux density measured at frequency ν, is a useful parameter to discriminate between different emission mechanisms. Non-thermal emission (synchrotron or

gyrosynchrotron) shows negative spectral indices, while thermal free-free emission from ionized gas shows flat or positive spectral indices ($-0.1 < \alpha < 2$).

The YSOs that power outflows are commonly associated with thermal free-free emission at centimeter wavelengths. When resolved, these radio sources are generally found to be elongated along a direction close to the axis of the large-scale outflow. Because of these characteristic properties, these sources are called thermal radio jets (see Rodríguez 1995, 1996; Anglada 1996), and constitute the base (i.e., the part nearest to the origin, heavily obscured in the optical) of the large scale thermal jets observed at optical wavelengths (see Sect. 1.2).

Reynolds (1986) constructed a simple model of the free-free emission from a collimated ionized flow that is very useful to study the emission of a thermal radio jet. The jet was modeled as a biconical flow with a narrow opening angle and power-law dependences for the velocity, temperature, and ionization fraction. The width of the jet as a function of distance to the origin is also described by a power law of index ϵ, so that a constant opening angle outflow has a value of $\epsilon = 1$. For the "standard" case of a jet with constant velocity, temperature, and ionization fraction, the model of Reynolds (1986) predicts that the flux density and angular size (θ_ν) of the radio continuum emission from a thermal jet are functions of the frequency in the form:

$$S_\nu \quad \propto \quad \nu^{1.3-0.7/\epsilon}, \tag{1.4}$$

$$\theta_\nu \quad \propto \quad \nu^{-0.7/\epsilon}. \tag{1.5}$$

The model of Reynolds (1986) describes only the behavior of the emission but does not deal with the mechanism that originates the ionization required to produce it. Photoionization does not appear to be the ionizing mechanism, since in the sources associated with low-luminosity objects, the number of UV photons from the star is clearly insufficient to produce the ionization required to explain the observed radio continuum emission (e.g., Rodríguez et al. 1989; Anglada 1995). Observed flux densities in low-luminosity objects are several orders of magnitude higher than those expected by photoionization (see Figure 1.5a).

As photoionization cannot account for the observed radio continuum emission of low-luminosity objects, shock ionization was proposed as a viable alternative mechanism (e.g., Torrelles et al. 1985). Curiel, Cantó & Rodríguez (1987) and Curiel (1989) modeled the scenario in which a neutral stellar wind is ionized as a result of a shock against the surrounding high-density material, assuming a plane-parallel shock. From the results obtained in this model a relationship between the momentum rate in the outflow ($\dot{P}$) and the radio luminosity ($S_\nu d^2$) at centimeter wavelengths can be obtained (see Anglada 1996):

$$\left(\frac{\dot{P}}{M_\odot \, \mathrm{yr}^{-1} \, \mathrm{km}\, \mathrm{s}^{-1}}\right) = \frac{10^{-35}}{\eta} \left(\frac{S_\nu d^2}{\mathrm{mJy\, kpc}^2}\right), \tag{1.6}$$

where η is an efficiency factor that can be taken to equal the ionizing fraction of the stellar wind that is shocked and originates the observed radio continuum emission. This prediction is in well agreement with the results obtained from a large number of observations, for an average
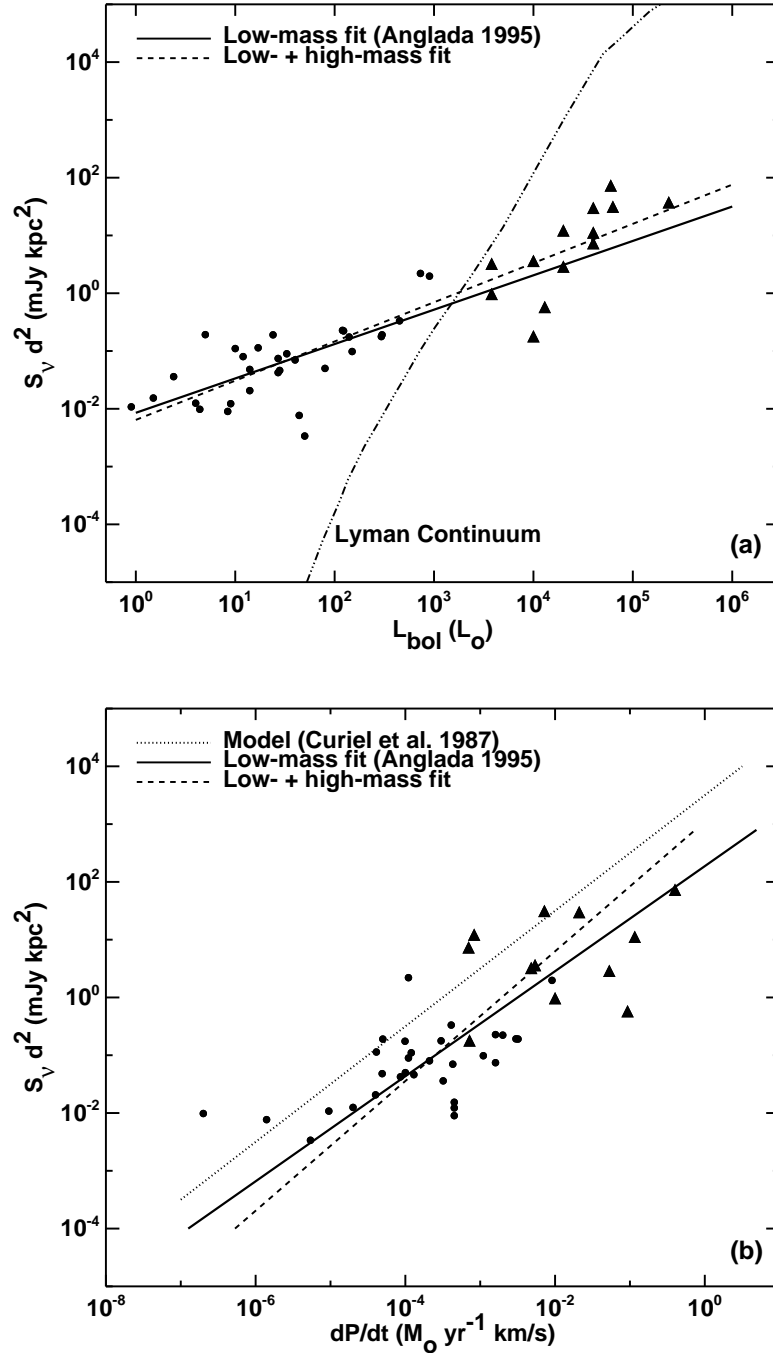
Figure 1.5 **(a)** Observed radio continuum luminosity, $S_\nu d^2$, as a function of the bolometric luminosity, L_{bol}. S_ν is the observed flux density at centimeter wavelengths and d is the distance to the source. **((a))** $S_\nu d^2$ vs the momentum rate in the outflow, $\dot{P}$. In both panels, the circles represent data on low luminosity YSOs (Anglada 1996), while the triangles represent high luminosity radio jets (Anglada et al., in preparation). Solid lines are least square fits to the data of low luminosity YSOs, while dashed lines are fits to both, low and high luminosity YSOs. Dotted-dashed line in panel (a) represents the values expected from Lyman-continuum radiation for a zero-age main-sequence star of the given bolometric luminosity. Dotted line in panel (b) represents the values expected from the model of shock-ionization of Curiel et al. 1987.

efficiency $\eta \simeq 0.1$ (see Figure 1.5b; Anglada et al. 1992; Anglada 1995). Therefore, these results suggest that the mechanism responsible for the free-free emission in low-luminosity objects is ionization produced by shocks of the jet with the high-density ambient medium.

For high-luminosity objects, the number of UV photons from the star is enough to produce the ionization required to produce the observed radio continuum emission, and therefore, the detection of free-free emission in these objects could be easily explained in terms of an optically thin HII region. However, in a few very young high-luminosity objects, radio jets with radio luminosities several orders of magnitude weaker than expected for a HII region have been found. Interestingly, the radio luminosities of these high-mass radio jets seem to follow similar correlations than low-mass radio jets (see Figure 1.5; Rodríguez et al. 2008; Anglada et al., in preparation). Therefore, the ionizing mechanism for jets associated with very young high-mass stellar objects appears to be similar to that of jets associated with low-mass YSOs (Anglada et al., in preparation). At later stages, photoionization should start and massive YSOs develop an HII region (Sect. 1.1.2) that finally dominates the emission in the centimeter wavelength range. This raises interesting questions about the possible existence of photoionized radio jets, and on how and when massive stars start to develop their associated HII regions.

1.5   Motivation, methodology and work scheme

The thesis work reported here is based on high angular resolution, highly sensitive, multiepoch observations of the radio emission associated with very young, deeply embedded, stellar objects in regions with signs of outflow activity. The main goal of this work is to study the earliest phases of the star formation process, when young stellar objects (YSOs) are still deeply embedded in their parental molecular cloud. At these stages, YSOs are detected mainly as radio (centimeter, millimeter or submillimeter) or far-IR sources. In contrast with the poor angular resolution currently achievable in the far-IR, the radio wavelengths have the advantage that subarcsecond angular resolution can be achieved through interferometric observations.

Radio emission from very young stellar objects is usually weak. It corresponds mostly to free-free emission from ionized jets at centimeter wavelengths and thermal dust emission from envelopes or disks at millimeter wavelengths. Although these observations do not trace the protostar itself, they trace a region very close to the object and provide the best estimate currently available for its position. Consequently, a radio study with *high angular resolution and sensitivity* would provide useful results on the *multiplicity* of deeply embedded YSOs in their earliest stages of the formation process, on the *origin of jets* (since it traces the base of jets, the region closest to the driving source), and on the associated *circumstellar accretion disks*. Accretion disks are a fundamental element in the star formation process in general, and in jet acceleration and collimation, and planetary formation in particular.

If the angular resolution is high enough, a *multiepoch* observational approach could reveal detectable changes in the structure of the sources, such as the development of new ejections, orbital proper motions of the stars, or even changes in the structure of protoplanetary disks. Since velocities involved are typically of the order of 10-100 km/s, these motions would produce

noticeable changes at scales of $0.1''$-$1''$ in time scales of 5-10 yr, for nearby star-forming regions.

In order to reach these goals we performed sensitive high angular resolution observations in the cm-submm wavelength range of a sample of five star-forming regions harboring low-, intermediate-, and high mass protostars. We used some of the most powerful radio interferometers available at present: the Very Large Array (VLA), which operates at centimeter wavelengths, the Combined Array for Research in Millimter Astronomy (CARMA) which operates at millimeter wavelengths, and the Submillimeter Array (SMA) which operates at submillimeter wavelengths. The VLA was available since the beginning of the thesis work and most of the data were obtained with this interferometer. CARMA and the SMA became operative recently, and the data presented in this thesis work are among the first results obtained with these instruments.

New observational developments, such as the Expanded VLA (EVLA), the upgrade of MER-LIN (e-MERLIN), and the Atacama Large Millimeter/submillimeter Array (ALMA) are starting to become operative, providing an excellent framework to pursue the work initiated in this thesis.

The thesis is structured as follows:

- In chapter 2 we present a study of the low-mass star-forming region L723. This region harbours a prototypical multipolar molecular outflow which has been proposed to be powered by a multiple stellar system. We performed a very sensitive observation of this region and found a multiple system of centimeter radio sources. We complemented this study with data at millimeter wavelengths in order to investigate the nature of the emission of all the components of the system, and we found that all of them are probably YSOs.

- In chapter 3 we study the low-mass star-forming region HL/XZ Tau. Very sensitive high angular resolution observations allowed us to map the structure of the disk in HL Tau, and to find signs of planet formation in it. Furthermore, our observations revealed that XZ Tau, which was though to be a binary system from previous HST observations, is actually a triple system of YSOs. This discovery offers a simple explanation for the powerful periodic ejections previously known to arise from this system.

- In chapter 4 we present the results of VLA and CARMA observations towards the intermediate-mass star forming region NGC 2071. This region contains one of the most powerful outflows known so far, and a cluster of YSOs previously detected at IR wavelengths. We detected centimeter and millimeter emission in four of the IR sources, and we studied the jets and disks associated with individual objects.

- In chapter 5 we present a study of the high-mass star-forming region W 75N. Through VLA and SMA observations of continuum and molecular line emission, we studied the nature of each source and their interrelationship.

- In chapters 6 and 7 we study the high-mass star-forming region HH 80-81. This region contains the largest and most collimated radio jet known so far. We found evidence of circumstellar dust emission, that we modeled as an accretion disk associated with the massive protostar that drives the jet. We present the discovery of linearly polarized synchrotron emission in the jet lobes. This is the first time that such emission is detected in a protostellar jet, and allowed us to describe the structure and strength of the magnetic field in the jet, in analogy with extragalactic sources.

1.6 List of Publications

The work presented in this Thesis has originated the following publications:

- *"A Multiple System of Radio Sources at the Core of the L723 Multipolar Outflow"*
  Carrasco-González, C., Anglada, G., Rodríguez, L.F., Torrelles, J.M., Osorio, M., Girart, J.M. 2008, The Astrophysical Journal, 676, 1073-1081

- *"High Angular Resolution Radio Observations of the HL/XZ Tau Region: Mapping the 50 AU Protoplanetary Disk Around HL Tau and Resolving XZ Tau S Into a 13 AU Binary"*
  Carrasco-González, C., Rodríguez, L.F., Anglada, G., Curiel, S. 2009, The Astrophysical Journal, 693, L86-L90

- *"A Bright Radio HH Object with Large Proper Motions in the Massive Star-forming Region W75N"*
  Carrasco-González, C., Rodríguez, L.F., Torrelles, J.M., Anglada, G., González-Martín, O. 2010, The Astronomical Journal, 139, 2433-2439

- *"A Magnetized Jet from a Massive Protostar"*
  Carrasco-González, C., Rodríguez, L.F., Anglada, G., Martí, J., Torrelles, J.M., Osorio, M., Science, 330, 1209

- *"Multiplicity, Disks, and Jets in the YSOs of the NGC 2071 Star-Forming Region"*
  Carrasco-González, C., Osorio, M., Anglada, G., D'Alessio, P., Rodíguez, L.F., Gómez, J.F., Torrelles, J.M., submitted to The Astrophysical Journal (2010)

- *"A Resolved Circumstellar Disk Around the Massive Protostar IRAS 18162−2048"*
  Carrasco-González, C. et al., in preparation

Other publications related to the Thesis work:

- *"A new radial system of dark globules in Monoceros"*
  Carrasco-González, C., López, R., Gyulbudaghian, A., Anglada, G., Lee, C.W. 2006, Astronomy & Astrophysics, 445, L43-L46

- *"Proper Motions of Thermal Radio Sources Near HH 7-11 in the NGC 1333 Star-Forming Region"*
  Carrasco-González, C., Anglada, G., Rodríguez, L.F., Torrelles, J.M., Osorio, M. 2008, The Astronomical Journal, 136, 2238-2243

- *"The nature of HH 223 from long-slit spectroscopy"*
  López, R., Estalella, R., Gómez, G., Riera, A., **Carrasco-González, C.** 2009, Astronomy & Astrophysics, 498, 761-769

- *"HH 223: a parsec-scale H_2 outflow in the star-forming region L723"*
  López, R., Acosta-Pulido, J.A., Gómez, G., Estalella, R., **Carrasco-González, C.** 2010, Astronomy & Astrophysics, submitted

Bibliography

Anglada, G. 1996 in Radio emission from the stars and the sun. ASP Conf. Ser., 93, 3

Anglada, G., Villuendas, E., Estalella, R., Beltrán, M.T., Rodríguez, L.F., Torrelles, J.M., Curiel, S. 1998, AJ, 116, 2953

Anglada, G., Rodríguez, L.F., Osorio, M., Torrelles, J.M., Estalella, R., Beltrán, M.T., Ho, P.T.P. 2004, ApJ, 605, 137

Anglada, G., López, R., Estalella, R., Masegosa, J., Riera, A., Raga, A.C. 2007, AJ, 133, 2799

Adams, F.C., Lada, C.J., Shu, F.H. 1987, ApJ, 312, 788

Andre, P., Ward-Thompson, D., Barsony, M. 1993, ApJ, 406, 122

Bally, J., Lada, C., 1983, ApJ, 265, 824

Bastien, P., Menard, F. 1988, ApJ, 326, 334

Bastien, P., Menard, F. 1990, ApJ, 364, 232

Benjamin, R.A. et al. 2003, PASP, 115, 953

Bonnell I.A., Bate M.R., Clarke C.J., Pringle J.E. 1997, MNRAS, 285, 201

Bonnell I.A., Vine S.G., Bate M.R. 2004, MNRAS, 349, 735

Bontemps, S., André, P., Tereby, S., Cabrit, S. 1996, A&A, 311, 858

Burrows, C.J., et al. 1996, ApJ, 473, 437

Carpenter J.M., Meyer M.R., Dougados C., Strom S.E., Hillenbrand L.A. 1997, AJ, 114, 198

Cesaroni R. 2005, Ap&SS, 295, 5

Duquennoy, A., Mayor, M. 1991, A&A, 248, 485

Edgar R, Clarke C. 2003, MNRAS, 338, 962

Edwards, S., Snell, R.L. 1982, ApJ, 261, 151

Edwards, S., Snell, R.L. 1983, ApJ, 270, 605

Edwards, S., Snell, R.L. 1984, ApJ, 281, 237

Egan M.P., Shipman R.F., Price S.D., Carey S.J., Clark F.O., Cohen M. 1998, ApJL, 494, 1999

Eislöffel, J. 2000, A&A, 354, 236

Gueth, F., Guilloteau, S., 1999, A&A, 343, 571

Guilloteau, S., Dutrey, A., Simon, M. 1999, A&A, 348, 570

Haro, G. 1952, ApJ, 115, 572

Herbig, G.H. 1951, ApJ, 113, 697

Hoare, M.G., Kurtz, S.E., Lizano, S., Keto, E., Hofner, P. 2007, in Protostars and Planets V, p.181-196

Keto, E. 2007, ApJ, 666, 976

Kitamura, Y., Momose, M., Yokogawa, S., Kawabe, R., Tamura, M., Ida, S. 2002, ApJ, 581, 357

Kurtz, S., Cesaroni, R., Churchwell, E., Hofner, P., Walmsley, C.M. 2000, in Protostars and Planets IV, p. 299

Kurtz, S. 2005, in Massive star birth: A crossroads of Astrophysics. IAU Symp. 227, pp.111-119

Kwan, J., Scoville, N. 1976, ApJ, 210, 39

Lada, C.J. 1987, in Star forming regions; Proceedings of the Symposium, Tokyo, Japan, Nov. 11-15, 1985. p. 1-17

Larson, R.B. 1972, MNRAS, 157, 121

Lin, Douglas N.C., Pringle, John E. 1990, ApJ, 358, 515

Loinard, L., Rodríguez, L.F., D'Alessio, P., Wilner, D.J., Ho, P.T.P. 2002, ApJ, 581, 109

López, R., Estalella, R., Gómez, G., Riera, A., Carrasco-González, C. 2009, A&A, 498, 761

Martí, J., Rodríguez, L.F., Reipurth, B. 1993, ApJ, 416, 208

Mathieu, R.D. 1994, ARA&A, 32, 465

McCaughrean, M.J., O'Dell, C.R. 1996, Aj, 111, 1977

Menten K.M., Pillai T., Wyrowski F. 2005, in Massive star birth: A crossroads of Astrophysics. IAU Symp. 227, pp.23-34

Mezger P.G., Altenhoff W., Schraml J., Burke B.F., Reifenstein E.C. III, Wilson T.L. 1967, ApJ, 150, 157

Nakano T. 1989, ApJ, 345, 464

Osorio, M., Lizano, S., D'Alessio, P. 1999, ApJ, 525, 808

Padgett, D.L., Brandner, W., Stapelfeldt, K.R., Strom, S.E., Terebey, S., Koerner, D. 1999, AJ, 117, 1490

Patel, N.A., Curiel, S., Sridharan, T.K., Zhang, Q., Hunter, T.R., Ho, P.T.P., Torrelles, J.M., Moran, J.M., Gómez, J.F., Anglada, G. 2005, Nature, 437, 109

Perault M., Omont A., Simon G., Seguin P., Ojha D., et al. 1996, A&A, 315, 165

Pfalzner, S., Tackenberg, J., Steinhausen, M. 2008, A&A, 487, 45

Pravdo, S.H., Rodríguez, L.F., Curiel, S., Cantó, J., Torrelles, J.M., Becker, R.H., Sellgren, K. 1985, ApJ, 293L, 35

Raga, A.C., Cantó, J., Calvet, N., Rodríguez, L.F., Torrelles, J.M. 1993, A&A, 276, 539

Reipurth, B., Bally, J. 2001, ARA&A, 39, 403

Reynolds, S.P. 1986, ApJ, 304, 713

Rodríguez, L.F., Moran, J.M., Ho, P.T.P. 1980, ApJ, 240L, 149

Rodríguez, L.F., Carral, P., Ho, P.T.P., Moran, J.M. 1982, ApJ, 260, 635

Rodríguez, L.F., Cantó, J., Torrelles, J.M., Gómez, J.F., Ho, P. T. P. 1992, ApJL, 393, 29

Rodríguez, L.F. 1994, RMAA, 29, 69

Rodríguez, L.F. 1995, RMAA Ser. Conf., 1, 1

Rodríguez, L.F. 1996, RMAA Ser. Conf., 4, 7

Rodríguez, L.F., D'Alessio, P., Wilner, D.J., Ho, P.T.P., Torrelles, J.M., Curiel, S., Gómez, Y., Lizano, S., Pedlar, A., Cantó, J., Raga, A.C. 1998, Nature, 395, 355

Rodríguez, L.F., Garay, G., Brooks, K.J., Mardones, D. 2005, ApJ, 626, 953

Rodríguez, L.F., Moran, J.M., Franco-Hernández, R., Garay, G., Brooks, K.J., Mardones, D. 2008, AJ, 135, 2370

Ruden, S.P., Lin, D. N. C. 1986, ApJ, 308, 883

Shepherd, D.S., Claussen, M.J., Kurtz, S.E. 2001, Science, 292, 1513

Shu F.H. 1977, ApJ, 214, 488

Shu F.H., Adams F.C., Lizano S. 1987, ARA&A, 25, 23

Snell, R.L., Loren, R.B., Plambeck, R.L. 1980, ApJ, 239L, 17

Stahler S.W, Palla F., Ho P.T.P. 2000, in Protostars and Planets IV, pp. 327

Stapelfeldt, K.R., Krist, J.E., Menard, F., Bouvier, J., Padgett, D.L., Burrows, C.J. 1998, ApJ, 502, L65

Stojimirović, I., Snell, R. L., & Narayanan, G. 2008, ApJ, 679, 557

Strom, S.E. 1995, RMAA Ser. Conf., 1, 317

Terebey S., Shu F.H., Cassen P. 1984, ApJ, 286, 529

Torrelles, J.M., Rodríguez, L.F., Cantó, J., Carral, P., Marcaide, J., Moran, J.M.; Ho, P.T.P. 1983, ApJ, 274, 214

Torrelles, J.M. 1991, in Atoms, ions and molecules: New results in spectral line astrophysics. ASPC, 16, p. 257.

Torrelles, J.M., Gómez, J.F., Ho, P.T.P., Rodríguez, L.F., Anglada, G., Cantó, J. 1994, ApJ, 435, 290

Torrelles, J.M., Patel, N.A., Curiel, S., Ho, P.T.P., Garay, G., Rodríguez, L.F. 2007, ApJ, 666, 37

van der Tak F.F.S., Menten K.M. 2005. A&A, 437, 947

Wolfire M.G., Cassinelli J.P. 1987, ApJ, 319, 850

Wilner, D.J., Ho, P.T.P., Rodríguez, L.F. 1996, ApJ, 470L, 117

Wu, Y., Huang, M., He, J. 1996, A&AS, 115, 283

Wu, Y., Wei, Y., Zhao, M., Shi, Y., Yu, W., Qin, S., Huang, M. 2004, A&A, 426, 503

Yorke H.W. 1986, ARA&A, 24, 48

Yorke H.W., Sonnhalter C. 2002, ApJ, 569, 846

Zinnecker H., McCaughrean M.J., Wilking B.A. 1993 in Protostars and Planets III, p. 429

Zinnecker, H., Yorke, H.W. 2007, A&A, 437, 947

Zuckerman, B., Kuiper, T.B.H., Rodríguez Kuiper, E.N. 1976, ApJ, 209L, 137

2

A Multiple System of Radio Sources at the Core of the L723 Multipolar Outflow*

In this chapter we present high angular resolution VLA multi-epoch continuum observations at 3.6 cm and 7 mm towards the core of the L723 multipolar outflow revealing a multiple system of four radio sources suspected to be YSOs in a region of only $\sim$4″ (1200 AU) in extent. The 3.6 cm observations show that the previously detected source VLA 2 contains a close (separation $\simeq$0.″29 or $\sim$90 AU) radio binary, with components (A and B) along a position angle of $\sim$150°. The northern component (VLA 2A) of this binary system is also detected in the 7 mm observations, with a positive spectral index between 3.6 cm and 7 mm. In addition, the source VLA 2A is associated with extended emission along a position angle of $\sim$115°, that we interpret as outflowing shock-ionized gas that is exciting a system of HH objects with the same position angle. A third, weak 3.6 cm source, VLA 2C, that is detected also at 7 mm, is located $\sim$0.″7 northeast of VLA 2A, and is possibly associated with the water maser emission in the region. The 7 mm observations reveal the presence of an additional source, VLA 2D, located $\sim$3.″5 southeast of VLA 2A, and with a 1.35 mm counterpart. All these radio continuum sources have a positive spectral index, compatible with them being YSOs. We also propose that the high velocity CO emission observed in the region could be the superposition of multiple outflows (at least three independent bipolar outflows) excited by the YSOs located at the core, instead of the previous interpretations in terms of only one or two outflows.

2.1   Introduction

L723 is an isolated dark cloud at a distance of 300 ± 150 pc (Goldsmith et al. 1984). Located in this cloud is a Class 0 source, IRAS 19156+1906, with a luminosity of $\sim$3.4 L$_\odot$ (Dartois et al. 2005). The IRAS source is associated with a CO outflow, first mapped by Goldsmith et al. (1984). The outflow shows a peculiar quadrupolar morphology, consisting of two pairs of

red-blue lobes with a common center, as is clearly seen in the maps of Avery et al. (1990). The larger pair of lobes extends along a direction with a P.A.$\simeq$100°, while the smaller pair extends along a direction with a P.A.$\simeq$30°. Over the years, the peculiar quadrupolar morphology of the L723 outflow has been interpreted as due to the presence of either one or two driving sources (see Anglada, Rodríguez & Torrelles 1996 and references therein). In the first case, the quadrupolar morphology is attributed to limb-brightening effects in the lobes of a single bipolar outflow, to splitting of the lobes due to interaction with ambient clumps, or to precession of the outflow axis. In the second case, the quadrupolar structure is attributed to two independent bipolar outflows, each one driven by a different source.

Previous VLA D-configuration observations (angular resolution of $\sim$8″) towards the center of the outflow revealed two 3.6 cm continuum sources, VLA 1 and VLA 2, separated by 15″ (Anglada et al. 1991). However, only VLA 2 is associated with millimeter emission from circumstellar dust (Cabrit & André 1991), suggesting that it is the counterpart of IRAS 19156+1906. VLA 2 has also been associated with a nearby ($\sim$0″.7 northeast from VLA 2) H_2O maser as well as with NH_3 emission (Girart et al. 1997). Also, only VLA 2 seems to be associated with the CO outflow as shown by interferometric observations with the Nobeyama Millimeter Array (Hirano et al. 1998) and with the Berkeley Illinois Maryland Association (BIMA) array (Lee et al. 2002). In the 3.6 cm maps of Anglada et al. (1996), made with data from the A and B configurations of the VLA (angular resolution of $\sim$0″.3), the centimeter emission of VLA 2 is elongated along a direction with a P.A.$\simeq$118°, that is close to that of the large pair of CO lobes. In addition, H_2 emission and Herbig-Haro (HH) objects have been found in the region along a direction with a P.A.$\simeq$ 115°, similar to that of the elongation of VLA 2 (Vrba et al. 1986; Hodapp 1994; Palacios & Eiroa 1999; López et al. 2006). These results suggest that the outflow activity along the direction $\sim$100°-118° is driven by the young protostellar object VLA 2. However, the identification of the exciting source of the smaller pair of CO lobes at P.A.$\simeq$30° remained unclear. As already pointed out, one possibility is that VLA 2 is the driving source of the two pairs of bipolar lobes, e.g., driving each pair in a different epoch as a consequence of precession of the jet axis. The second possibility is the presence of another, still undetected source in the vicinity of VLA 2, that could be driving the small pair of CO lobes.

Other regions harboring multipolar outflows, when studied with subarcsecond angular resolution (equivalent to physical scales of tens to hundreds of AUs for the relatively nearby regions that are better studied) and sensitivity at the level of tens of μJy, have shown that the multipolar outflow morphology is usually associated with the presence of multiple YSOs at the center of the outflows: e.g., IRAS 16293−2422 (CO outflow: Mizuno et al. 1990; radio continuum: Estalella et al. 1991); IRAS 20050+2720 (CO outflow: Bachiller et al. 1995; radio continuum: Anglada, Rodríguez & Torrelles 1998); HH 111 (CO outflow: Cernicharo & Reipurth 1996; radio continuum: Reipurth et al. 1999); L1634 (H_2 jet: Hodapp & Ladd 1995; radio continuum: Beltrán et al. 2002); HH 288 (CO outflow: Gueth et al. 2001; radio continuum: Franco-Hernández & Rodríguez 2003); OMC-1S (optical jets: Bally et al. 2000; radio continuum: Zapata et al. 2004).

In this chapter we present sensitive, high angular resolution multi-epoch observations at 3.6 cm of the radio sources detected in the central region of the L723 outflow. Our goals were to search for changes in the structure of VLA 2 that could help us to clarify the origin of the quadrupolar morphology of the outflow and to search for additional indications of multiplicity at very small scales. We also analyze VLA archive 7 mm continuum data of the region.

2.2   Observations

The 3.6 cm continuum observations were carried out in six epochs, ranging from 1995 August 12 to 2000 December 16. The data from the 1995.6 observations were already reported by Anglada et al. (1996). The VLA was used in its A configuration, providing an angular resolution of $\sim 0\rlap{.}''3$. Absolute flux calibration was achieved by observing 3C 286, for which a flux density of 5.20 Jy at 3.6 cm was adopted. Data editing and calibration were carried out using the Astronomical Image Processing System (AIPS) package of NRAO, following the standard VLA procedures. The observation dates, the bootstrapped flux densities of 1925+211, the phase calibrator used in all the observations, as well as the parameters of the synthesized beams, and the rms noise of the naturally weighted maps are given in Table 2.1. Due to the weakness of the sources detected the signal-to-noise ratio per baseline was insufficient to self-calibrate the data.

For each epoch, we made cleaned maps with different values of the parameter ROBUST of IMAGR (Briggs 1995). The ROBUST parameter ranges in value from $+5$ to -5, with the maps made with ROBUST=$+5$ (equivalent to natural weighting of the visibility data) having the highest sensitivity but the lowest angular resolution and the maps made with ROBUST=-5 (equivalent to uniform weighting) having the highest angular resolution but the lowest sensitivity. For each value of the ROBUST parameter the map of each epoch was restored using a circular beam whose HPBW is the geometric mean of the major and minor axes of the synthesized beam obtained by concatenating the uv data of all the six epochs (HPBW = $0\rlap{.}''29$ for naturally weighted maps and HPBW = $0\rlap{.}''19$ for uniformly weighted maps). This average restoring beam was adopted to facilitate comparison between the different epochs and to allow averaging of all the 3.6 cm images into a single image. We consider this procedure appropriate since the major and minor axes of the synthesized beams of the individual observing sessions (see Table 2.1) are within $\sim 10\%$ of the adopted average HPBW.

To improve the sensitivity and uv coverage, we have concatenated the uv data from all the epochs to obtain single maps, which we will refer to as "All-Epochs" maps. Since some of the structures persist from one epoch to another, while others change, the procedure of concatenating data could result in spurious effects in the final images. Therefore, we checked that the maps obtained by concatenating all the uv data do not show significant differences from the maps obtained by averaging all the single epoch maps.

The 7 mm continuum data were taken from the VLA archive. The data consist of four sets of observations in the D, C and CnB configurations (see Table 2.2). Absolute flux calibration was achieved by observing 3C 286, and a model image at 7 mm for this calibrator was used

Table 2.1. Observations at 3.6 cm

Epoch	Observation Date	Bootstrapped Flux Density of Phase Calibrator[a] (Jy)	Synthesized Beam[b] HPBW (arcsec)	P.A. (deg)	rms Noise[b] (μJy beam^{-1})
1995.6	95-Aug-12	1.146 ± 0.006	0.32 × 0.27	−85	11
1997.0	97-Jan-10	0.926 ± 0.004	0.27 × 0.25	15	11
1998.2	98-Mar-27	0.94 ± 0.01	0.34 × 0.25	58	12
1998.4	98-May-26	0.952 ± 0.007	0.34 × 0.25	58	11
1999.5	99-Jul-03	1.260 ± 0.006	0.39 × 0.26	50	14
2000.9	00-Dec-16	1.65 ± 0.02	0.28 × 0.27	−70	6

[a]The phase calibrator used in all the observations was 1925+211.

[b]For naturally weighted maps.

Table 2.2. Observations at 7 mm

Observation Date[a]	VLA Configuration	Bootstrapped Flux Density of Phase Calibrator[a] (Jy)	Synthesized Beam[b] HPBW (arcsec)	P.A. (deg)	rms Noise[b] (mJy beam^{-1})
02-Jan-05	D	2.38 ± 0.04	2.37×1.75	−22	0.12
04-Feb-01	CnB	1.85 ± 0.05	0.45×0.39	−76	0.12
04-Mar-26	C	2.22 ± 0.05	0.58×0.51	−8	0.12
05-Jul-29	C	1.68 ± 0.02	0.57×0.51	+34	0.12

[a]The phase calibrator used in all the observations was 1925+211.

[b]For naturally weighted maps.

to calibrate the data in amplitude. In order to improve the sensitivity of the final image, but keeping a balanced contribution from the different configurations, we have concatenated all the available uv data giving the same weight to the D and C+CnB data. Since these data come from different configurations, it is not possible to average the individual maps. From these uv data we obtained a 7 mm "All-Epochs" naturally weighted map.

2.3   Results and Discussion

2.3.1   VLA 2A and 2B: A Close Binary System of YSOs

In Figure 2.1 we show naturally weighted 3.6 cm maps of VLA 2 for each individual epoch. We have detected radio continuum emission from VLA 2 in all the epochs, with total flux densities varying in the range 0.2-0.5 mJy. In these maps, we see changes in the morphology of VLA

Table 2.3.   YSO Candidates Associated with VLA 2

| Component | Position (J2000)[a] | | | Flux Density (mJy)[b] | | Spectral |
	RA	DEC	Error	3.6 cm	7 mm	Index
A	19 17 53.673	+19 12 19.59	0″.01	0.11 ± 0.04[c]	0.7 ± 0.2	$+1.1 \pm 0.3$
B	19 17 53.685	+19 12 19.34	0″.01	0.08 ± 0.02	<0.37[d]	$<+0.9$
C	19 17 53.739	+19 12 19.77	0″.07	0.05 ± 0.02[e]	0.7 ± 0.2[f]	$+1.5 \pm 0.4$
D	19 17 53.894	+19 12 17.96	0″.09	<0.02[d]	0.6 ± 0.2	$>+2.0$

[a]Positions for components A and B are derived from Gaussian fits to the sources in the 3.6 cm "All-Epochs" uniformly weighted map (Fig. 2.3a). Positions for components C and D are derived from the 7 mm map (Fig. 2.4). Units of right ascension are hours, minutes, and seconds, and units of declination are degrees, arcminutes, and arcseconds.

[b]Derived from Gaussian fits to "All-Epochs" naturally weighted maps.

[c]Uncertainty is estimated from the observed peak intensity variability in our multi-epoch observations (Table 2.3)

[d]4-σ upper limit.

[e]Sum of the flux densities of VLA 2Ca and VLA 2Cb.

[f]Angularly resolved source. Deconvolved size is $\sim 1''.2 \pm 0''.2$ at a P.A $\simeq 90° \pm 7°$.

2, but some of the structures persist from one epoch to another. In particular, in three of the epochs VLA 2 shows a clear double morphology with two components separated by $\sim 0''.3$ along a P.A. of $\sim 150°$. This double morphology appears in the 1998.2 and 1998.4 epochs, where the uv coverage was exactly the same, and in the 2000.9 epoch, which was a full-track observation and therefore the uv coverage obtained was much better than in the other epochs (see Table 2.1 for the HA ranges and time on source for each epoch of observation). In the 1999.5 epoch, the uv coverage was also very similar to that of the 1998 epochs, but the double morphology is not so evident. We think this could be due to the higher rms noise of the 1999.5 map and to the increase of the flux density of the northern component (see below) that partially masks the emission of the southern component. Given these considerations, it is likely that VLA 2 is actually a persistent double radio source, with the differences in the observed morphology being mainly due to the different uv coverage from one epoch to another.

A way to mitigate the effects introduced by the different uv coverages would be to make uniformly weighted maps of the individual epochs. In uniformly weighted maps all the grid cells have equal weight, which compensates for the high concentration of data points in the inner region of the uv plane. This provides a more uniform coverage of the gridded uv plane, resulting in maps having higher angular resolution than naturally weighted maps. Unfortunately, uniform weighting yields lower sensitivity, and due to the weakness of the source, it is difficult to detect it in the uniformly weighted map of a single epoch. However, it is still possible to test our hypothesis of a double radio source with the available data. For this purpose we have made uniformly weighted maps from two different sets of concatenated uv data: (i) the three epochs
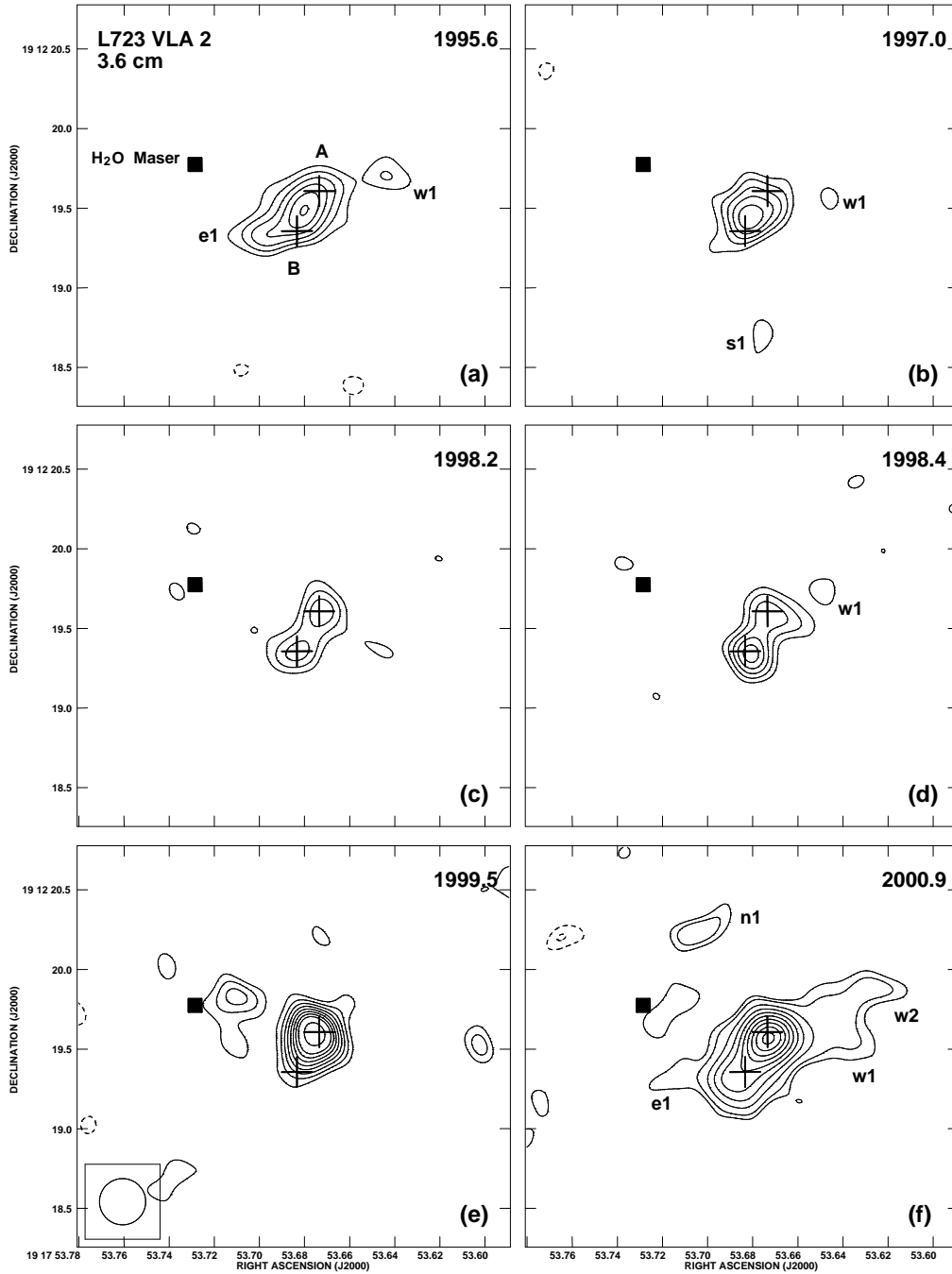
Figure 2.1 VLA 3.6 cm continuum maps of the VLA 2 region at different epochs, obtained with natural weighting. In order to better identify morphological changes from one epoch to other, the maps have been restored using the same circular beam of $0\rlap{.}''29$ (HPBW) and contoured in terms of the same reference value (11 μJy beam^{-1}). For panels (a) to (e), contour levels are -4, -3, 3, 4, 5, 6, 7, 8, 9, 10, and 12 times 11 μJy beam^{-1}, the typical rms of these maps (see Table 2.1). For panel (f), additional contours at -2, -1.5, 1.5, and 2 times 11 μJy beam^{-1} have been included so that the lowest contour level corresponds approximately to 3 times the rms of this map (see Table 2.1). The crosses mark the positions of VLA 2A and VLA 2B derived from Gaussian fits to the uniformly weighted "All-epochs" map (see text). The filled square marks the position of the H$_2$O maser detected by Girart et al. (1997). The radio continuum knots detected in the region (w2, w1, e1, e2, s1, and n1) are also labeled (see §2.3.1).
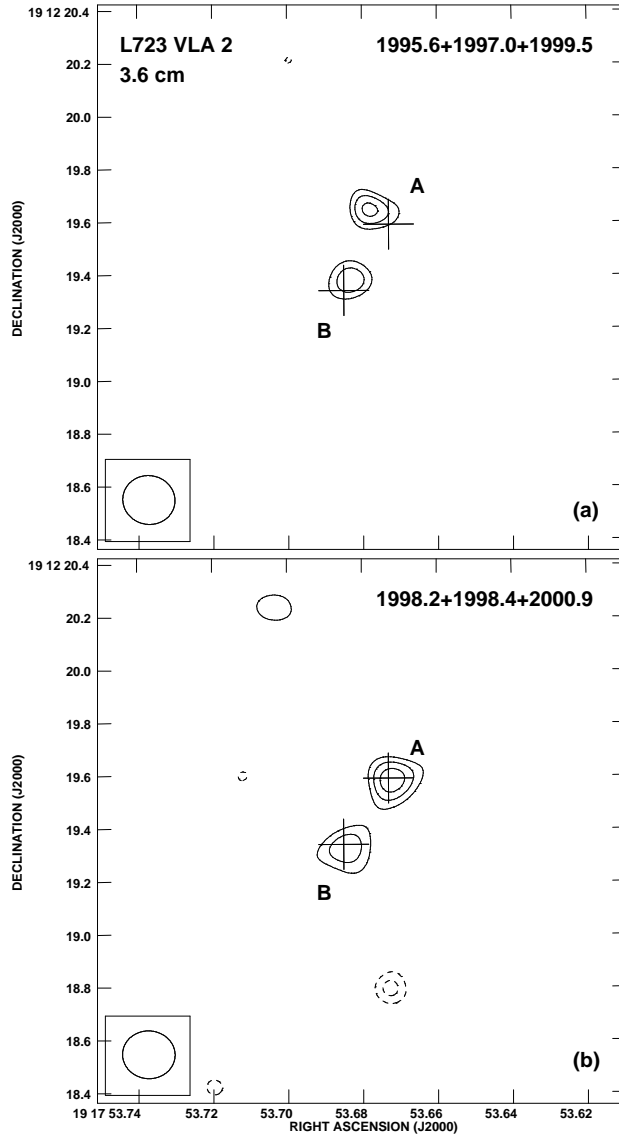
Figure 2.2 **(a)** Uniformly weighted map of the source VLA 2 at 3.6 cm made by concatenating the uv data of the 1995.6, 1997.0, and 1999.5 epochs (where VLA 2 does not show a clear double morphology; see Fig. 2.1). The synthesized beam of the map is $0\rlap{.}''20 \times 0\rlap{.}''18$, with a P.A. of 79°. Contour levels are −4, −3, 3, 4, and 5 times the rms of the map, 17 μJy beam^{-1}. **(b)** Same as (a), but for the 1998.2, 1998.4, and 2000.9 epochs (where VLA 2 shows a clear double morphology; see Fig. 2.1). The synthesized beam of the map is $0\rlap{.}''20 \times 0\rlap{.}''18$, with a P.A. of 86°. Contour levels are −4, −3, 3, 4, and 5 times the rms of the map, 12 μJy beam^{-1}. Note that in both maps the source VLA 2 shows a clear double morphology, suggesting that VLA 2 is a binary system of embedded YSOs (see text for further details). The crosses mark the positions of VLA 2A and VLA 2B derived from Gaussian fits to the uniformly weighted "All-epochs" map (see text, and Fig. 2.3a).

Table 2.4.   Monitoring of the VLA 2 binary at 3.6 cm

Epoch	Peak Intensity (mJy beam^{-1})[a]		Total Flux[b] Density (mJy)
	VLA 2A	VLA 2B	
1995.6	0.08 ± 0.01[c]	0.06 ± 0.01[c]	0.30 ± 0.03
1997.0	0.07 ± 0.01[c]	0.06 ± 0.01[c]	0.18 ± 0.03
1998.2	0.06 ± 0.01	0.06 ± 0.01	0.20 ± 0.02
1998.4	0.06 ± 0.01	0.07 ± 0.01	0.16 ± 0.02
1999.5	0.15 ± 0.01[c]	0.05 ± 0.01[c]	0.21 ± 0.03
2000.9	0.13 ± 0.01	0.07 ± 0.01	0.24 ± 0.02

[a]Derived from Gaussian fits to the 3.6 cm naturally weighted maps that have been restored with an average circular beam of HPBW=$0\rlap{.}''29$ (Fig. 2.1).

[b]Total flux density of the binary system excluding the extended emission (see Fig. 2.1).

[c]Obtained by fixing the Gaussian centers to the positions of VLA 2A and VLA 2B given in Table 2.2.

in which VLA 2 does not show clearly a double morphology, and (ii) the three epochs in which VLA 2 shows a clear double morphology. This procedure allows us to compare two maps with high enough angular resolution and sensitivity, as well as a good uv coverage. As can be seen in Figure 2.2, VLA 2 shows always a double morphology (with a slight change of $\sim 0\rlap{.}''1$ in the position of the sources), even in the map made with the data of the epochs in which the double morphology was not evident. This strongly supports that two radio continuum sources (that we call VLA 2A and VLA 2B) persist through all the epochs, covering a time span $\gtrsim 5$ yr.

Since all the data seem to be consistent with the presence of a double source, we obtained an "All-Epochs" uniformly weighted map (Fig. 2.3a) by concatenating all the uv data. The positions and flux densities of components VLA 2A and 2B, derived from Gaussian ellipsoid fits to this map, are given in Table 2.2. The angular separation of the two components is $0\rlap{.}''29$, which corresponds to a projected separation of ~ 90 AU (assuming a distance of 300 pc). If these sources were tracing some kind of high-velocity outflowing features, such as knots in a jet, a significant variation in their positions in the single epoch maps would be expected (e.g., a velocity of ~ 100 km s^{-1} in the plane of the sky would result in an angular displacement of $\sim 0\rlap{.}''35$ over the period of ~ 5 yr covered by our observations). The lack of a significant displacement from one epoch to another excludes that these sources trace high-velocity material, unless the axis of the motion was very close the line of sight (which does not seem to be the case, given that the blue and red lobes of the molecular outflow appear clearly separated on the sky). This, together with the additional properties observed for these sources (see below) led us to interpret VLA 2A and VLA 2B as a close binary system of embedded YSOs.

The individual epoch maps shown in Figure 2.1 suggest variability in the 3.6 cm flux density
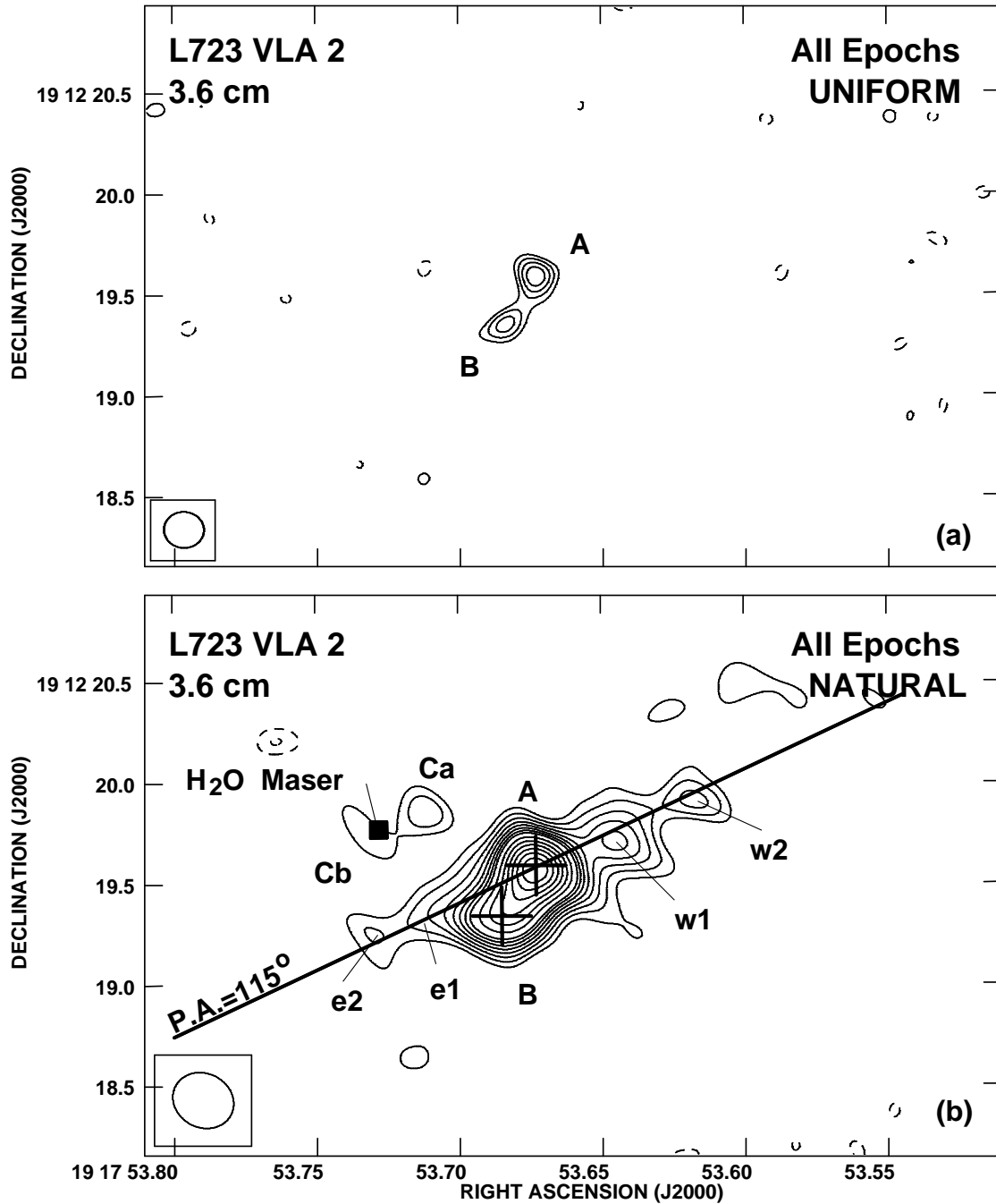
Figure 2.3 **(a)** Uniformly weighted "All-Epochs" map of the source VLA 2 at 3.6 cm, obtained by concatenating the uv data from all the epochs. The synthesized beam of the map is $0\rlap{.}''20 \times 0\rlap{.}''18$, with a P.A. of $86°$. Contour levels are -4, -3, 3, 4, 5, and 6 times the rms of the map, 11 μJy beam^{-1}. **(b)** Same as (a), but with natural weighting. The synthesized beam of the map is $0\rlap{.}''31 \times 0\rlap{.}''27$, with a P.A. of $63°$. Contour levels are -4, -3, 3, 4, 5, 6, 7, 8, 9, 10, 12, 14, 16, 18, and 20 times the rms of the map, 4 μJy beam^{-1}. Crosses mark the positions of VLA 2A and VLA 2B derived from Gaussian fits to the uniformly weighted map. The filled square marks the position of the H_2O maser detected by Girart et al. (1997). The axis of the extended emission (traced by knots w2, w1, e1, and e2), at P.A. of $\sim 115°$, is indicated.

of the compact components of the double source. In Table 2.3 we give the peak intensities of VLA 2A and VLA 2B at each epoch of observation. Because the angular resolution of our observations is similar to the angular separation of the two sources, these values of the peak intensity must be taken with care. However, given that the maps of the different epochs have been restored with the same beam, the variations of the peak intensities are expected to be representative of the variability of the individual components. The peak intensity of VLA 2B appears to be constant at all epochs, consistent with a value of 0.06 ± 0.01 mJy beam^{-1} (see Table 2.3). On the other hand, the peak intensity of VLA 2A is consistent with a value of 0.07 ± 0.01 mJy beam^{-1} (see Table 2.3) in the four first epochs, while in the last two epochs the peak intensity of the source increased approximately by a factor of two. Similar flux density variability has been observed in several embedded YSOs (e.g., Cep A, Porras et al. 2002; B335, Ávila et al. 2001). We interpret the variability in the flux density of VLA 2A as due to material recently ejected that still remains very close to the YSO and it is not distinguishable from the source.

In addition, we have detected 7 mm emission from VLA 2A (see Fig. 2.4). The flux densities at 3.6 cm and 7 mm of VLA 2A (see Table 2.2) imply a spectral index $\alpha \simeq 1.1 \pm 0.3$ ($S_\nu \propto \nu^\alpha$), consistent with partially optically thick free-free emission that could be tracing a radio jet. The nominal value of the spectral index obtained is slightly higher than the typical values found in ionized jets driven by YSOs, $0.3 \lesssim \alpha \lesssim 0.9$ (Anglada 1996 and references therein). This higher value of the spectral index of VLA 2A could be indicating that we are partially missing the extended emission of the possible radio jet, either because of insufficient uv coverage or because part of this extended emission is confused with the emission of the nearby source VLA 2B. Since the outer part of a thermal radio jet is where the emission is optically thinner, we would be observing preferentially the emission coming from the region closer to the driving source, where the optical depth is higher. This effect would increase the value of the spectral index with respect to that of the overall emission of a radio jet. Alternatively, a high value of the spectral index could be indicative of a significant contribution from dust emission at 7 mm. Both possibilities (free-free emission from a jet with a possible contribution of dust emission from a circumstellar disk or an envelope) are consistent with VLA 2A being a YSO.

We should note that the spectral indices derived in this chapter have been obtained from non-simultaneous observations and can be affected by time-variability of the sources. However, as discussed above, the flux variations observed in our multi-epoch observations suggest modest variability that it is not expected to affect our conclusions on the nature of the emission derived from the spectral index. Also, the 3.6 cm and 7 mm observations have different uv coverages, that could introduce additional errors in the flux density measurements of extended emission. Finally, the presence of several sources in a small area makes difficult to isolate the contribution of each source. Therefore, the spectral indices reported in this paper should be considered as rough estimates.

In addition to the compact emission of the two sources VLA 2A and VLA 2B, in the individual 3.6 cm maps of Figure 2.1 we also note the presence of several weak "knots" that
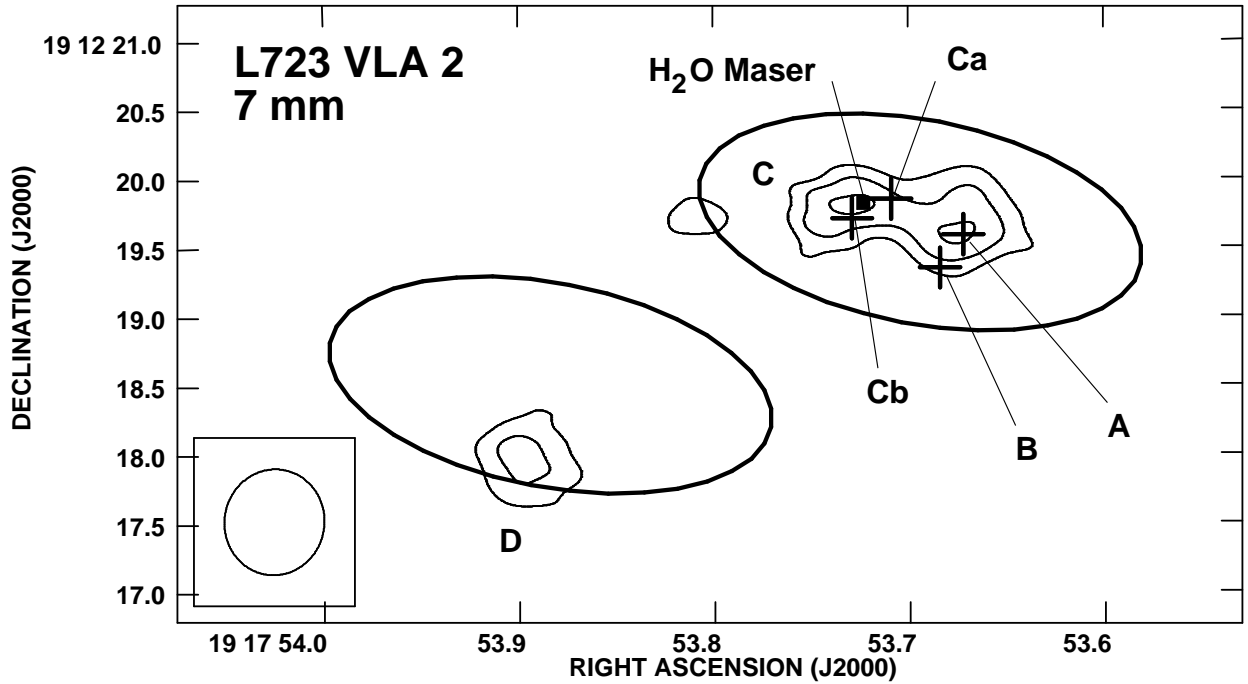
Figure 2.4 Naturally weighted map of the VLA 2 region at 7 mm, obtained by concatenating the uv data from VLA D, CnB, and C configurations. The synthesized beam of the map is $0\rlap{.}''77 \times 0\rlap{.}''73$ with a P.A. of $-10°$. Contour levels are $-4, -3, 3, 4$, and 5 times the rms of the map, 93 μJy beam^{-1}. Crosses mark the positions of VLA 2A, VLA 2B, VLA 2Ca, and VLA 2Cb at 3.6 cm. The filled square marks the position of the water maser detected by Girart et al. (1997). Ellipses are centered at the nominal positions of the 1.35 mm sources detected by Girart et al. (2009), and their size corresponds to the synthesized beam of the SMA.

could be tracing extended emission. In order to gain sensitivity to extended structures, we have concatenated all the 3.6 cm uv data and made a naturally weighted "All-Epochs" map, that is shown in Figure 2.3b. This map shows extended emission with a P.A. of $\sim$115°, where we identify the knots w1, w2, e1, and e2, that can also be seen in several of the individual epoch maps (Fig. 2.1). The extended emission seems to emanate from VLA 2A, the northern component of the double source, since a line running through the major axis of this extended emission is centered close to the position of VLA 2A (see Fig. 2.3b), which is the strongest source along this direction. The P.A. of this extended emission ($\sim$115°) coincides with that of the system of HH objects observed in the region (López et al. 2006), suggesting that VLA 2A is a YSO that is driving these HH objects. The P.A. of the extended emission is also similar to that of the symmetry axis of the larger pair of CO outflow lobes ($\sim$100°), thus suggesting that VLA 2A is also associated with this lobe pair.

We interpret the extended radio emission as tracing an ionized jet that originates at the position of VLA 2A, and where the knots w1, w2, e1, and e2 would be tracing electron density enhancements produced by shock-ionization. We do not detect clear proper motions associated

with these knots from one epoch to another, setting an upper limit to the proper motion velocity of the knots of $\sim$27 km s^{-1} (however, due to the coarse temporal sampling and the low signal-to-noise ratio of the knots in the individual epoch maps, they are difficult to identify from one epoch to another, and we cannot discard higher proper motion velocities). This suggests that these knots have been excited by the interaction of the jet of VLA 2A with dense, stationary clumps in the surrounding gas.

We also note the detection of the faint knots, n1 (in the 2000.9 image; Fig. 2.1f) and s1 (in the 1997.0 image; Fig. 2.1b). We interpret these two knots as shock-ionized gas associated with episodic ejections of material. Their location, nearly aligned with source VLA 2B, at a P.A. $\simeq 20°$, is consistent with being excited by a jet coming from this source. The P.A. of this jet is similar to that of the smaller pair of CO outflow lobes ($\sim$30°) and therefore, we tentatively propose VLA 2B as its exciting source.

In summary, we detected two compact 3.6 cm sources, VLA 2A and VLA 2B, separated by $\sim$0.3 along a P.A. of $\sim$150°. We also detected extended 3.6 cm emission, centered on VLA 2A, and along a P.A. of $\sim$115°, that coincides with the P.A of the system of HH objects in the region and is similar to that of the larger pair of CO outflow lobes. The spectral index of VLA 2A in the 3.6 cm to 7 mm wavelength range, is consistent with this source tracing the origin of an ionized radio jet with a possible contribution from dust. Therefore, we conclude that VLA 2A is an embedded YSO associated with a radio jet; it is also the likely exciting source of the system of HH objects and of the larger pair of lobes of the CO outflow observed in the region. We identify several knots (w1, w2, e1, and e2) distributed along the extended 3.6 cm emission, at both sides of VLA 2A. Since these knots are much weaker than VLA 2A and are aligned along the axis of the extended emission we interpret them as tracing electron density enhancements in the jet from VLA 2A rather than tracing the location of other YSOs. The lack of clear proper motions suggests that these knots have been excited by the interaction of the jet with dense, stationary clumps in the gas surrounding VLA 2A. The compact source VLA 2B has a flux density comparable to that of VLA 2A and both sources are aligned along a P.A. of $\sim$150°, a direction where there are no indications of outflow activity. Therefore, we interpret VLA 2B as a second embedded YSO, constituting a close (projected separation of 90 AU) binary system. Neither VLA 2A nor VLA 2B show noticeable proper motions; this result strongly suggests that these sources do not trace high-velocity material, and is consistent with these sources being YSOs. Unfortunately, with the current data it is not possible to obtain a precise enough measure of proper motions that would allows us to derive possible orbital motions, as has been done in other sources (e.g., Loinard et al. 2002); this kind of data could be helpful to confirm that this is a binary system. Also, there are no high angular resolution data outside the centimeter wavelength range that allow us to characterize the individual spectral energy distribution of each component in order to establish the evolutionary status of the sources and to confirm their nature as YSOs. Therefore, these sources are good targets for future observations with the EVLA and ALMA. We also detect in the single epoch images two faint knots (n1 and s1) nearly aligned with the source VLA 2B along a P.A. of $\sim$20°, that is similar

Table 2.5.   Monitoring of VLA 1 at 3.6 cm[a]

| | Position (J2000)[b] | | | Flux Density | Deconvolved Size | | |
| | | | | | Major Axis | Minor Axis | P.A. |
Epoch	RA	DEC	Error	(mJy)	(arcsec)	(arcsec)	(deg)
1995.6	19 17 52.922	+19 12 08.85	0″01	0.36 ± 0.02	0.11	0.10	179
1997.0	19 17 52.923	+19 12 08.85	0″01	0.38 ± 0.02	0.13	0.00	37
1998.2	19 17 52.922	+19 12 08.86	0″01	0.34 ± 0.02	0.12	0.04	179
1998.4	19 17 52.922	+19 12 08.86	0″01	0.31 ± 0.02	0.11	0.05	179
1999.5	19 17 52.923	+19 12 08.86	0″01	0.34 ± 0.03	0.13	0.07	179
2000.9	19 17 52.923	+19 12 08.85	0″01	0.34 ± 0.01	0.13	0.00	30

[a]Parameters derived from Gaussian fits to the 3.6 cm naturally weighted maps that have been restored with an average circular beam of HPBW=0″29.

[b]Units of right ascension are hours, minutes, and seconds, and units of declination are degrees, arcminutes, and arcseconds.

to the P.A. of the smaller pair of CO outflow lobes. We tentatively interpret these two knots as shock-ionized gas associated with episodic ejections from VLA 2B, that could be the driving source of these knots as well as of this pair of CO outflow lobes.

2.3.2   Other Radio Sources Detected in the Region

In addition to VLA 2A, our 7 mm image (Fig. 2.4) shows emission from other two sources. One of them, that we will refer to as VLA 2C, coincides with the position of the water maser emission detected by Girart et al. (1997) and Furuya et al. (2003). The coincidence of this source with the water maser suggests that VLA 2C is a YSO. At 7 mm, the source VLA 2C appears elongated, with a deconvolved size of $1''2 \pm 0''2$ with a P.A. $\simeq 90° \pm 7°$. At 3.6 cm, we detect weak extended emission that coincides with the source detected at 7 mm. The 3.6 cm emission shows two peaks, that we call VLA 2Ca and VLA 2Cb. With the current data it is unclear if these two peaks actually correspond to two objects or to a single extended source. Sensitive high angular resolution multiwavelength observations would be required to further define the nature of this emission. From the total flux density at 3.6 cm (VLA 2Ca + VLA 2Cb) and 7 mm (see Table 2.2), we estimate a spectral index of 1.5±0.4 for VLA 2C, a value suggestive of thermal emission from a YSO (see discussion in §2.3.1).

The third 7 mm source, VLA 2D, is located $\sim3''5$ from VLA 2A and does not have a detected 3.6 cm counterpart. However, this source is located within $\sim0''6$ of the nominal position of a 1.35 mm source detected by Girart et al. (2009) with the Submillimeter Array (SMA) (see Fig. 2.4). Given that the beam size of the SMA observations is $3''3 \times 1''5$ (P.A.=79°), we suggest that VLA 2D is the 7 mm counterpart of the 1.35 mm source. From the total flux density at 7 mm of VLA 2D, and adopting a 4σ upper limit to the 3.6 cm flux density, we estimate a lower limit to the spectral index of this source of ~2.0 in this wavelength range, suggesting that the 7 mm emission is dominated by thermal dust emission. Additionally, the 1.35 mm source seems to be associated with an elongated SiO structure, probably tracing material shocked by a high velocity flow (Girart et al. 2009), suggesting that this source is associated with a YSO.

In addition to the sources VLA 2A, VLA 2B, VLA 2C, and VLA 2D that appear located

at the center of the L723 outflow, our 3.6 cm images detect the source VLA 1, first reported by Anglada et al. (1991), and located $\sim 15''$ SW of the position of VLA 2A. The source VLA 1 appears always compact (deconvolved size $\leq 0''.13$; see Table 2.5) with a roughly constant flux density consistent at all epochs with a value of 0.36±0.02 mJy (see Table 2.5). We have not detected this source at 7 mm up to a 4σ level of 0.32 mJy. With our 3.6 cm flux density and the 7 mm upper limit, we estimate for VLA 1 a spectral index $\alpha \leq -0.1$, a value consistent with the spectral index $\alpha = -0.3 \pm 0.2$ measured by Anglada et al. (1996) between 3.6 and 6 cm. As discussed by Anglada et al. (1996) and Girart et al. (1997), this source is most probably a radio-emitting, optically-obscured T Tauri star located very near to the denser part of the molecular cloud. Our accurate astrometry indicates that this compact source does not show noticeable proper motions, with a position displacement $< 0''.03$ (3σ) over the 5.3 yr period covered by our observations (see Table 2.5). Since a total proper motion displacement of $\sim 0''.03$ is expected for an object embedded in the L723 cloud (assuming a distance of 300 pc and the Brand & Blitz 1993 model of galactic rotation), this result is compatible with VLA 1 belonging to the L723 cloud. However, the possibility that VLA 1 is a line-of-sight source not directly associated with the molecular cloud is not discarded. The remaining radio sources (VLA 2A, VLA 2B, VLA 2C, and VLA 2D) discussed in this paper are embedded in regions of extended radio emission and are associated with ejecta, which does not allow a precise determination of their possible proper motions.

2.3.3   The Morphology of the Outflow in L723: Three Bipolar Outflows?

In the maps of Avery et al. (1990), the L723 CO outflow shows a four-lobe morphology with a large pair of bipolar lobes along a P.A. of $\sim 100°$ and a smaller pair of bipolar lobes along a P.A. of $\sim 30°$. As discussed in the previous sections, our radio continuum data suggest that a multiple system of at least four YSOs is present, within a region of ~ 1200 AU, at the intersection of the axes of symmetry of the two pairs of CO lobes. Furthermore, in §2.3.1 we discussed the results that led us to propose that VLA 2A is related to the excitation of the larger pair of CO lobes, while VLA 2B could be driving the smaller pair of CO lobes.

Nevertheless, the interferometric maps of Lee et al. (2002) (obtained with higher angular resolution than the maps of Avery et al. 1990) reveal additional details of the CO outflow structure (see Fig. 2.5a). As can be seen in this figure, the smaller pair of CO lobes shows a compact shape with a well defined axis at P.A. $\simeq 30°$. On the other hand, the shape of the larger pair of CO lobes appears clumpy, with only a few weak CO emission knots near the symmetry axis of this lobe pair (at P.A. $\simeq 100°$), and most of the emission concentrated at both sides of this central axis, roughly at P.A. $\simeq 90°$ and P.A. $\simeq 115°$. The distribution of the CO emission of this larger lobe pair was interpreted by Lee et al. (2002) as tracing the limb-brightened cavity walls of a bipolar outflow with a P.A. $\simeq 100°$. However, we note that the distribution of the CO emission at both sides of the central axis (P.A. $\simeq 100°$) of this lobe pair is asymmetric. The emission at P.A. $\simeq 115°$ starts at the center of the outflow (the position of VLA 2) and is stronger than the emission at P.A. $\simeq 90°$, which shows a gap, with the bulk of the emission
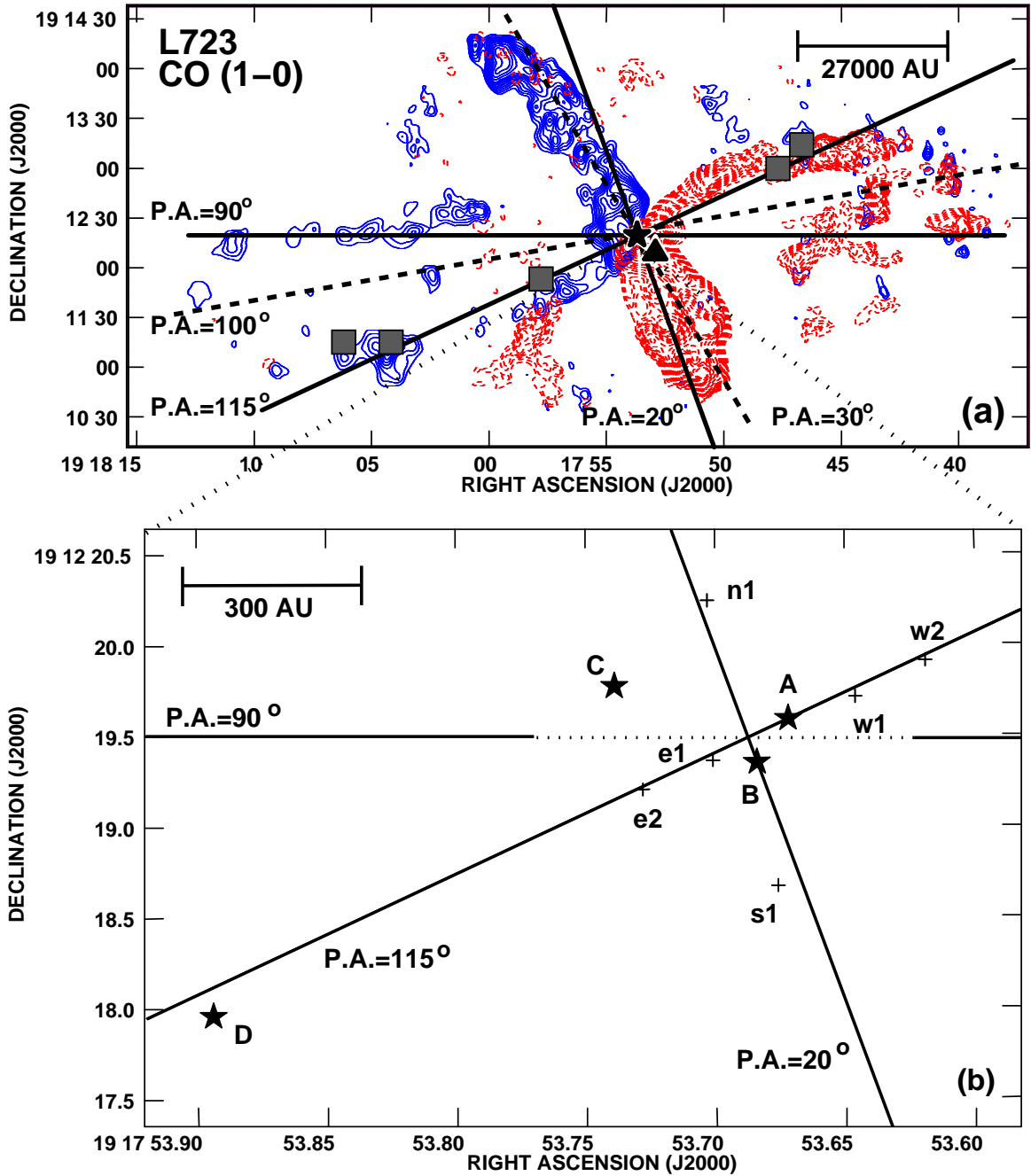
Figure 2.5 **(a)** Map of the high velocity CO ($J=1{\to}0$) emission in L723 (Lee et al. 2002). Redshifted emission (dashed contours) is integrated from 11 to 31 km s^{-1} and blueshifted emission (solid contours) is integrated from -10 to 10 km s^{-1}. Dashed lines mark the position angles of the axes of the bipolar outflows proposed by Lee et al. (2002). Solid lines mark the position angles of the axes of the three bipolar outflows proposed in this paper. Herbig-Haro objects (López et al. 2006) are marked by boxes. The star symbol marks the position of VLA 2 and the triangle marks the position of VLA 1 (Anglada et al. 1991, 1996). **(b)** A schematic depiction of the proposed outflow axes and the multiple system of YSOs at the center of the L723 outflow. Star symbols mark the positions of the suspected YSOs: VLA 2A, VLA 2B, VLA 2C, and VLA 2D. The three axes have the directions of the outflows proposed in this paper. The crosses mark the positions of the knots detected at 3.6 cm.

apparently starting $\sim 1'$ away from the outflow center. Furthermore, the P.A. of 115° coincides with that of the extended radio emission associated with VLA 2A and with that of the system of HH objects.

These considerations led us to propose a new interpretation of the high-velocity CO emission in L723 in terms of three bipolar outflows. One bipolar outflow at P.A. $\simeq 30°$, that could be driven by VLA 2B. A second bipolar outflow at P.A. $\simeq 115°$, which is associated with a system of HH objects and shock-ionized extended radio continuum emission with the same position angle, that is driven by VLA 2A. Finally, a third bipolar outflow at P.A. $\simeq 90°$, whose exciting source is uncertain. The lobes of the proposed outflows at P.A. $\simeq 30°$ and P.A. $\simeq 115°$ appear well "connected" with the outflow center, suggesting recent outflow activity in these directions. On the contrary, the lobes of the outflow at P.A. $\simeq 90°$ are weaker and well detached from the central region, suggesting that they resulted from activity taking place in the past. Therefore, we speculate that this outflow at P.A. $\simeq 90°$ could be a "fossil" outflow in the sense that its exciting source has not been active in the recent past. The motion observed will then be the result of momentum conservation of the gas accelerated when the exciting source was active. A similar fossil molecular outflow has been proposed to exist in the molecular cloud B5 (Yu, Billawala, & Bally 1999).

2.4   Conclusions

Our high angular resolution 3.6 cm and 7 mm continuum observations towards the previously known source VLA 2, at the center of the L723 multipolar CO outflow, have revealed a group of at least four YSOs within a region of $\sim 4''$ (1200 AU) in size. The size of this region is comparable with the size of the region where Girart et al. (1997) found a local heating of the high density gas. Two of our continuum sources, VLA 2A and VLA 2B, form a close radio binary whose components are separated by $\sim 0\farcs 29$ (~ 90 AU). Another source, VLA 2C, is associated with a water maser, and a fourth source, VLA 2D, that we only detect at 7 mm, appears to be the counterpart of a recently discovered 1.35 mm source.

We propose that the multipolar CO outflow in L723 could result from the superposition of at least three independent bipolar outflows with position angles of $\sim 115°$, $\sim 90°$, and $\sim 30°$, driven by three different YSOs. Our 3.6 cm observations suggest that VLA 2A is associated with an ionized jet at a position angle of $\sim 115°$. We propose that this is the exciting source of the system of HH objects previously detected in the region, as well as of a bipolar CO outflow with the same position angle. The presence of two 3.6 cm knots aligned with VLA 2B at a P.A. of $\sim 20°$ suggests that VLA 2B could be the exciting source of the bipolar CO outflow at a P.A of $\sim 30°$. Finally, the third bipolar CO outflow, with a position angle of $\sim 90°$, seems to be a "fossil" outflow whose exciting source has not been very active in the recent past.

Bibliography

Anglada, G. 1996, ASP Conf. Ser., 93, 3

Anglada, G., Estalella, R., Rodríguez, L.F., Torrelles, J.M., López, R., & Cantó, J. 1991, ApJ, 376, 615

Anglada, G., Rodríguez, L.F., & Torrelles, J.M 1996, ApJ, 473, 123

Anglada, G., Rodríguez, L.F., & Torrelles, J.M. 1998, ASP Conf. Ser., 132, 303

Avery, L.W., Hayahi, S.S., & White, G.J. 1990, ApJ, 357, 524

Ávila, R., Rodríguez, L. F., & Curiel, S. 2001, RevMexAA, 37, 201

Bachiller, R., Fuente, A., & Tafalla, M. 1995, ApJ, 445, 51

Bally, J., O'Dell, C.R., & McCaughrean, M.J. 2000, AJ, 119, 2919

Beltrán, M.T., Estalella, R., Ho, P.T.P., Calvet, N., Anglada, G., & Sepúlveda, I. 2002, ApJ, 565, 1069

Brand, J., & Blitz, L. 1993, A&A, 275, 67

Briggs, D.S., 1995, Ph.D. thesis, New Mexico Institute of Mining and Technology

Cabrit, S. & André, P. 1991, ApJ, 379, 25

Cernicharo, J., & Reipurth, B. 1996, ApJ, 460, 57

Dartois, E., Pontoppidan, K., Thi, W.-F., & Muñoz Caro, G.M., 2005, A&A, 444, 57

Estalella, R., Anglada, G., Rodríguez, L.F., & Garay, G. 1991, ApJ, 371, 626

Franco-Hernández, R. & Rodríguez, L.F. 2003, RevMexAA, 39, 107

Furuya, R.S., Kitamura, Y., Wootten, A., Claussen, M.J., & Kawabe, R. 2003, ApJS, 144, 71

Girart, J.M., Estalella, R., Anglada, G., Torrelles, J.M., Ho, P.T.P., & Rodríguez, L.F. 1997, ApJ, 489, 734

Girart, J.M., Rao, R., & Estalella, R., 2009, ApJ, 694, 56

Goldsmith, P.F., Snell, R.L., Hemeon-Heyer, M., & Langer, W.D. 1984, ApJ, 286, 599

Gueth, F., Schilke, P., & McCaughrean, M.J. 2001, A&A, 375, 1018

Hodapp, K. 1994, ApJS, 94, 615

Hodapp, K., & Ladd, E.F. 1995, ApJ, 453, 715

Hirano, N., Hayashi, S.S., Umemoto, T., & Ukita, N. 1998, ApJ, 504, 334

Lee, C.-F., Mundy, L.G., Stone, J.M., & Ostriker, E.C. 2002, ApJ, 576, 294

López, R., Estalella, R., Gómez, G., & Riera, A. 2006, A&A, 454, 233L

Loinard, L., Rodríguez, L.F., D'Alessio, P., Wilner, D.J., & Ho, P.T.P. 2002, ApJ, 581, L109

Mizuno, A., Fukui, Y., Iwata, T., Nozawa, S., & Cantó, J. 1990, ApJ, 356, 184

Palacios, J. & Eiroa, C. 1999, A&A, 346, 233

Porras, A., Rodríguez, L.F., Cantó, J., Curiel, S., & Torrelles, J.M. 2002, RevMexAA, 38, 187

Reipurth, B., Yu, K.C., Rodríguez, L.F., Heathcote, S., & Bally, J. 1999, A&A, 352, 83

Vrba, F.J, Luginbuhl, C.B., Strom, S.E., Strom, K.M., & Heyer, M.H. 1986, AJ, 92, 633

Yu, K. C., Billawala, Y., & Bally, J. 1999, AJ, 118, 2940

Zapata, L.A., Rodríguez, L.F., Kurtz, S.E., O'Dell, C.R., & Ho, P.T.P., 2004, ApJ, 610, L121

3

High Angular Resolution Observations of the HL/XZ Tau Region*

In this chapter we present 7 mm and 1.3 cm high angular resolution observations of the HL/XZ Tau region made with the VLA. At 7 mm, the emission from HL Tau seems to be arising in a clumpy disk with radius of order 25 AU. The 1.3 cm emission from XZ Tau shows the emission from a binary system with 0."3 (42 AU) separation, known from previous optical/IR observations. However, at 7 mm, the southern radio component resolves into a binary with 0."09 (13 AU) separation, suggesting that XZ Tau is actually a triple star system. We suggest that the remarkable ejection of gas from the XZ Tau system observed with the HST may be related to a periastron passage of this newly discovered close binary system.

3.1 Introduction

The region encompassing the stars HL/XZ Tau, in the northeastern part of the L1551 dark cloud, has been the subject of many studies over the years. This region lies at a distance of 140 pc (e.g., Kenyon et al. 1994; Torres et al. 2009) and it is particularly rich in HH jets, being one of the regions where this phenomenon was first identified (Mundt & Fried 1983).

HL Tau is one of the most intensively studied T Tauri stars. Since the first proposal that this star is associated with a nearly edge-on circumstellar disk (Cohen 1983), numerous studies have been carried out in order to image the proposed disk (e.g., Sargent & Beckwith 1991; Wilner et al. 1996; Looney et al. 2000). This star has been proposed as the exciting source of a molecular outflow (e.g., Torrelles et al. 1987; Monin et al. 1996). HL Tau is also the source of a collimated optical jet-counterjet system that has been extensively studied (e.g., Mundt et al. 1990; Rodríguez et al. 1994; Anglada et al. 2007). Very recently, Greaves et al. (2008) presented high angular resolution maps at 1.3 cm of the jet-disk system in HL Tau. These authors reported the detection of a weak 1.3 cm source which they propose is a 14 M_J

proto-planet orbiting at a radius of ∼65 AU around HL Tau.

XZ Tau, located ∼25″ to the east of HL Tau, is a close binary system composed of a T Tauri star and a cool companion separated by 0.″3 (Haas et al. 1990). XZ Tau is also the source of an optical outflow, as revealed, e.g., by the studies of Mundt et al. (1990). The spectacular sequence of Hubble Space Telescope (HST) images of Krist et al. (1999) shows evidence of the expansion of nebular emission, moving away from XZ Tau with a velocity of ∼70 km s^{-1}. This bubble of nebular emission is different from the collimated jets seen in other young stars, for example HL Tau. Recent new HST observations (Krist et al. 2008) revealed a succession of bubbles and a fainter counterbubble. In addition, they reveal that both components of the XZ Tau binary are also driving collimated jets. Krist et al. (2008) proposed that the bubble is the result of a large velocity pulse in the collimated jet driven by the southern component of the XZ Tau system.

In this chapter, we present the results of sensitive high-angular resolution VLA observations at 1.3 cm and 7 mm of HL/XZ Tau. These observations allowed us to map the dust emission from the disk of HL Tau at scales of ∼7 AU and reveal that XZ Tau is actually a triple-star system with the southern optical component resolved into a close binary with a separation of only 13 AU.

3.2 Observations

The 7 mm data were taken in A, B and D configurations (VLA Project Codes: AC0763, AC0850 and AC0816). Total on-source integration times were ∼3 h at A Configuration (observed in three runs during 2004 October 15, 17 and 26), ∼1 h at B Configuration (2006 September 19), and ∼1.5 h at D Configuration (observed in two runs during 2006 January 20 and 22). The fast-switching technique was used for all the observations. Phase and flux calibrators were 0431+175 and 3C286, respectively. The same phase center was used for all the observations.

We also used archive continuum data at 1.3 cm taken with the VLA in its A Configuration (VLA Project Code: AG0711) with a total on-source integration time of ∼12 h (observed in two runs during 2006 March 12 and April 1). Phase and flux calibrators were 0431+206 and 3C286, respectively. The Pie Town antenna was used originally in these observations, but we did not include it in our analysis.

Data editing and calibration were carried out using the AIPS package of NRAO, following the standard high-frequency VLA procedures. Primary beam corrections were applied using the task PBCOR of AIPS.

Maps at 7 mm were made by concatenating the data from all the configurations (A, B and D). This allowed us to improve by ∼20% the signal-to-noise ratio of the A configuration data without significant detriment of the angular resolution. The 7 mm map of HL Tau shown here was made using data with baselines >150 kλ in order to resolve out extended emission that surrounds HL Tau. The nature of this extended emission is not fully understood, but probably originates from diffuse dust in the region. The 1.3 cm map of HL Tau shown in Greaves et al. (2008) was obtained from the same data, and, as expected, is very similar to our 1.3 cm map.

The rms noises of the natural weighting maps were 13 μJy at 1.3 cm, and 50 μJy at 7 mm. Synthesized beams are $\sim0\rlap{.}''10$ at 1.3 cm and $\sim0\rlap{.}''05$ at 7 mm. Bandwidth smearing at the position of XZ Tau degrades the resolution by $\sim5\%$ in the radial direction, which does not affect our analysis.

This region has a known proper motion of $0\rlap{.}''025\pm0\rlap{.}''0035$ yr^{-1} (Rodríguez et al. 2003), so we shifted the 2006 1.3 cm data by $0\rlap{.}''04$ to align them with the 2004 7 mm data (with uncertainties of $0\rlap{.}''005$ in proper motions and $0\rlap{.}''01$ in absolute astrometry at each epoch).

3.3 Results and Discussion

3.3.1 HL Tau: Planet formation in the circumstellar disk?

In Figure 3.1a we show a superposition of the 7 mm emission of HL Tau (contours) over the 1.3 cm map (colors). At 1.3 cm, HL Tau shows a quadrupolar morphology consisting of two nearly perpendicular structures at position angles (P.A.s) of $\sim50°$ and $\sim140°$. As previously noted by Greaves et al. (2008), the alignment of the 1.3 cm emission at P.A.$\simeq50°$ with the optical jet of HL Tau (e.g. Anglada et al. 2007), suggests that the 1.3 cm emission at this P.A. is tracing free-free emission from the shock-ionized gas at the base of the flow. In contrast, the 1.3 cm emission at P.A.$\simeq140°$ is most probably tracing thermal dust emission from a circumstellar disk perpendicular to the outflow. This is more evident in our 7 mm map (see Fig. 3.1a), where the emission shows an elongated morphology with a P.A. of $\sim140°$ (perpendicular to the jet) and a size of ~50 AU. The positions of the 1.3 cm and 7 mm maxima are nearly coincident and define the center of the radio jet.

We also detected two weak compact 1.3 cm features, one $\sim0\rlap{.}''4$ to the NW (at a level of 3-σ) and the other $\sim0\rlap{.}''4$ to the S (at a level of 4-σ) of the 1.3 cm emission peak (see Fig. 3.1a). Greaves et al. (2008) identified the 1.3 cm NW feature with a 1.4 mm source detected by Welch et al. (2004), obtaining a spectral index of 2.5 in this wavelength range. They proposed that the 1.3 cm NW feature is dust emission arising from a proto-planet with a mass of 14 M$_J$ and orbiting around HL Tau at a radius of ~65 AU. The other 1.3 cm feature to the S, although somewhat stronger than the NW feature, was not discussed by these authors. As can be seen in Figure 3.1a, we have not detected 7 mm emission at the position of the proto-planet candidate, with a 3-σ upper limit level of ~0.15 mJy. This upper limit and the 1.3 cm flux density of Greaves et al. (2008) implies a spectral index <1, suggesting free-free rather than dust emission. On the other hand, the spectral index of 2.5 between 1.3 cm and 1.4 mm obtained by Greaves et al. (2008) would imply a 7 mm flux density of 0.5 mJy, well above our 3-σ upper limit. Additional, high angular resolution observations in the mm range are necessary to clarify the true nature of this source.

In Figure 3.1b we show an intensity profile of the 7 mm emission along the major axis of the disk. As can be seen in Figures 3.1a and 3.1b, the 7 mm emission is knotty and asymmetric. The proposed disk extends ~25 AU to the SE, and shows a gap at a radius of ~10 AU and the emission to the NW appears truncated at a radius of ~12-15 AU. The gap and the truncation
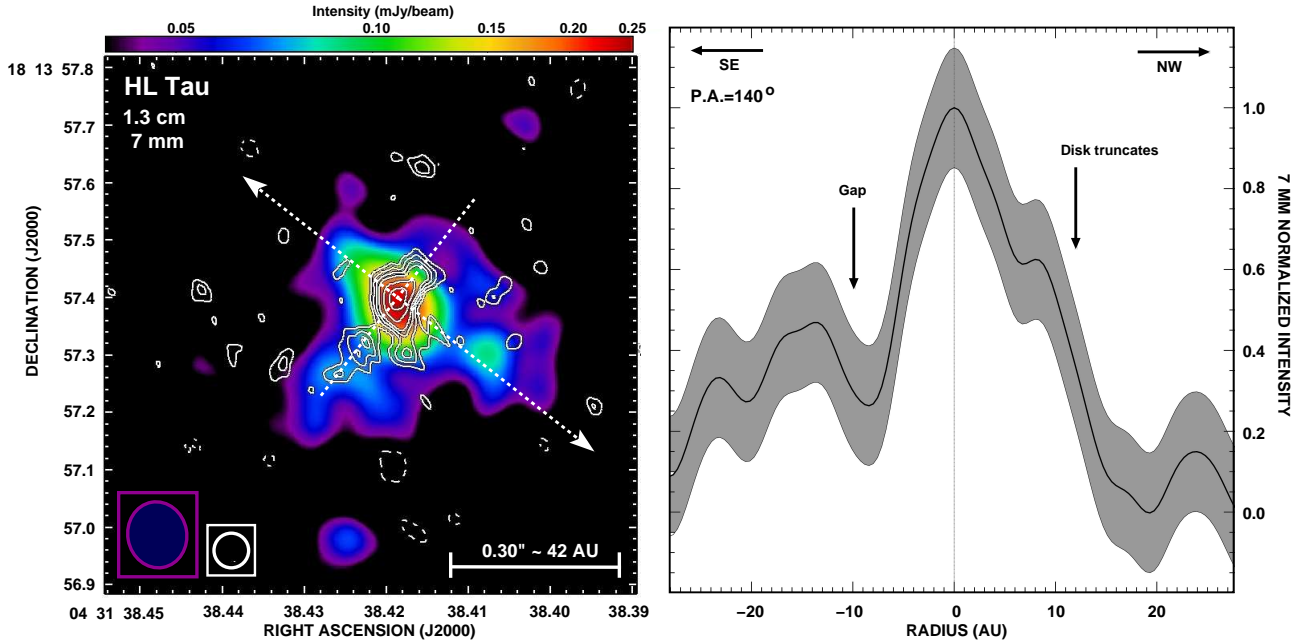
Figure 3.1 **(a)** Superposition of the 7 mm map (contours) over the 1.3 cm continuum map (color scale) of HL Tau. Contours at 7 mm are -3, 3, 4, 5, 6, 8, 10, 12, 14, 18, 22, 26 and 32 times the rms of the map, 50 μJy. The dashed lines mark the directions of the optical jet (P.A.=50°) and the disk (P.A.=140°). The half power contour of the 1.3 cm (filled ellipse) and 7 mm (empty ellipse) beams are shown in the bottom left corner. **(b)** A 7 mm intensity profile along the major axis of the disk (P.A.=140°), obtained by averaging the emission at $\pm 0\rlap{.}''05$ from the axis marked in (a). The intensity error is indicated by the thickness of the profile. The disk truncates at a radius of $\sim$12 AU to the NW, and shows a gap at a radius of $\sim$10 AU to the SE. We speculate that these features could be related to the formation of a proto-planet (see text).

are probably related to a decrease of the density in the disk. Thus, since the disk is observed nearly edge-on (e.g. Cohen 1983), this gap could be associated with an annulus of low density in the disk with a radius of $\sim$10-15 AU, similar to the radius of the orbit of Saturn, or twice the orbit of Jupiter. Such structures are expected to form as a consequence of the accretion of a planetary object forming in the disk (see, e.g. Bryden et al. 1999). Therefore, the gap and the truncation of the disk detected in our 7 mm map could be related to the formation of a proto-planet. Alternatively, this gap could be due to tidal truncation in a binary system (e.g., Pichardo et al. 2005) as in the case of HH30 (Anglada et al. 2007, Guilloteau et al. 2008). However, with the present data, these suggestions are very speculative, and should be confirmed by subsequent observations and/or modelling of the disk of HL Tau.

3.3.2 XZ Tau: A triple system of YSOs

In Figure 3.2a we show the 3.6 cm continuum map (angular resolution $\simeq 0\rlap{.}''3$) of XZ Tau, obtained by Rodríguez et al. (1994), where a single radio continuum source was detected. Figures 3.2b and 3.2c show our 1.3 cm and 7 mm maps, respectively. At 1.3 cm (angular resolution $\simeq 0\rlap{.}''1$), XZ Tau is resolved in two radio continuum sources (labeled N and S) separated
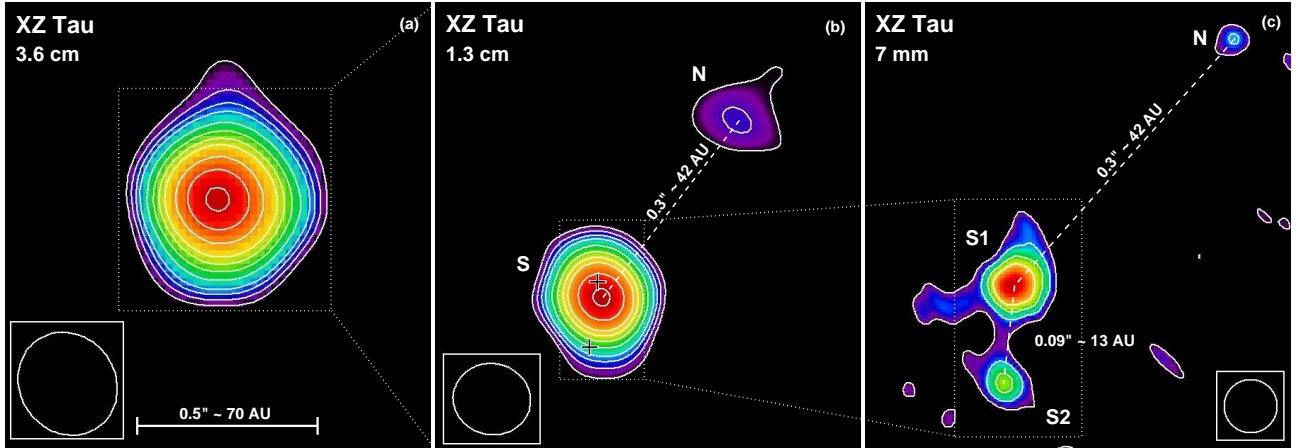
Figure 3.2 Radio continuum maps of XZ Tau at 3.6 cm (a), 1.3 cm (b) and 7 mm (c). The contours are -3, 3, 4, 5, 6, 8, 10, 12, 14, 18, 22 and 26 times the rms of each map, 7 μJy (3.6 cm), 13 μJy (1.3 cm) and 50 μJy (7 mm). At 3.6 cm a single radio source is detected. The 1.3 cm map shows two continuum sources, labeled as N and S. The source S is marginally resolved, showing a slight elongation to the south. Crosses mark the positions of the two components S1 and S2 detected at 7 mm. At 7 mm, the source N is detected as a weak source, and the 1.3 cm source S, is resolved in two components, S1 and S2.

Table 3.1.   Components of the XZ Tau triple system

Radio Component	Optical Component	Position (J2000)[a]			Flux Density (mJy)[a]		Spectral Index	Emission Mechanism
		RA	DEC	Error	1.3 cm	7 mm		
N	XZ Tau B	04 31 40.0751	18 13 57.079	0$\farcs$006	0.14 ± 0.03	0.3 ± 0.2	1.1 ± 1.0	Free-free
S1	XZ Tau A	04 31 40.0891	18 13 56.853	0$\farcs$005	0.33 ± 0.03[b]	1.2 ± 0.2	1.9 ± 0.3	Free-Free + Dust
S2	XZ Tau C[c]	04 31 40.0899	18 13 56.762	0$\farcs$008	0.08 ± 0.03[b]	0.8 ± 0.2	3.4 ± 0.7	Dust

NOTES.- Units of right ascension are hours, minutes, and seconds, and units of declination are degrees, arcminutes, and arcseconds.

[a]Derived from Gaussian fits to the 7 mm natural weighting map (Epoch 2004.8). Errors in positions correspond to the relative positions. The error in the absolute position is estimated to be $\sim$0$\farcs$01.

[b]Flux density derived by fitting the marginally resolved 1.3 cm source S to two unresolved Gaussian sources.

[c]This component is probably a deeply embedded object undetectable at optical/IR wavelengths.

by $\sim$0$\farcs$3 with a P.A. of $\sim$143°. The 7 mm map (angular resolution $\simeq$0$\farcs$05), reveals that the 1.3 cm component S is actually a double radio source (that we label as components S1 and S2) with a separation of 0$\farcs$09 and a P.A. of -6°.

The size of the synthesized beam of the 1.3 cm map ($\sim$0$\farcs$1), slightly larger than the separation between the S1 and S2 components at 7 mm ($\sim$0$\farcs$09), does not allow to completely separate the emission of these components at 1.3 cm. However, the 1.3 cm source S is marginally resolved in our map, showing a slight elongation to the south. In Figure 3.2b we show the positions of the components S1 and S2 derived from the 7 mm map. As can be seen, most of the 1.3 cm emission seems to arise from component S1, since this is the source nearest to the peak of the 1.3 cm source S. The 1.3 cm source S can be fitted by two unresolved Gaussian sources separated by $\sim$0$\farcs$08, very similar to the separation between sources S1 and S2 in the 7 mm map.

In Table 3.1 we give the position (derived from the 7 mm map), flux density at 1.3 cm and

7 mm, and the spectral index for each component. For source N, we obtained a spectral index of 1.1 ± 1.0 consistent with free-free emission from this source. For source S as a whole, we obtained a "combined" spectral index of 2.5 ± 0.3 (obtained from the total flux density of the 1.3 cm source S, and the sum of the 7 mm flux densities of S1 and S2). This steep spectral index suggests a combination of free-free plus thermal dust emission. If we use the flux densities obtained from a double Gaussian fit to the 1.3 cm source S, for source S1 we obtain a spectral index of 1.9 ± 0.3 which suggests a combination of free-free plus thermal dust emission. In contrast, for S2 we obtain a spectral index of 3.4 ± 0.7 which suggests that the emission of this source is dominated by thermal dust emission.

As mentioned above, XZ Tau is known to be an optical/IR binary system with a separation of $\sim 0\overset{''}{.}3$. Following the notation of Krist et al. (2008), we will refer to the optical components of this system as XZ Tau A (the southern optical component) and XZ Tau B (the northern optical component). Krist et al. (1999, 2008) observed XZ Tau with the HST in several epochs, and detected a change in the P.A. of the binary due to orbital motions. According to this motion (~ -0.9 deg yr^{-1}) at the epoch of our radio observations, component XZ Tau B must be still located north of component XZ Tau A. Therefore, we identify the radio source N with the optical component XZ Tau B.

The identification of the two radio sources at the south (S1 and S2) with the other optical component (XZ Tau A) is not straightforward. One possibility is that both radio sources have optical emission that could not be resolved by the HST observations of Krist et al. (2008). However, another possibility is that only one of the radio sources is the counterpart of the optical component. In order to investigate these possibilities, we have plotted in Figures 3.3a and 3.3b the P.A. and separation of the optical binary measured in each epoch together with the P.A.s and separations between the different radio components measured from our 1.3 cm and 7 mm maps. As can be seen, the P.A. and separation between the radio sources N and S1 seems to be the only one compatible with the previous optical/IR data. This suggests radio source S1 as the sole counterpart to the optical component XZ Tau A; S2 is optically undetected. This is similar to the case of the close binary SVS 13, where both components are detected at cm wavelengths, but only one object is detected in the optical regime (Anglada et al. 2004). As we have discussed above, the radio emission of component S2 seems to be dominated by thermal dust emission. We believe that this source traces a star since if it not were gravitationally bound, it would quickly dissipate. The size of Sb is smaller than 7 AU, that expanding at only 1 km s^{-1}, will dissipate in only 30 years. Then, we conclude that this dust must be gravitationally bound to a star and it is most possibly an envelope or a disk. This suggests that source S2 is a more deeply embedded object so it is not surprising that it is optically very faint. Therefore, we propose that the radio source S2 is an optically invisible third component of the XZ Tau system. For consistency with the previous nomenclature, we call this component XZ Tau C.

In summary, the results derived from our 1.3 cm and 7 mm maps suggest that XZ Tau, previously known as a binary system, is actually a triple star-system (see Figs. 3.3c and 3.3d).
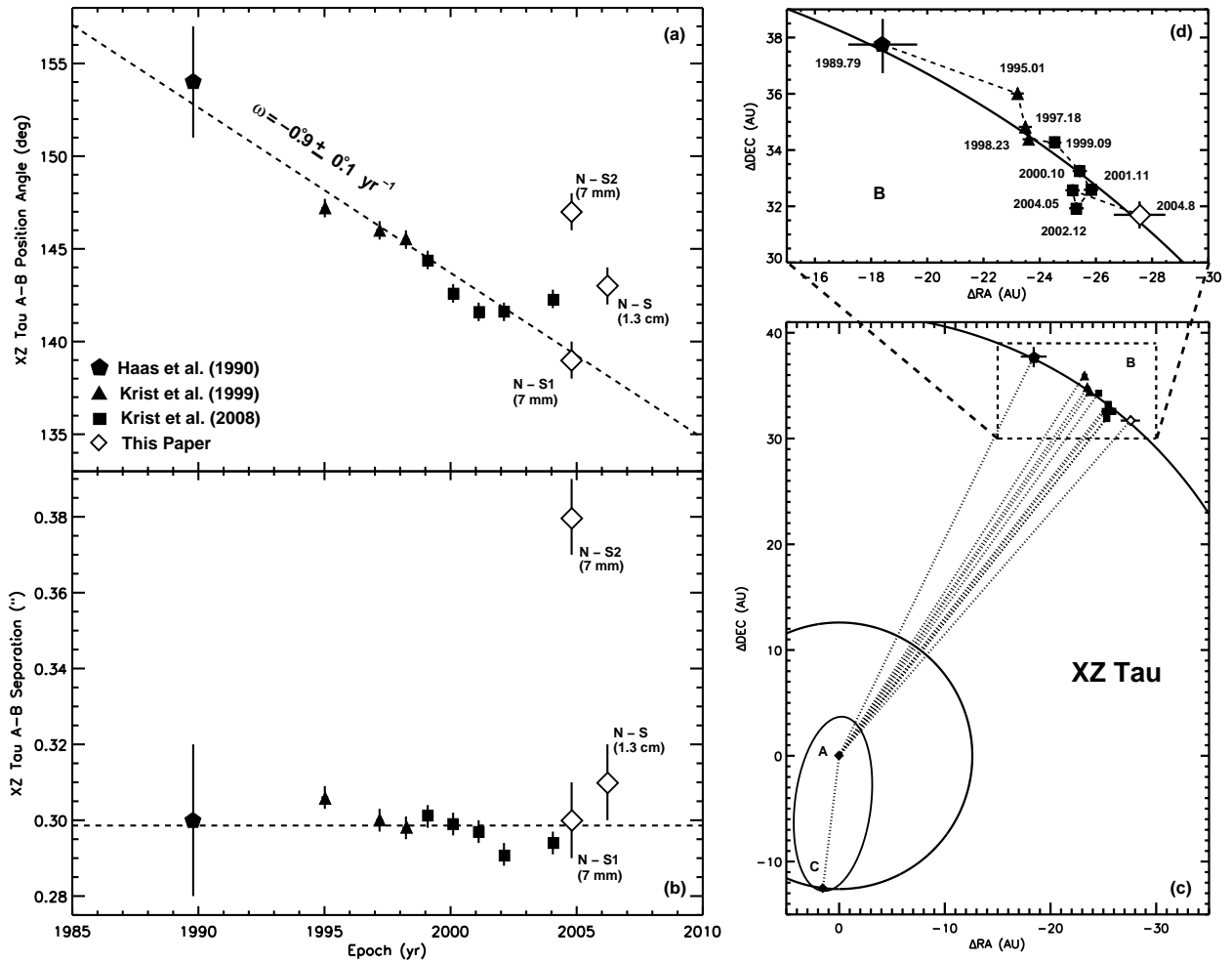
Figure 3.3 **(a)** Plot of the P.A. between the optical/IR components XZ Tau A and XZ Tau B vs. time (Haas et al. 1990; Krist et al 1999, 2008). The dashed line is a least squares fit to these data, and corresponds to an orbital angular velocity of -0.9 ± 0.1 degrees yr^{-1}. Three different P.A.s measured from our 1.3 cm and 7 mm maps are marked with diamonds. Only the P.A. between the 7 mm sources N and S1 seems to be compatible with the angular orbital velocity derived from the optical/IR data. This suggests that the source S1 is the radio counterpart of the optical component XZ Tau A. **(b)** Plot of the separation between the optical/IR components XZ Tau A and XZ Tau B vs time. The measurements are compatible with a constant separation of $0\farcs30\pm0\farcs01$. **(c)** and **(d)** A schematic representation of the XZ Tau triple system. The positions of XZ Tau B relative to XZ Tau A, derived from the P.A. and separation measurements of Haas et al. (1990), Krist et al (1999, 2008) and our data, are shown. The current data are compatible with a circular face-on orbit of XZ Tau B relative to XZ Tau A. In contrast, with only a single detection of the third component, XZ Tau C, we have no information about its orbital motion. Two hypothetical orbits (circular and elliptical) for XZ Tau C are shown.

The previously known optical/IR components, XZ Tau A and XZ Tau B, have 1.3 cm and 7 mm counterparts and are separated by 42 AU. A third component, XZ Tau C has been detected for the first time in our 1.3 cm and 7 mm maps, and is found to be a more deeply embedded object, probably undetectable at optical/IR wavelengths, that forms a close binary system with XZ Tau A with a separation of only 13 AU.

Each optical component of the XZ Tau system (A and B) is known to drive a collimated jet (Krist et al 2008). It has been proposed that the jet of XZ Tau A underwent a large velocity pulse approximately in 1980 (Krist et al. 2008) which, after shocking and heating the gas near the star, would result in the 70 km s^{-1} expanding bubble detected in the series of HST images of Krist et al. (1999, 2008). These authors explored the possibility that this ejection was triggered by the passage of component XZ Tau B very near component XZ Tau A. However, even assuming a very eccentric orbit (e$\simeq$0.9) they derived that the last approach of these components would have taken place in 1955, and thus, they discarded this possibility.

The discovery of a new companion, closer to XZ Tau A, suggests that it is once more feasible to consider the passage of this companion as the ejection trigger. If we assume a face-on, nearly circular (e$\simeq$0.1) orbit and a total mass of 1 M$_\odot$ (as suggested by the results of Krist et al. 1999 and White & Ghez 2001), we derive an orbital period of $\sim$40 yr. If at the time of our 7 mm observations (2004.8) the XZ Tau A-C system wass near apoastron, then the last periastron passage must have taken place one half-period before, i.e. nearly 1980, the date estimated for the ejection. Further observations are needed to produce a more accurate ephemeris for the XZ Tau system. The present results predict a new periastron passage around 2020, and then a new major ejection from XZ Tau A at this epoch.

3.4   Conclusions

We performed VLA high angular resolution observations at 1.3 cm and 7 mm of the HL/XZ Tau region. Our main conclusions can be summarized as follows:

- We detected dust emission at 7 mm associated with HL Tau. This emission seems to be arising in a clumpy disk with radius of $\sim$25 AU.

- The disk of HL Tau shows a density gap at a radius of $\sim$10-15 AU (similar to the radius of the orbit of Saturn) that may be the signpost of a growing protoplanet.

- The young star XZ Tau, known to be a binary with 42 AU separation from previous optical/IR observations, is actually a triple star system, since our radio observations reveal that one of the two components is resolved, in its turn, into a 13 AU binary.

- We propose that the remarkable ejection of gas from the XZ Tau system observed with the HST may be related to a periastron passage of this newly discovered close binary system.

Bibliography

Anglada, G., López, R., Estalella, R., Masegosa, J., Riera, A., & Raga, A. C. 2007, AJ, 133, 2799

Anglada, G., Rodríguez, L.F., Osorio, M., Torrelles, José M., Estalella, R., Beltrán, M.T., Ho, P.T.P. 2004, ApJ, 605, L137

Bryden, G., Chen, X., Lin, D. N. C., Nelson, R. P., & Papaloizou, J. C. B. 1999, ApJ, 514, 344

Cohen, M. 1983, ApJ, 270, L69

Greaves, J. S., Richards, A. M. S., Rice, W. K. M., & Muxlow, T. W. B. 2008, MNRAS, 391, L74

Guilloteau, S., Dutrey, A., Pety, J., Gueth, F. 2008, A&A, 478, 31

Haas, M., Leinert, C., & Zinnecker, H. 1990, A&A, 230, L1

Kenyon, S. J., Dobrzycka, D., & Hartmann, L. 1994, AJ, 108, 1872

Krist, J. E., et al. 1999, ApJ, 515, L35

Krist, J. E., Stapelfeldt, K. R., Hester, J. J., Healy, K., Dwyer, S. J., & Gardner, C. L. 2008, AJ, 136, 1980

Looney, L. W., Mundy, L. G., & Welch, W. J. 2000, ApJ, 529, 477

Monin, J.-L., Pudritz, R. E., & Lazareff, B. 1996, A&A, 305, 572

Mundt, R., Ray, T. P., Bührke, T., Raga, A. C., & Solf, J. 1990, A&A, 232, 37

Mundt, R., & Fried, J. W. 1983, ApJ, 274, L83

Pichardo, B., Sparke, L.S., Aguilar, L.A. 2005, MNRAS, 359, 521

Rodríguez, L. F., Cantó, J., Torrelles, J. M., Gómez, J. F., Anglada, G., & Ho, P. T. P. 1994, ApJ, 427, L103

Rodríguez, L.F., Curiel, S., Cantó, J., Loinard, L., Raga, A.C.; Torrelles, J.M. 2003, ApJ, 583, 330

Sargent, A. I., & Beckwith, S. V. W. 1991, ApJ, 382, L31

Torrelles, J. M., Anglada, G., Rodríguez, L. F., Cantó, L. F., & Barral, J. F. 1987, A&A, 177, 171

Torres, R.M., Loinard, L., Mioduszewki, A.J., & Rodríguez, L.F. 2009 submitted to ApJ.

Wilner, D. J., Ho, P. T. P., & Rodríguez, L. F. 1996, ApJ, 470, L117

White, R. J., & Ghez, A. M. 2001, ApJ, 556, 265

Welch, W. J., Webster, Z., Mundy, L., Volgenau, N., & Looney, L. 2004, in Bioastronomy 2002, IAU Symp. 213, eds. R. Norris, F. Stootman (ASP, San Francisco), p59

4

Multiple Jets and Disks in the NGC 2071 star-forming region*, Osorio, M., Anglada, G., D'Alessio, P., Rodíguez, L.F., Gómez, J.F., Torrelles, J.M., submitted to The Astrophysical Journal (2010)

In this chapter we present observations of the NGC 2071 star-forming region performed with the VLA and CARMA in the cm-mm wavelength range. We detected counterparts at 3.6 cm and 3 mm for three of the previously known sources (IRS 1, IRS 2, and IRS 3). We also report the detection of a previously unkonwn radio object (VLA 1). All these sources show a SED that seems to be dominated by free-free thermal emission at cm wavelengths, and thermal dust emission at mm wavelengths. This result suggests that all of the sources are associated with YSOs. Source IRS 1 shows a complex morphology at 3.6 cm. We proposed two possible explanations to this morphology: the result of changes in the direction of a jet due to interactions with dense ambient medium, or that we are actually observing a binary jet. Higher angular resolution observations at 1.3 cm support the second possibility, since a double source at this wavelength, that could corresponds to a binary system, is detected. Source IRS 3 shows a clear jet-like morphology at 3.6 cm, while the emission at 3 mm seems to be tracing a dusty circumstellar disk perpendicular to the radio jet. We have modeled the SED and spatial intensity profile of the 3 mm emission as an accretion disk. This has allowed us to constrain the mass of the central star in the range 3-6 $M_\odot$, the accretion rate in the range 2-4$\times10^{-7}$ $M_\odot$ yr^{-1}, and the radius of the disk in the range 150-175 AU.

---

*Carrasco-González, C.

4.1   Introduction

NGC 2071 is a reflection nebula located at a distance of 390 pc in the L1630 molecular cloud of Orion B (Anthony-Twarog 1982). Approximately $4'$ north of the NGC 2071 reflection nebula lies a $\sim 30''$ diameter infrared cluster, NGC 2071 IR (Persson et al. 1981), with a total luminosity of 520 $L_\odot$ (Butner et al. 1990), which has been identified as an intermediate-mass star-forming region.

A bipolar molecular outflow was been observed centered on the IR cluster. This powerful outflow, oriented in the NE-SW direction, extends $\sim 15'$ in length and ~ 120 km s^{-1} in velocity. It has been extensively studied in CO (Bally 1982; Snell et al. 1984; Scoville et al. 1986; Moriarty-Schieven 1989; Margulis & Snell 1989; Kitamura et al. 1990; Chernin & Masson 1992; Chernin & Welch 1995; Houde et al. 2001; Stojimirovic et al. 2008). In addition, shock-excited molecular hydrogen emission at 2.12 μm has also been observed, showing a spatial extent similar to the CO outflow. The H$_2$ traces several outflows in the region (Eisloffel 2000).

Emission at 6 cm have been detected associated with three of the IR sources (IRS 1, 2, and 3; Snell & Bally 1986). Sources IRS 1 and IRS 3 are also associated with 1.3 cm continuum and water maser emission (Torrelles et al. 1998). In IRS 1, both the 1.3 cm continuum and the water maser emission seem to be tracing a radio jet. Interestingly, in IRS 3, while the 1.3 cm emission clearly trace a radio jet, the water maser spots seems to be tracing a perpendicular compact disk with a radius of ~ 20 AU (Torrelles et al. 1998). In this chapter we present new high angular resolution observations in the cm to mm wavelength range of the NGC 2071-IR cluster. We used the VLA and CARMA in their most extended configurations.

4.2   Observations

4.2.1   VLA Observations

Continuum observations at 3.6 cm were made with the VLA of the National Radio Astronomy Observatory (NRAO) using the A configuration. The observations were carried out in five epochs, ranging from 1995 August 12 to 1999 July 3. The phase center in all the epochs was α(J2000)=05^{h}47^{m}04.784^s, δ(J2000)=00°21′43.103″. The same phase calibrator, 0541$-$056, was used for all the epochs. Flux calibration was achieved by observing 3C286 and 3C48. Data editing and calibration were carried out using the AIPS package of the NRAO, following the standard VLA calibration procedures. Resolved models for the flux calibrators were used. Data from each epoch were self-calibrated in amplitude and phase. A summary of the observation parameters is given in Table 4.1

Additional A configuration data at 20, 6 and 2 cm were taken from the VLA archive (see Table 4.1) and calibrated following standard VLA procedures. Finnally, we also have reanalysed the 1.3 cm continuum data previously reported by Torrelles et al. (1998).

Table 4.1.   Summary of observations

Wavelength	Conf.	Epoch	Observation Date	Flux Calibrator	Phase Calibrator	Bootstrapped Flux Density (Jy)	Synthesized Beam[a] HPBW (arcsec)	P.A. (deg)	rms Noise[a] (μJy beam^{-1})
20 cm	A	1983.9	83-Nov-11	3C48	0530+135	1.90 ± 0.03	1.44 × 1.07	−18	67
6 cm	A	1981.1	81-Feb-08	3C286	0530+135	4.41 ± 0.039	0.71 × 0.50	−39	39
3.6 cm	A	1995.6	95-Aug-12	3C286	0541−056	1.225 ± 0.003	0.34 × 0.25	−15	27
3.6 cm	A	1997.0	97-Jan-10	3C48	0541−056	0.809 ± 0.005	0.31 × 0.25	7	19
3.6 cm	A	1998.2	98-Mar-27	3C48	0541−056	0.720 ± 0.004	0.35 × 0.25	−20	18
3.6 cm	A	1998.4	98-May-26	3C48	0541−056	0.858 ± 0.008	0.36 × 0.24	−26	20
3.6 cm	A	1999.5	99-Jul-03	3C48	0541−056	1.021 ± 0.005	0.34 × 0.27	−12	19
2 cm	A	1987.5	87-Jul-04	3C286	0541−056	1.09 ± 0.01	0.18 × 0.15	−12	55
1.3 cm[b]	A	1996.9	96-Dec-15	3C48	0532+075	2.4 ± 0.1	0.13 × 0.10	−25	200
3 mm[c]	B	2008.0	07-Dec-22	Uranus	0541−056	1.06 ± 0.03	0.52 × 0.48	86	560
3 mm[c]	A	2009.0	09-Jan-30	Uranus	0541−056	0.53 ± 0.02	0.48 × 0.31	-21	300

[a]For naturally weighted maps.

[b]Continuum observations at 1.3 cm were previously reported by Torrelles et al. (1998).

[c]Passband calibration was achieved by observing 0530+135.

4.2.2   CARMA Observations

Continuum data at 3 mm were taken using the CARMA interferometer (Mundy & Scott 2000). We obtained B and A configuration data which provide angular resolutions of ∼0″.5 and ∼0″.3, respectively. Continuum data were recorded in six bands of ∼500 MHz width, covering the frequency ranges 99.75-100.67 GHz and 102.90-103.82 GHz for the lower and upper sidebands, respectively, of the receiver. Each band consists of 15 channels. Flux calibration and bandpass calibration was achieved by observing Uranus and 0530+135, respectively. Data editing and calibration were performed using the MIRIAD package (Sault et al. 1995). A summary of the observational parameters is given in Table 4.1.

4.3   Results and Discussion

In Figure 4.1 we show a superposition of the 3 mm CARMA map (contours) over the 3.6 cm VLA map (colors) of the NGC 2071 region. As can be seen in this figure, we detect the sources IRS 1, IRS 2, and IRS 3 at both wavelengths. Additionally, we have detected at both wavelengths a new radio source, that we call VLA 1 (see figure 4.1), with no known counterparts at other wavelengths. In Table 4.2 we give the flux densities of the sources in the range from 20 cm to 3 mm. In Figure 4.2 we show the SED in the cm-mm range obtained from our data, for sources IRS 1, VLA 1, IRS 2A, and IRS 2B (the SED of IRS 3 will be discussed in section 4.3.2). All the sources show the typical radio spectra found in YSOs consistent in free-free emission at cm wavelengths plus a thermal dust contribution at mm wavelengths.

The brightest sources at radio wavelengths are the sources associated with IRS 1 and IRS 3. These two sources were previously detected at 1.3 cm by Torrelles et al. (1998). These authors found that the 1.3 cm emission from these two sources shows an elongated morphology with their emission dominated by free-free emission, suggesting that both sources trace radio jets. Our results are consistent with those of Torrelles et al. (1998), since these two sources also
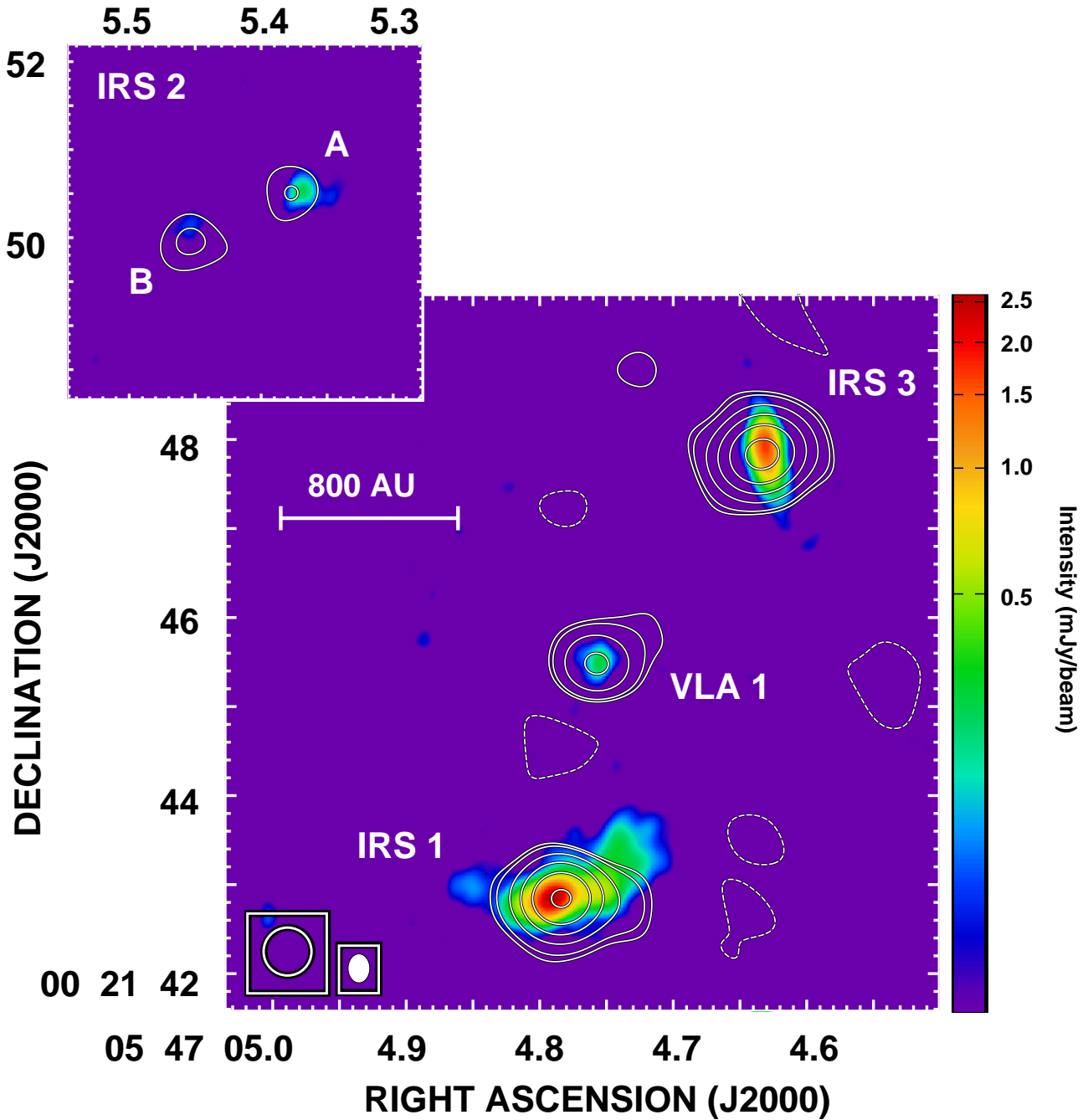
Figure 4.1 Superposition of the CARMA 3 mm continuum emission map (contours) over the VLA 3.6 cm continuum emission map (colors) of the NGC 2071 region. The 3.6 cm map was made by concatenating the uv data from the five epochs. The 3 mm map was made from B Configuration data. Both maps were made using natural weighting. Contours are -3, 3, 4, 8, 16, 32, 64, 128, and 256 times the rms of each map, 19 μJy (3.6 cm) and 600 μJy (3 mm).
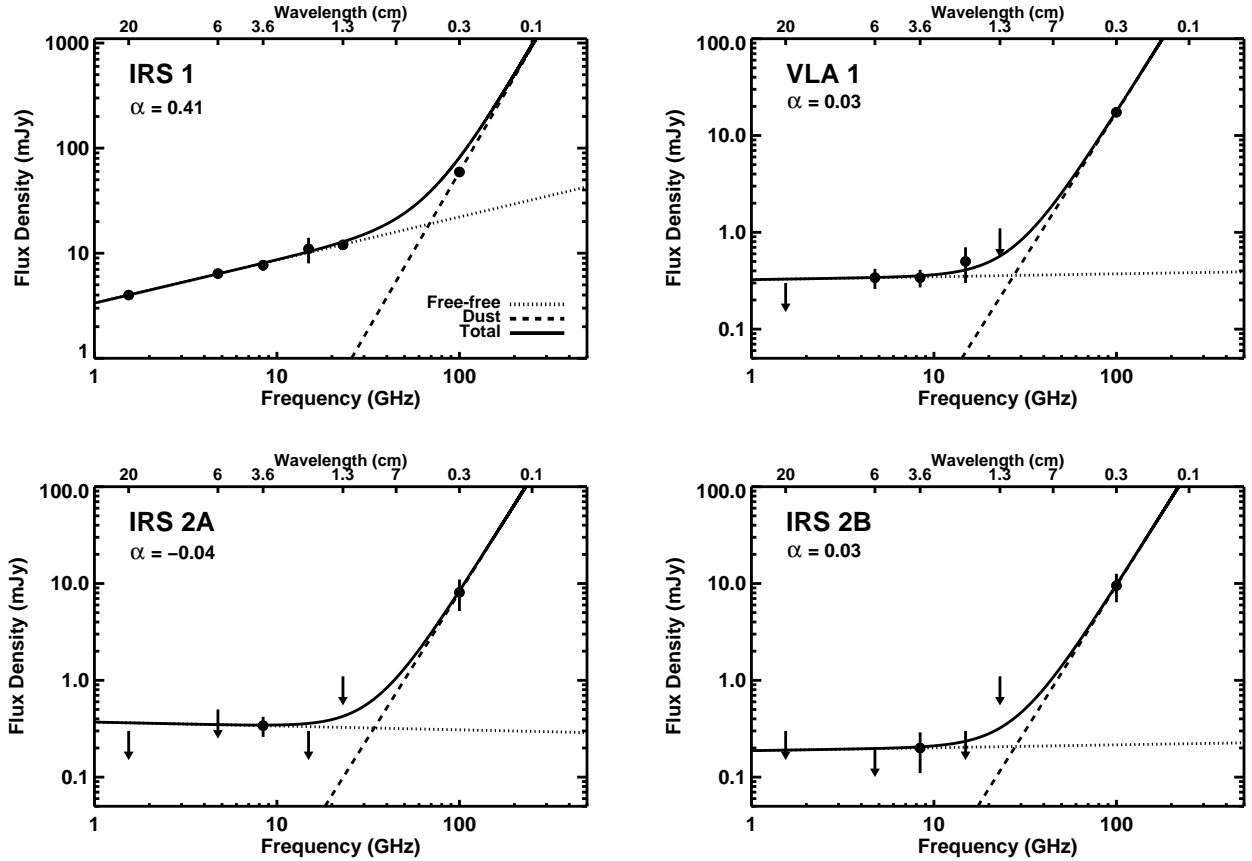
Figure 4.2 Spectral Energy Distributions of sources IRS 1, VLA 1, IRS 2A, and IRS 2B from 20 cm to 3 mm. The data points have been fitted as the sum of two power laws, one of them with a fixed slope of +3 (dust). The slope of the free-free emission (α) is shown in each panel.

shown a jet-like morphology at 3.6 cm (see Figure 4.1). Moreover, the detection of 3 mm emission from both sources, indicates that they are also associated with thermal dust emission, suggesting the presence of circumstellar disks (see figure 4.2). In the following subsections (4.3.1 and 4.3.2), we disscus in more detail the results obtained for these two sources.

IRS 2 was previously detected as a compact source at 6 cm by Snell & Bally (1986). In our higher angular resolution maps, this source is resolved into two weak components (A and B) separated by $1\rlap{.}''3$ ($\sim$500 AU). Both components appear compact and show emission at 3.6 cm and 3 mm. From their flux densities at these two wavelengths (see Table 4.2) we derive steep spectral indices >1.3 for both sources.

Source VLA 1 is detected at 3.6 cm and 3 mm (see Table 4.2). We also detected this source in the VLA data archive at 6 cm and 2 cm (see Table 4.2). The SED of this source also suggests free-free emission at cm wavelengths and thermal dust emission at mm wavelengths. Therefore, this source is most probably another YSOs associated with the region.

4.3.1 IRS 1: A binary jet?

As commented above, the IRS 1 radio source has been proposed to be tracing a radio jet by Torrelles et al. (1998). These authors describe the morphology of IRS 1 as consisting of a main
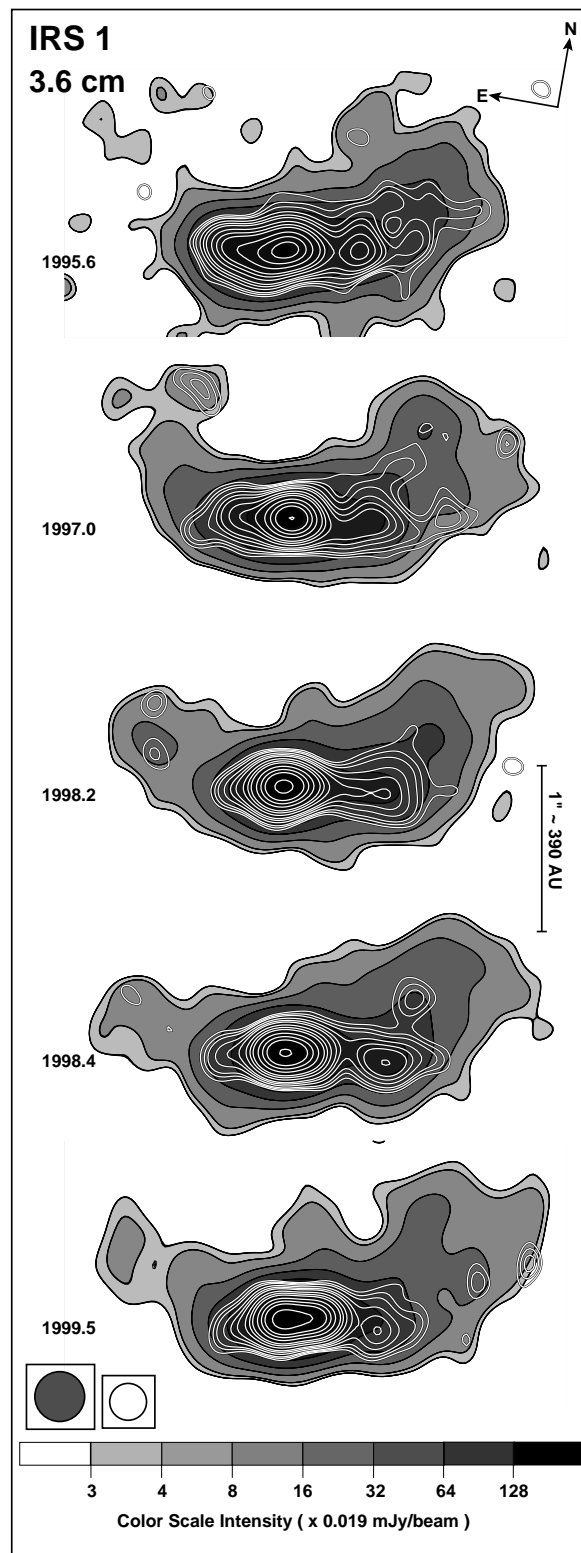
Figure 4.3 VLA 3.6 cm maps of IRS 1 at several epochs. For each epoch, we show the superposition of the uniform weighting map over the natural weighting map. The maps were reconstructed with the same circular beams, $0\rlap{.}''30$ (natural weighting maps) and $0\rlap{.}''22$ (uniform weighting maps). Grey scale ranges from 3 to 128 times the rms of the maps, 19 μJy beam^{-1}. Uniform weighting contours are 4, 5, 6, 7, 8, 10, 12, 14, 16, 18, 20, 25, 30, and 35 times the rms of the maps, 36 μJy/beam.
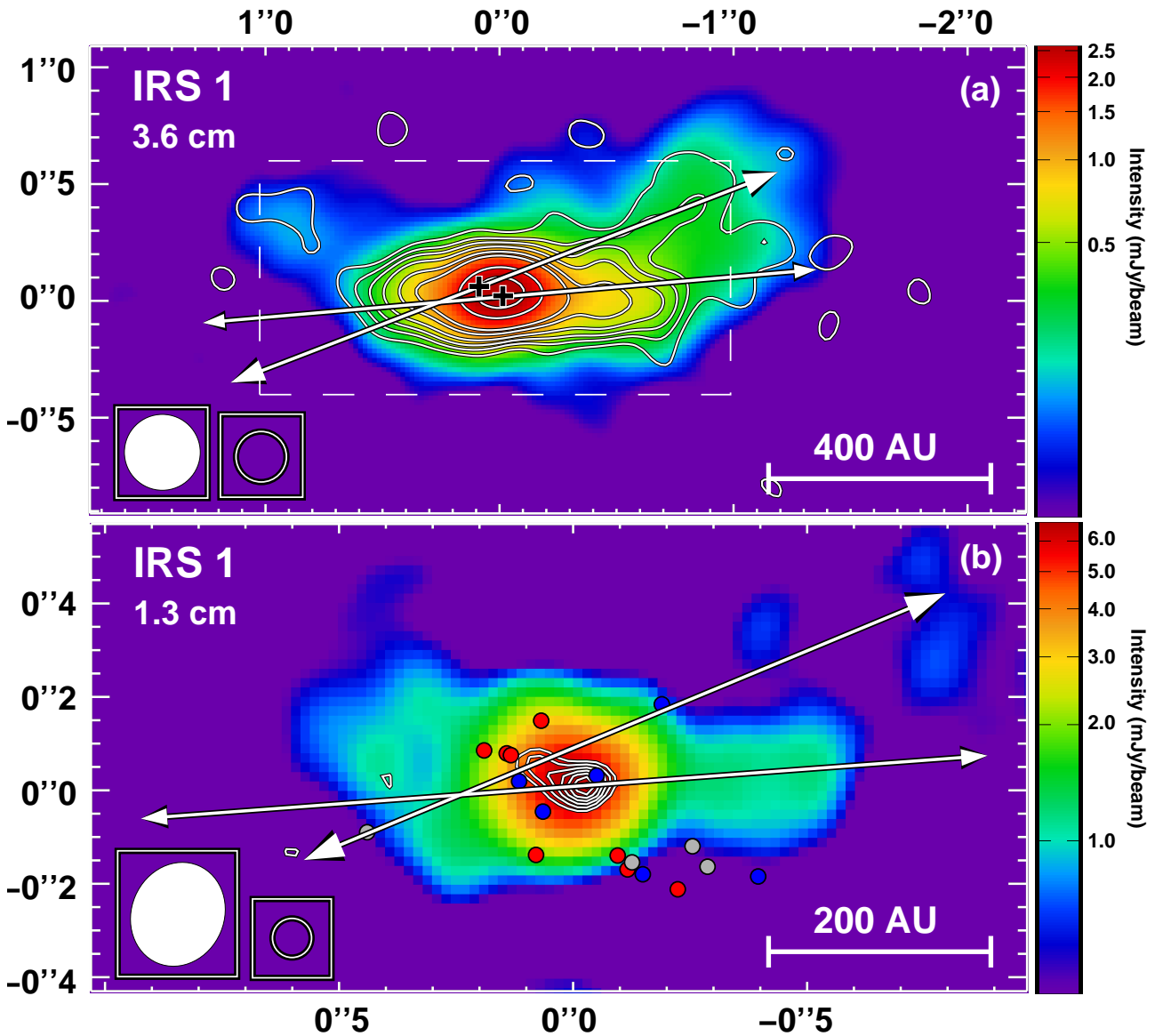
Figure 4.4 VLA maps of IRS 1. **(a)** Superposition of the 3.6 cm uniform weighting map (contours; synthesized beam=$0\farcs22\times0\farcs22$) over the 3.6 cm natural weighting map (colors; synthesized beam=$0\farcs30\times0\farcs30$). These maps were made after concatenation of data from all the epochs. Contours are -3, 3, 5, 7, 10, 15, 20, 40, and 60 times the rms of the map, 30 μJy beam^{-1}. The rms of the natural weighting map is 19 μJy beam^{-1}. Crosses mark the positions of the proposed protobinary system suggested by the 1.3 cm observations shown in panel (b). Solid lines mark a possible orientation of the two jets proposed (see text). **(b)** Superposition of the VLA 1.3 cm uniform weighting map (contours; synthesized beam=$0\farcs09\times0\farcs09$) over the 1.3 cm natural weighting map made with a tapering of 1000 kλ (colors; synthesized beam=0.22×0.20, P.A.=-13°). Contours are 3, 4, 5, 6, 7, 8, and 9 times the rms of the map, 400 μJy. Circles mark the positions of the water maser spots detected by Torrelles et al. (1998). Blue circles have velocities ≤8 km s^{-1}, grey circles have velocities between 8-12 km s^{-1}, and red circles have velocities ≥12 km s^{-1}.

Table 4.2.   Spectral Energy Distributions

Wavelength	Flux Density (mJy)				
	IRS 1	IRS 2A	IRS 2B	IRS 3	VLA 1
20 cm	4.0 ± 0.2	<0.3	<0.3	1.3 ± 0.2	<0.3
6 cm	6.4 ± 0.3	<0.5	<0.2	2.2 ± 0.2	0.34 ± 0.08
3.6 cm[a]	7.7 ± 0.9	0.34 ± 0.08	0.20 ± 0.09	2.9 ± 0.2	0.34 ± 0.07
2 cm	11.0 ± 3.0	<0.3	<0.3	>2.2	0.5 ± 0.2
1.3 cm	12.0 ± 0.7	<1.1	<1.1	7.6 ± 0.7	<1.1
3 mm[b]	59.3 ± 1.6	8.1 ± 2.9	9.5 ± 3.1	72.1 ± 1.7	17.4 ± 1.8

[a]Flux densities at 3.6 cm: Nominal values are the average of the values obtained from the natural weighting maps of each epoch and the errors are estimated as the dispersion of the flux density over all the epochs.

[b]Flux densities at 3 mm obtained from Gaussian fits to the B Configuration natural weighting map.

body elongated east-west and a weak protuberance of emission arising from the main body with a P.A. of 62°. Additionally, the water maser spots associated with this source, appear spread along a direction with a P.A. of 77°, relatively close to the direction of the elongation of the continuum emission. Therefore, they proposed that both, the continuum emission and the water maser spots are tracing a radio jet.

In Figure 4.3 we show the 3.6 cm VLA maps of IRS 1 obtained in the five epochs. Although the general aspect is similar in the different epochs, there are distinguishable differences from one epoch to another that can be attributed to motions and changes in the ionized flow. However, this conclusion cannot be firmly established since the coverage of the uv-plane was different in different epochs.

In our higher sensitivity 3.6 cm observations of source IRS 1, we detected emission with a quite complex morphology (see Figure 4.4). Globally, the source is elongated in a E-W direction, suggesting that it traces a radio jet in that direction. However, in the natural weighting map, the emission at both the eastern and the western edges of the radio jet bends to the north (see Figure 4.4). In the uniform weighting map, which has higher angular resolution, the emission seems to be divided in two different structures: the core of the emission seems to follow an E-W direction, while there is some emission that traces a sort of filament in a SE-NW direction (see Figure 4.4).

In order to explain this morphology, we speculate with two possibilities. A first possibility is that a single YSO drives a jet oriented in the E-W direction. At a distance of ∼300 AU from the driving source, both lobes of the jet strongly interact with dense material in the ambient medium. These shocks could result in a change of the direction of both lobes of the jet resulting in the complex morphology seen in our VLA maps. Since it is required that both lobes of the jet interact with dense gas, this implies that IRS 1 should be completely surrounded by a high

density structure, being IRS 1 embedded in a sort of cavity. Unfortunately, the presence of such a high density structure could not be tested with the present data. High angular resolution observations with a high density gas tracer such as NH_3 would be necessary in order to detect it.

A second possibility is that the emission from IRS 1 is actually arising from a binary jet, i.e., two jets each of them driven by a different component in a close binary system. To explore this possibility, the binary system would remain unresolved with the angular resolution of the 3.6 cm observations. A way to support this possibility would be to resolve the core of the emission in a double source. In this sense, we have obtained new maps from the 1.3 cm data of Torrelles et al. (1998). In the bottom panel of Figure 4.4 we show (in colors) a map made with a tapering of 1000 kλ, which is more sensitive to weak extended emission than the maps shown in Torrelles et al. (1998). This map shows essentially the same morphology than the map of 3.6 cm (except for a slight change in the size of the source due to opacity effects), but with a slightly higher angular resolution. In the same figure, we show, superimposed in contours, a 1.3 cm map made with uniform weighting, which has the highest angular resolution reachable with the data (we used uniform weighting, while the map shown in Torrelles et al. 1998 has been obtained with ROBUST=0). As can be seen in the figure, this uniform weighting map shows emission from a compact source with an elongation to the NE. This elongation could be interpreted as due to emission from a second component, resulting in a binary system with a separation of $\sim 0\rlap{.}''11$ (~ 40 AU) that is marginally resolved by the $0\rlap{.}''09$ beam of the map. These results would support the possibility of a binary jet in the IRS 1 source. However, this should be confirmed with observations with higher angular resolution and sensitivity.

4.3.2   IRS 3: A disk/jet system

Source IRS 3 was previously detected as a 1.3 cm continuum source by Torrelles et al. (1998). In their maps, IRS 3 shows a clear jet-like morphology. These authors also detected a group of water maser spots associated with IRS 3. The maser spots are distributed in a strip of $0\rlap{.}''1$ size (~ 40 AU) centered at the continuum source, almost perpendicular to its major axis (Torrelles et al. 1998). In addition, the LSR velocity of the masers presents a clear gradient along their major axis. From these results, Torrelles et al. (1998) proposed that while the 1.3 cm continuum emission from IRS 3 is tracing a radio jet, the water maser spots are tracing a circumstellar disk with a radius of ~ 20 AU which is seen almost edge-on.

In Figure 4.5 we show the 3.6 cm VLA maps of IRS 3 obtained in the five epochs. There are small differences in the elongation of the source from one epoch to another, that can be attributed to the ejection of new condensations. However, this conclusion cannot be firmly established, since the coverage of the uv-plane was different in different epochs.

In Figure 4.6a we show our 3.6 cm map of IRS 3 made after concatenation of data from all the epochs (natural weighting), as well as the 1.3 cm map (Figure 4.6b) of Torrelles et al. (1998). As can be seen in the figure, the emission at both wavelengths seems to be tracing a radio jet.
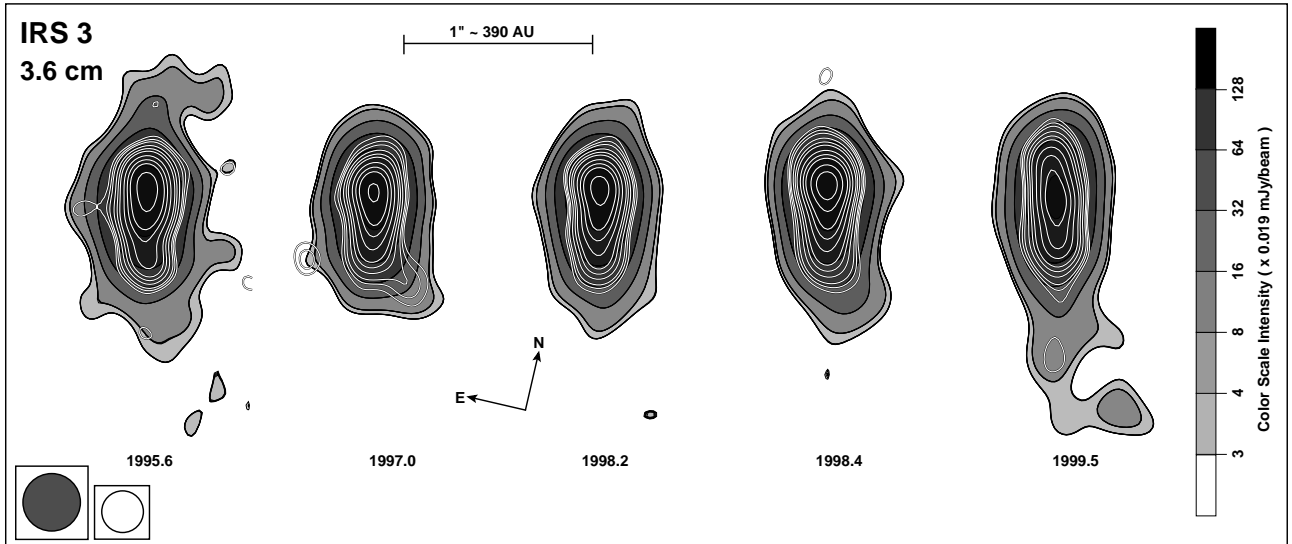
Figure 4.5 VLA 3.6 cm maps of IRS 3 at several epochs. For each epoch, we show the superposition of the uniform weighting map over the natural weighting map. The maps were reconstructed with the same circular beams, $0''\!.30$ (natural weighting maps) and $0''\!.22$ (uniform weighting maps). Grey scale ranges from 3 to 128 times the rms of the maps, 19 μJy beam^{-1}. Uniform weighting contours are 4, 5, 6, 7, 8, 10, 12, 14, 16, 18, 20, 25, 30, and 35 times the rms of the maps, 36 μJy/beam.

In Figure 4.6a, we have superimposed the 3 mm contour map obtained from our CARMA A-configuration observations. As can be seen in the figure, the 3 mm source appears elongated, nearly perpendicular to the jet traced by the centimeter emission. From a Gaussian fit to the 3 mm source, we obtain a deconvolved size of $0''\!.316\times0''\!.136 \pm 0''\!.009$ ($\sim$120$\times$50 AU), and a P.A. of $127° \pm 2°$, which is the same P.A. obtained by Torrelles et al. (1998) from the water maser spots. This strongly suggests that the 3 mm emission is tracing, at larger scales, the same structure than the water maser spots, i.e., a circumstellar disk.

In Figure 4.7 we show the SED of IRS 3 in the range from 20 cm to 1 mm. From a fit to the data in the range from 20 cm to 1.3 cm (dashed line in Fig. 4.7) we obtain a spectral index of $\alpha = 0.6 \pm 0.1$, which is typical of radiojets expanding with constant velocity and constant opening angle (Reynolds 1986). As can be seen in this figure, the extrapolation of the free-free emission (dashed line) cannot account for the flux density detected at 3 mm (34.9 ± 0.8 mJy). Instead, it is possible to account for the 3 mm flux density if a significant contribution ($\sim$60%-90%) of thermal dust emission from a protoplanetary disk is also present at this wavelength.

In order to see if the emission at 3 mm might correspond to that arising from a circumstellar accretion disk, we calculated the emission at this wavelength using physically self-consistent α disk models (D'Alessio et al. 1998, 1999, 2001, 2006). We assumed that contamination from a possible envelope is negligible at 3 mm since there is no evidence of an extended structure in the 3 mm image.

The disk model assumes the α prescription for the viscosity (Shakura & Sunyaev 1973) and solves the disk structure for a given mass accretion rate, stellar central mass and viscosity parameter. The model also assumes a bimodal dust-grain distribution, where it is possible to
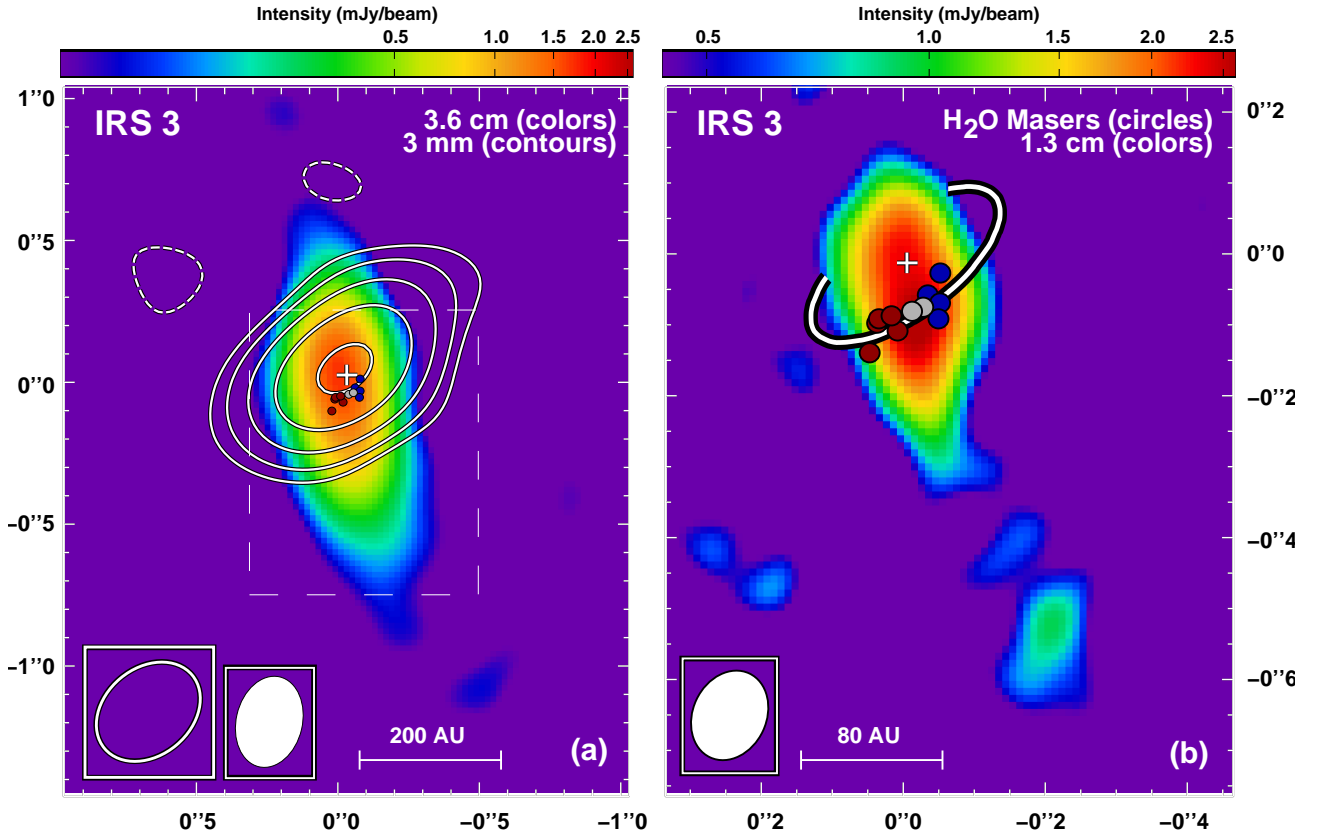
Figure 4.6 **(a)** Superposition of the 3 mm CARMA A-configuration uniform weighting map (contours; synthesized beam=$0\rlap{.}''41 \times 0\rlap{.}''30$, P.A.=$-49°$) over the 3.6 cm VLA natural weighting map (colors; synthesized beam=$0.30''$). The VLA map was made after concatenation of data from all the observed epochs. Contours are -3, 3, 6, 12, 24, and 48 times the rms of the map, 460 μJy beam^{-1}. The rms of the VLA map is 19 μJy beam^{-1}. **(b)** VLA 1.3 cm map of IRS 3 (Torrelles et al. 1998). In both panels, the cross marks the position of the center of the disk derived from a Gaussian fit. The ellipse in the right pannel represents the deconvolved size of the 3 mm source (see Table 4.1). Water masers spots detected by Torrelles et al. (1998) are marked with red (V$_{LSR}$ > 11.8 km $^{-1}$), grey (7.8 km s^{-1} < V$_{LSR}$ < 11.8 km s^{-1}) and blue (V$_{LSR}$ < 7.8 km $^{-1}$) circles.

have grains grow up to mm-size in the disk equatorial plane and a dust distribution with small grains in the disk upper atmosphere. In this way, it is possible to have settling of the dust grains in the equatorial plane which provides a realistic picture of the disk. Once the disk structure is obtained, the monochromatic radiative transfer equation is integrated through the disk and the flux density is calculated.

We adopted a standard value for the viscosity $\alpha = 0.01$. The inclination angle (angle between the polar axis and the line of sight) was derived from the axes ratio in the 3 mm map, resulting in an angle of 60°. Then, we explored different combinations of the mass accretion rate, $\dot{M}$, radius of the disk, R$_d$, and the mass of the central star M$_*$. We tested central stars in the range from 1 to 6 M$_\odot$, accretion rates in the range 10^{-8} - 10^{-6} M$\odot$ yr^{-1}. The stellar effective temperatures and radii are taken from evolutionary tracks of Siess et al. (2000). We considered as valid those sets of parameters that simultaneously fit the observed flux densities and the spatial intensity profile of the 3 mm emission (see Table 4.3).
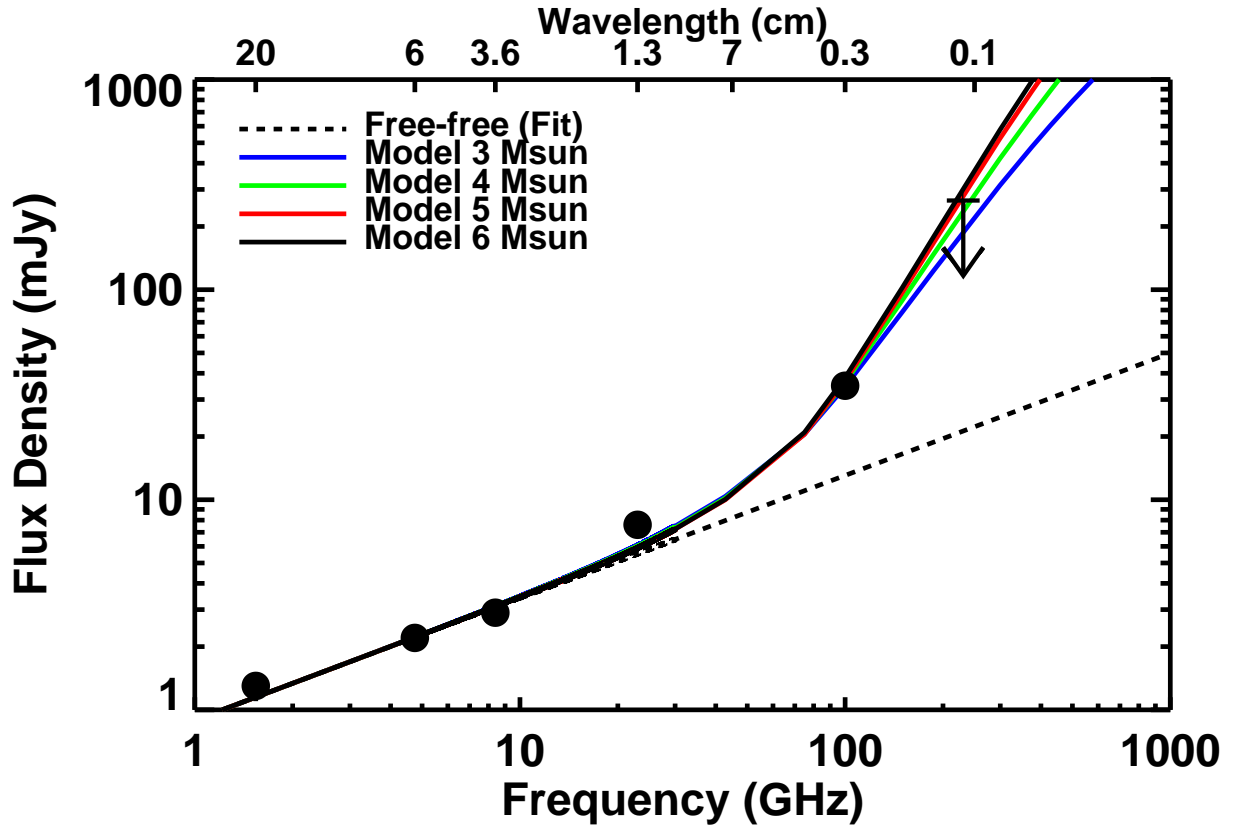
Figure 4.7 Spectral energy distribution of IRS 3. Black circles are the total flux density observed at each wavelength. Dashed line is a least squares fit to the centimeter data. Solid lines are the sums of the free-free and thermal dust emission obtained from the disk models (see Table 4.3).

We found that central stars with masses greater than 6 $M_\odot$ can explain the spatial intensity profile, but predict emission in excess at 1 mm wavelength. Additionally, for any mass accretion rate, stars with masses smaller than 3 $M_\odot$ are unable to reproduce the high emission observed at 3 mm. Thus, although we do not have enough observational constraints, we found that only disks with a mass in the range of 0.2-1.1 $M_\odot$, and an accretion rate in the range 2-4×10^{-7} $M_\odot$ yr^{-1} are able to explain the integrated flux density and spatial intensity profile at 3 mm. Our modeling also constrained the mass of the central star in the range 3-6 $M_\odot$.

The mass of the central star obtained from the modeling is higher than that obtained from the water maser emission by Torrelles et al. (1998). As commented above, these authors inferred a radius of 20 AU for the disk and a central star with a mass of ~1 $M_\odot$. However, in their calculations of the binding stellar mass from the velocity gradient, Torrelles et al. (1998) assumed that the water maser spots were tracing the full extent of an edge-on disk. However, our data suggest that the disk is seen with a inclination angle of 60°, and extends in a larger region that the water maser spots. Under this interpretation the masers would only partially trace the disk, and the mass derived by Torrelles et al. (1998) should be taken as a lower limit.

In Figure 4.6b, we also show an ellipse with the same inclination angle as the disk inferred from our 3 mm observations. This ellipse would represent an orbit with a radius of 60 AU. As can be seen in this figure, all the water maser spots seem to be placed in such a orbit, but they
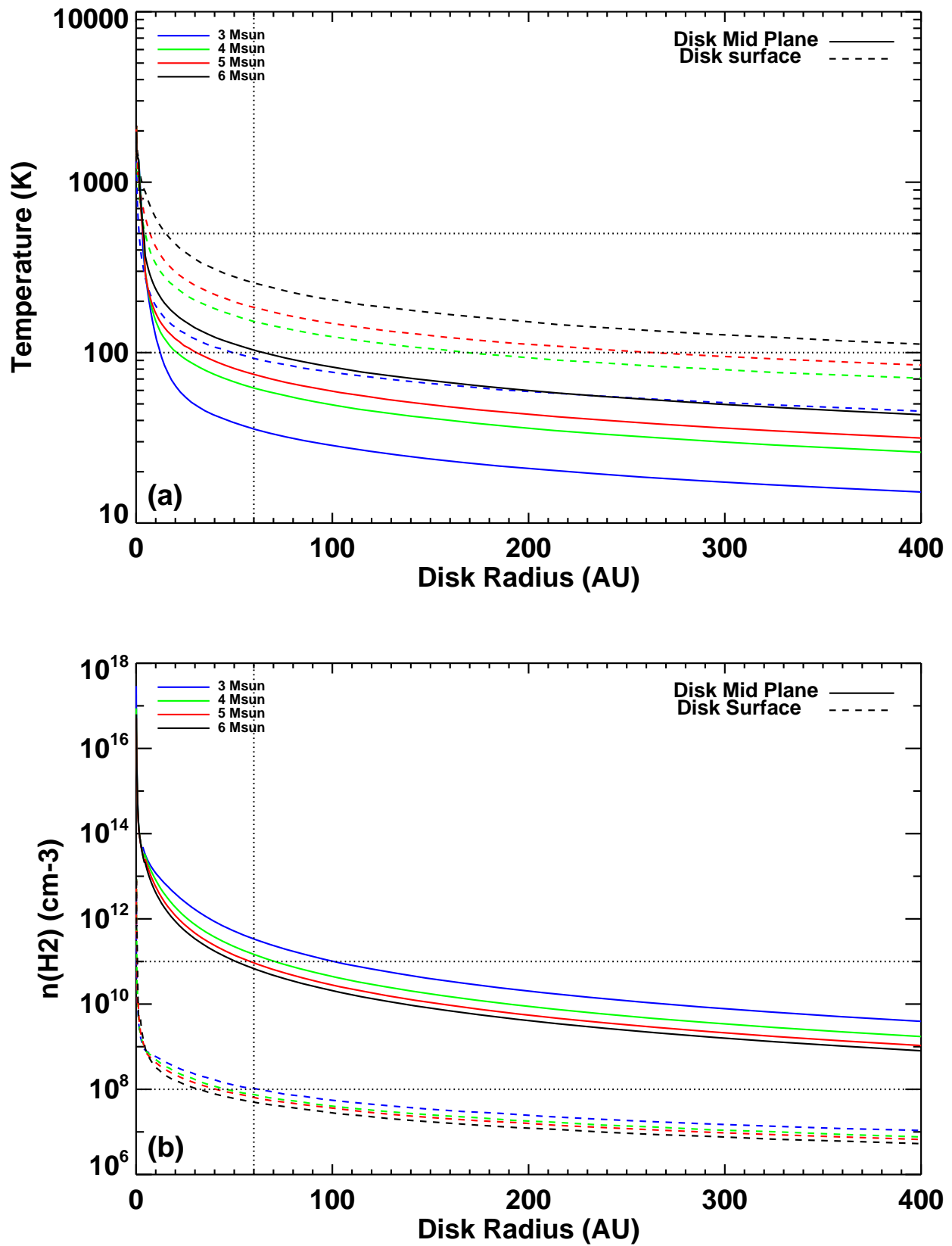
Figure 4.8 Temperature (a) and density (b) profiles, obtained for different models of the IRS 3 disk. Horizontal dotted lines mark the rought limit conditions for water maser emission. The vertical dotted line marks an orbit at radius 60 AU, the proposed distance where the water maser emission detected by Torrelles et al. (1998) originates (see section 4.3.2).

Table 4.3. Parameters of the valid disk models

Stellar Mass ($M_\odot$)	Disk Mass ($M_\odot$)	Accretion Rate ($M_\odot$ yr^{-1})	Disk Radius (AU)	Flux density at 3 mm (mJy)
3	1.1	4.0×10^{-7}	175	24
4	0.46	3.0×10^{-7}	150	26
5	0.75	2.0×10^{-7}	175	27
6	0.248	2.0×10^{-7}	150	28

only partially cover it. This suggests that all the water maser spots detected by Torrelles et al. (1998) are physically located in an orbit of ∼60 AU from the central star. In Figure 4.8, we show the density and temperature profiles obtained for each disk model. We also show in this figure (horizontal dotted lines) rough limit conditions for water maser emission (Elitzur et al. 1989). As can be seen in the figure, all the models have proper density conditions at a radius of 60 AU. However, the model with a central stellar mass of 3 $M_\odot$ has not enough temperature at this radius to produce water masers. Therefore, if our interpretation of the water maser emission is valid, this would impose an additional constraint to the disk models, resulting in a range of possible values for the mass of the central star of 4-6 $M_\odot$, which is significantly higher than the value obtained by Torrelles et al. (1998).

4.4 Conclusions

We observed the intermediate-mass star-forming region NGC 2071 with the VLA and CARMA. We detected 3.6 cm and 3 mm emission from IRS 1, IRS 2, and IRS 3. We also detected a new radio continuum source that we called VLA 1. Our main conclusions can be summarized as follows:

- We have resolved IRS 2 in two components, suggesting that this source is actually a binary system.

- All the sources show a SED consisting of free-free thermal emission at cm wavelengths and thermal dust emission at 3 mm.

- Source IRS 1 shows a complex morphology at 3.6 cm. We speculate that the morphology of this source could be consequence of strong interactions of the jet with the ambient medium, or that we are detecting emission from a binary jet. Higher angular resolution maps of the core of the emission in this source suggests the presence of a binary system, supporting the hypothesis of a binary jet as the origin of the morphology of IRS 1.

- The 3.6 cm emission of IRS 3 shows a clear jet-like morphology, while at 3 mm, the morphology seems to be tracing thermal dust emission from a resolved circumstellar disk. We have modeled the SED and spatial intensity profile of the 3 mm emission as an

accretion disk. This has allowed us to constrain the mass of the central star in the range 3-6 $M_{\odot}$, the accretion rate in the range 2-4$\times 10^{-7}$ $M_{\odot}$ yr^{-1}, and the radius of the disk in the range 150-175 AU.

- Our results suggest that the water maser spots previously detected in IRS 3 are arising from a region located in an orbit of 60 AU in the disk.

Bibliography

Anthony-Twarog, B. J. 1982, AJ, 87, 1213

Bally, J. 1982, ApJ, 261, 558

Butner, H. M., Evans, N. J., II, Harvey, P. M., Mundy, L. G., Natta, A., & Randich, M. S. 1990, ApJ, 364, 164

Chernin, L. M., & Masson, C. R. 1992, ApJL, 396, L35

Chernin, L. M., & Welch, W. J. 1995, ApJL, 440, L21

D'Alessio, P., Cantó, J., Calvet, N., Lizano, S. 1998, ApJ, 500, 411

D'Alessio, P., Calvet, N., Hartmann, L., Lizano, S., Cantó, J. 1999, ApJ, 527, 893

D'Alessio, P., Calvet, N., Hartmann, L. 2001, ApJ, 553, 321

D'Alessio, P., Calvet, N., Hartmann, L., Franco-Hernández, R., Servín, H. 2006, ApJ, 638, 314

Elitzur, M., Hollenbach, D.J., & McKee, C.F. 1989, ApJ, 346, 983

Eislöffel, J. 2000, A&A, 354, 236

Houde, M., Phillips, T. G., Bastien, P., Peng, R., & Yoshida, H. 2001, ApJ, 547, 311

Kitamura, Y., Kawabe, R., Yamashita, T., & Hayashi, M. 1990, ApJ, 363, 180

Margulis, M., & Snell, R. L. 1989, ApJ, 343, 779

Moriarty-Schieven, G. H., Hughes, V. A., & Snell, R. L. 1989, ApJ, 347, 358

Mundy, L. G., Scott, S. L. 2000, ASPC, 217, 235M

Persson, S. E., Geballe, T. R., Simon, T., Lonsdale, C. J., & Baas, F. 1981, ApJL, 251, L85

Sault, R. J., Teuben, P. J., Wright, M. C. H. 1995, ASPC, 77, 433

Scoville, N. Z., Sargent, A. I., Sanders, D. B., Claussen, M. J., Masson, C. R., Lo, K. Y., & Phillips, T. G. 1986, ApJ, 303, 416

Shakura & Sunyaev 1973, A&A, 24, 337

Siess, L., Dufour, E., Forestini, M. 2000, A&A, 358, 593

Smith, H. A., & Beck, S. C. 1994, ApJ, 420, 643

Snell, R. L., & Bally, J. 1986, ApJ, 303, 683

Snell, R. L., Scoville, N. Z., Sanders, D. B., & Erickson, N. R. 1984, ApJ, 284, 176

Stojimirović, I., Snell, R. L., & Narayanan, G. 2008, ApJ, 679, 557

Torrelles, J. M., Gómez, J. F., Rodríguez, L. F., Curiel, S., Anglada, G., & Ho, P. T. P. 1998, ApJ, 505, 756

5

The Nature of the Sources in the W 75 N massive star-forming region*

In this chapter we analyze radio continuum and line observations from the VLA archive of the region of massive star formation W75N. Five radio continuum sources are detected: VLA 1, VLA 2, VLA 3, Bc, and VLA 4. VLA 3 appears to be a radio jet; we detect J=1-0, v=0 SiO emission towards it, probably tracing the inner parts of a molecular outflow. The radio continuum source Bc, previously believed to be tracing an independent star, is found to exhibit important changes in total flux density, morphology, and position. These results suggest that source Bc is actually a radio Herbig-Haro object, one of the brightest known, powered by the VLA 3 jet source. VLA 4 is a new radio continuum component, located a few arcsec to the south of the group of previously known radio sources. Strong and broad (1,1) and (2,2) ammonia emission is detected from the region containing the radio sources VLA 1, VLA 2, and VLA 3.

5.1 Introduction

The massive star-forming region W75N is part of the Cygnus X complex of dense molecular clouds. Its distance is estimated to be 2 kpc (Fischer et al. 1985). Haschick et al. (1981) detected at 6 cm a source that was interpreted as an ultracompact HII (UC HII) region named W75N(B), that later was resolved into three small diameter radio continuum sources: Ba, Bb and Bc in the high angular resolution (0.′′5) observations of Hunter et al. (1994). Two of these sources, Ba and Bb, were also detected at 1.3 cm (with a 0.′′1 resolution) by Torrelles et al. (1997) (who named them as VLA 1 and VLA 3) along with another fainter and more compact source, located in between VLA 1 and VLA 3, and named as VLA 2. These compact sources were believed to be UC HII regions in an early phase, based on the presence of H2O and/or OH masers (Baart et al. 1986, Hunter et al. 1994, Torrelles et al. 1997) in its close vicinity.

At radio wavelengths, VLA 1 has a structure elongated at a PA of ∼43° (Torrelles et al.

1997), approximately in the direction of the observed high-velocity three pc-scale bipolar outflow (Hunter et al. 1994; Shepherd et al. 2003). However, Shepherd (2001) had pointed that VLA 1 does not appear to contribute significantly to the energetics of the large-scale outflow. VLA 2 shows a symmetric roundish shape. A detailed Very Long Baseline Interferometry (VLBI) study of the water maser cluster morphology and kinematics in the vicinity of these two radio sources by Torrelles et al. (2003) showed remarkably different outflow ejection geometries among them (VLA 1 has a collimated, jetlike outflow, while VLA 2 has a shell outflow expanding in multiple directions). This is a surprising result given that both objects are separated by only 1400 AU and share the same environment. VLA 3 was found to have deconvolved dimensions of $0\rlap{.}''9 \times 0\rlap{.}''4$ (PA = 152°) at 1.3 cm by Torrelles et al. (1997). This source is also detected at mid-infrared wavelengths, with a bolometric luminosity of 750 L$_\odot$ (Persi, Tapia, & Smith 2006). The physical parameters of the ionized gas in VLA 1, VLA 2, VLA 3, and Bc, as well as the more evolved W75N(A) are all consistent with each being powered by a ZAMS star of spectral type between B0 and B2 (Shepherd et al. 2004). The present evidence is consistent with an independent exciting source of this spectral type for each radio continuum component, but the results presented in this chapter suggest a likely alternative interpretation.

5.2   Observations

5.2.1   Continuum Observations

Continuum observations at 3.6 cm and 2 cm were taken from the archive of the VLA. The 3.6 cm observations were carried out in three epochs using the A configuration. The 2 cm observations were carried out in one epoch using the B configuration. Data editing and calibration were carried out using the Astronomical Image Processing System (AIPS) package of NRAO, following the standard VLA procedures. The observation dates, the flux and phase calibrator, the bootstrapped flux densities of the phase calibrator, as well as the parameters of the synthesized beams, and the rms noise of the naturally weighted maps are given in Table 5.1.

5.2.2   NH$_3$ Observations

We analysed VLA archival observations of the (1,1) and (2,2) inversion transitions of ammonia, at 23.694495 and 23.722633 GHz, respectively. The spectral line observations were made with two IFs, one centered on the (1,1) transition and the other on the (2,2) transition. The number of channels in each IF was 63, for a velocity resolution of 0.6 km s^{-1} and a velocity coverage of $\sim$35 km s^{-1}. Since these observations did not include an ad hoc bandpass calibrator, we were forced to use as bandpass calibrators the flux (1331+305) and phase (2007+404) calibrators. We made natural- and uniform-weight images of the NH3 emission. The natural-weight images emphasize the large scale extended emission of the region, while the uniform-weight images emphasize bright and compact emission. We also made maps of the rotational temperature of the gas, estimated from the (2,2)/(1,1) ratio following Ho & Townes (1983), assuming constant

Table 5.1. Parameters of the VLA continuum observations

Observation Date	Conf.	Frequency (GHz)	Flux Calibrator	Phase Calibrator	Bootstrapped Flux Density (Jy)	Synthesized Beam[a]		rms of the map[a] (mJy/beam)
						HPBW	P.A.	
1992 Nov 24 (1992.90)	A	8.44	0137+331	2007+404	3.18±0.07	$0\rlap{.}''23\times0\rlap{.}''19$	-56°	0.09
1998 Mar 26 (1998.23)	A	8.46	1331+305	2025+337	4.73±0.08	$0\rlap{.}''24\times0\rlap{.}''20$	48°	0.13
2001 Apr 23 (2001.31)	B	14.9	1331+305	2015+371	2.21±0.01	$0\rlap{.}''47\times0\rlap{.}''39$	-83°	0.08
2006 May 18 (2006.38)	A	8.46	1331+305	2007+404	2.30±0.01	$0\rlap{.}''22\times0\rlap{.}''17$	18°	0.05

[a]For naturally weighted maps.

excitation conditions along the line of sight and optically thin emission.

5.2.3 SiO Observations

We also analysed VLA archival observations of the J = 1→0; v = 0 emission of the SiO molecule (43.423858 GHz). The spectral line observations were made with one IF and a total number of 63 channels, for a velocity resolution of 1.2 km s^{-1} and a velocity coverage of ∼80 km s^{-1}. Since these observations did not include an ad hoc bandpass calibrator, we were forced to use as bandpass calibrators the flux (1331+305) and phase (2012+464) calibrators.

5.3 Results

5.3.1 Continuum emission

In Figure 5.1 we show the continuum images of the central region of the W75N star-forming region at 3.6 cm (2006.38) and 2 cm (2001.31). As can be seen in this figure, to the south of the previously known components (VLA 1, VLA 2, VLA 3 and Bc), we detected a new radio source, VLA 4. This source was not detected in the other continuum images discussed here (see below), most probably because they are noiser than the 2006 image at 3.6 cm. In Table 5.2 we show the positions of the five sources (from the 3.6 cm 2006 data) with their flux densities at both wavelengths (3.6 and 2 cm) and their spectral indices in this wavelength range. We note that since some of the sources are time-variable (see below), these spectral indices are not very reliable.

Three of the sources (VLA 1, Bc, and VLA 4) have flat spectral indices within the error, a result consistent with optically thin free-free emission. Source VLA 3 has a spectral index of 0.6±0.1, consistent with the value expected for a thermal jet. The source with the steepest spectral index is VLA 2, that with a value of 2.2±0.3 suggests optically thick free-free emission.

In Figure 5.2 we compare the three 3.6 cm images made from data taken in 1992, 1998, and 2006. Since these observations were not made with the same phase calibrator (see Table 5.1), we aligned them by assuming that the position of VLA 3 was the same at all three epochs and using the 2006 position for all of them. This alignment involved small position shifts of $\leq0\rlap{.}''1$. In particular, the shift of the 1998 image to align it with the 2006 image was of only $\Delta\alpha = +0\rlap{.}^{s}007$; $\Delta\beta = -0\rlap{.}''03$. Of the sources in the region, only source Bc shows important changes in position. Its average proper motion, $0\rlap{.}''3 \pm 0\rlap{.}''1$ toward the south, over a time of 13.48 years
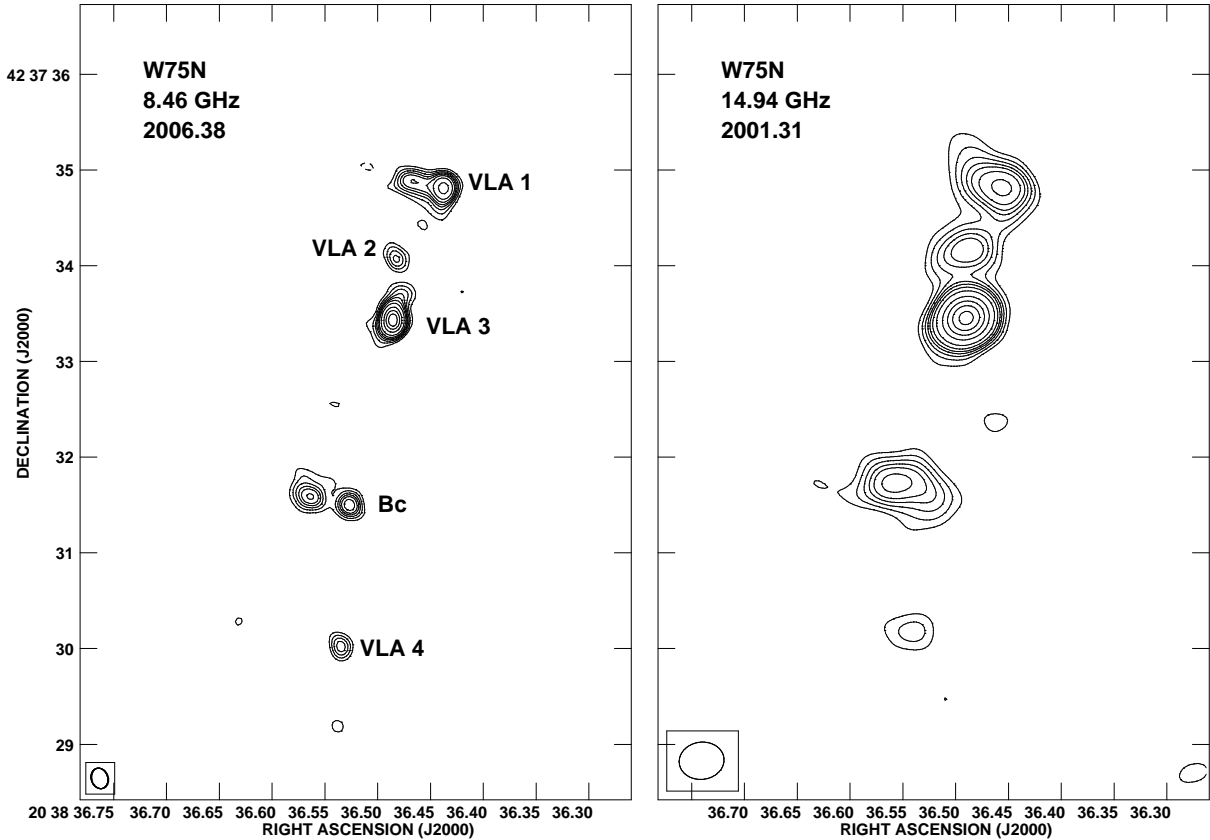
Figure 5.1 VLA contour images of the 3.6 cm (left) and 2 cm (right) emission from the W75N region. The contours are -4, 4, 6, 8, 10, 12, 15, 20, 30, 40, 50, and 60 times 45 and 78 μJy beam^{-1}, the respective rms noises. The half power contours of the synthesized beams are shown in the bottom left corner of each figure and are $0\rlap{.}''22 \times 0\rlap{.}''17; PA = 18°$ for the 3.6 cm image and $0\rlap{.}''47 \times 0\rlap{.}''39; PA = -83°$ for the 2 cm image. Both images were made with ROBUST = 0 (u,v) weighting. The source VLA 4 is a new detection. The epochs of the observations are given in the figure.

at a distance of 2 kpc, implies an average velocity in the plane of the sky of 220±70 km s^{-1}. However, as can be seen in Figure 5.2, most of the displacement took place between the last two epochs, so the velocity between these two last epochs is possibly larger.

In addition to the proper motions, there is a dramatic change in flux density and morphology of source Bc at 3.6 cm. In 1992 it was a weak compact source (with a flux density of 0.9±0.2 mJy), becoming brighter (2.7±0.5 mJy) and elongated in 1998 (see Figure 2). The position does not seem to change significantly between these two epochs. Finally, in 2006 the source remained bright (3.3±0.2 mJy) and appears as broken in two components. Furthermore, it has clearly moved to the south.

5.3.2   SiO Emission

In Figure 5.3, we show a velocity-integrated (moment 0) of the J = 1→0; v = 0 emission of the SiO molecule. The SiO emission is compact and centered on VLA 3, although part of the emission could be coming from VLA 2. The SiO spectrum is shown in the right panel of Figure

Table 5.2. Parameters of the continuum sources

Source	Position (J2000)[a] Right Ascension	Declination	Deconvolved Size[b] $'' \times ''$; $°$	Flux Density (mJy)[c] 3.6 cm	2 cm	Spectral Index[d]
VLA 1	$20^h\ 38^m\ 36\overset{s}{.}445$	$+42°\ 37'\ 34\overset{''}{.}82$	$0.43\pm0.02\times0.17\pm0.02;\ 80\pm2$	3.8 ± 0.1	3.0 ± 0.2	-0.4 ± 0.1
VLA 2	$20^h\ 38^m\ 36\overset{s}{.}482$	$+42°\ 37'\ 34\overset{''}{.}08$	$< 0\overset{''}{.}2$	0.7 ± 0.1	2.4 ± 0.3	2.2 ± 0.3
VLA 3	$20^h\ 38^m\ 36\overset{s}{.}486$	$+42°\ 37'\ 33\overset{''}{.}44$	$0.21\pm0.01\times0.07\pm0.01;\ 157\pm3$	4.0 ± 0.1	5.7 ± 0.2	0.6 ± 0.1
Bc	$20^h\ 38^m\ 36\overset{s}{.}549$	$+42°\ 37'\ 31\overset{''}{.}57$	$0.75\pm0.05\times0.23\pm0.03;\ 74\pm3$	3.3 ± 0.2	3.0 ± 0.3	-0.2 ± 0.2
VLA 4	$20^h\ 38^m\ 36\overset{s}{.}535$	$+42°\ 37'\ 30\overset{''}{.}03$	$< 0\overset{''}{.}2$	0.7 ± 0.1	0.9 ± 0.2	0.4 ± 0.5

[a]Positions obtained from the 3.6 cm 2006 data. Absolute positional error is estimated to be $\sim0\overset{''}{.}07$.

[b]Deconvolved sizes obtained from Gaussian fits to the 3.6 cm 2006 data. The deconvolved dimensions are given as major axis $\times$ minor axis; position angle.

[c]The flux densities were obtained fitting a single Gaussian ellipsoid to all the emission present.

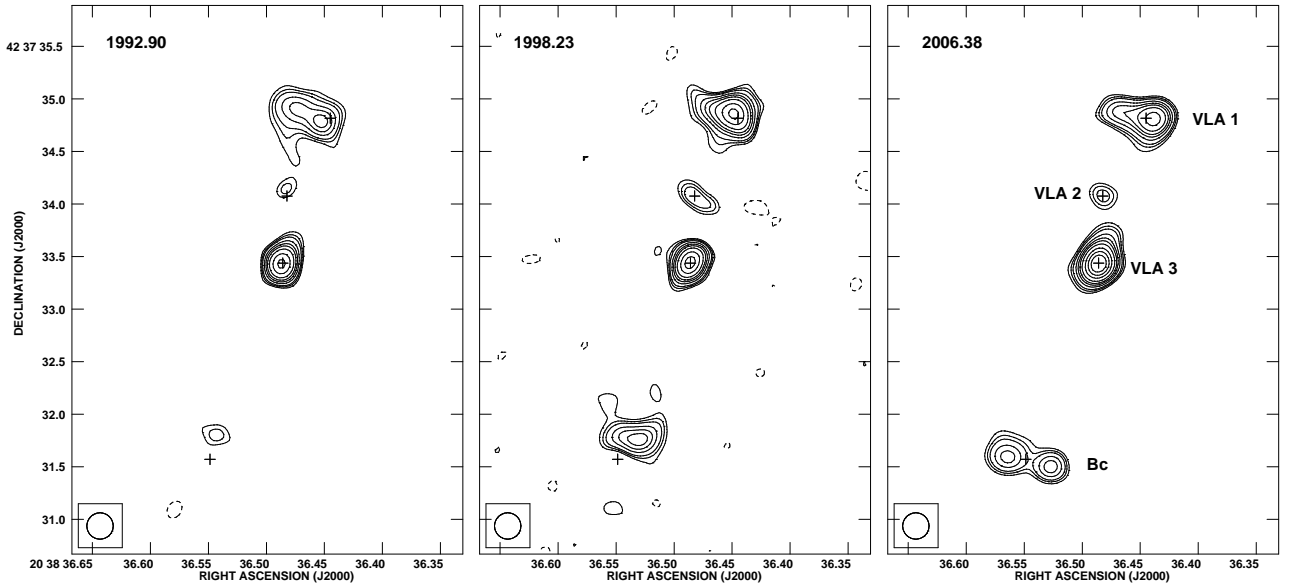[d]Spectral indices in the 3.6 to 2 cm wavelength range.

Figure 5.2 VLA contour images of the 3.6 cm emission for the three epochs (1992.90, 1998.23, and 2006.38) analyzed. Contours are -4, 4, 5, 6, 8, 10, 12, 15, 20, 25, and 30 times 80 μJy beam^{-1}. The images have been restored with a circular beam of $0\overset{''}{.}25$, shown in the bottom left corner of the images. The crosses mark the centroids of the radio sources for epoch 2006.38. The source VLA 4 is detected only in the last epoch and it is not included in these images.

5.3. The observed transition is known to be a tracer of outflows (e.g. Choi 2005). We propose that the SiO emission could be tracing the inner parts of an outflow associated with VLA 3, although observations with much better angular resolution, sensitivity and velocity coverage are needed to test this hypothesis.

5.3.3 NH$_3$ Emission

In Figure 5.4 we show the large scale emission of the ammonia. The main result of this image is that the region of active star formation in W75N appears to be located at the intersection of two molecular filaments, one with emission in the LSR radial velocity range of $\sim$5 to 8 km s^{-1} and the other with emission in the LSR radial velocity range of $\sim$9 to 13 km s^{-1}. In particular,
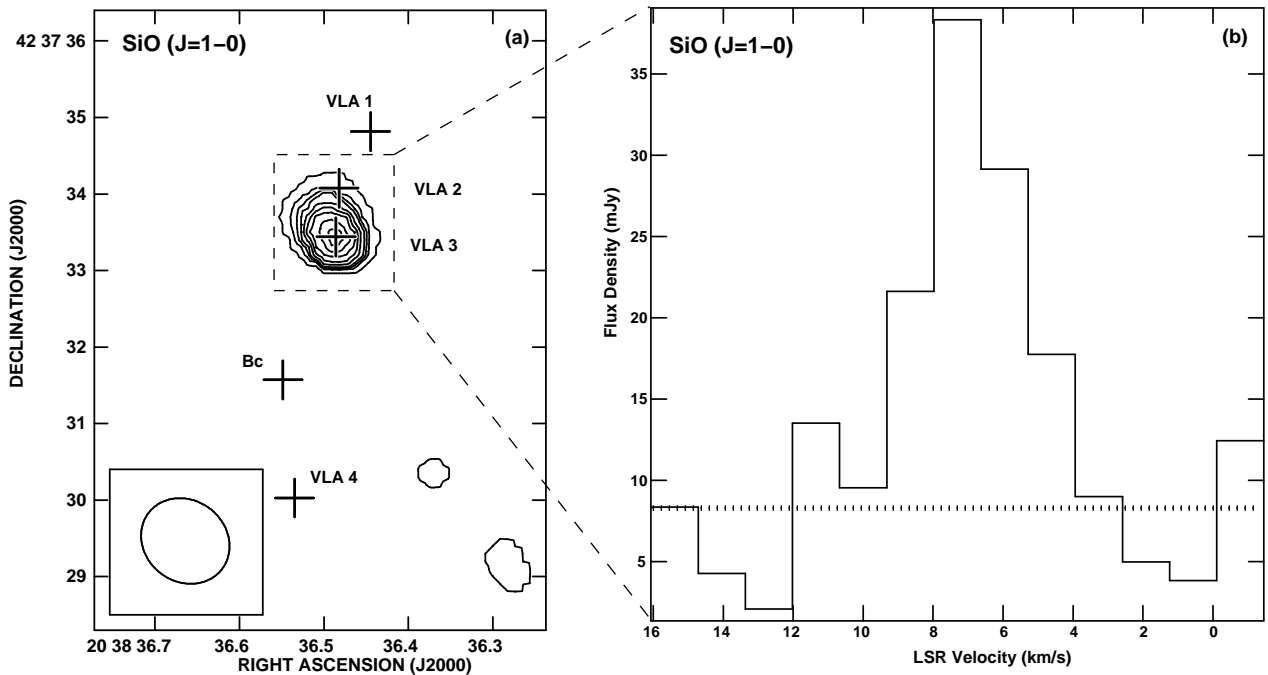
Figure 5.3 **(a)** VLA contour image of the moment 0 of the J= 1–0; v = 0 SiO emission from the W75N region. Contours are 20, 40, 50, 60, 80, 100, 120, 140, and 160 mJy beam^{-1} km s^{-1}. The beam ($1''21 \times 1''06$; PA = 52°) is shown in the bottom left corner of the image. The crosses mark the positions of the radio continuum sources. The dashed rectangle indicates the solid angle over which the spectrum of the right panel of this figure was obtained. **(b)** Spectrum of the SiO emission from the box indicated in the left panel. The dotted horizontal line indicates the expected 7-mm continuum contribution, as estimated from the results of Shepherd et al. (2004).

the five continuum sources are located at the intersection zone, which is also the hottest zone. This suggests that the star formation in W 75N is being triggered by the collision of molecular filaments. This mode of star formation is predicted by numerical simulations (e.g., Ballesteros-Paredes et al. 1999 and Vázquez-Semanedi et al. 2007) and has been also suggested to be present for the regions W3 IRS 5 by Rodón et al. (2008) and W33A by Galván-Madrid et al. (2010).

In Figure 5.5 we investigate in more detail the region of active star formation. In the left panel of this Figure we show in greyscale the velocity-integrated (moment 0) emission of the (2,2) transition as well as the adjacent continuum emission, obtained from the line-free channels, in contours. On the right panel of this Figure we show the (1,1) and (2,2) spectra integrated over the region of emission. From this spectra we conclude that there is strong and broad (FWHM of $\sim$6 km s^{-1}) ammonia emission originating from the region that contains the continuum sources VLA 1, VLA 2, and VLA 3. This emission is most probably tracing dense ($\geq 3 \times 10^4$ cm^{-3}) gas. From the ratio of the inner satellite lines to the main line of the (1,1) transition ($\sim$0.3), we conclude that the emission is optically thin. Following Anglada et al. (1995) and assuming a $[NH3/H2]$ ratio of 10^7, we estimate a mass of $\sim$0.6 M$_\odot$ for the
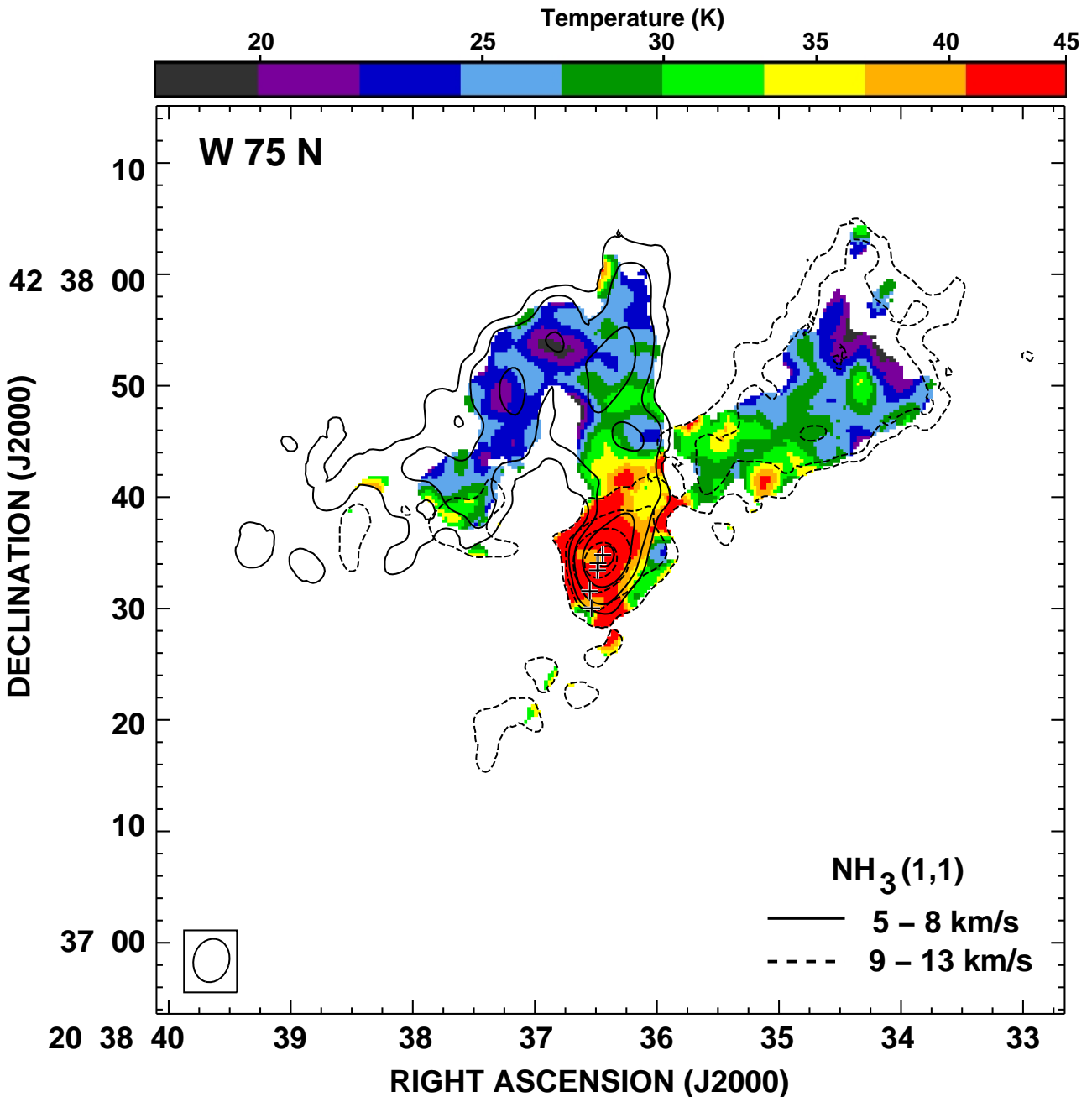
Figure 5.4 Superposition of the natural-weight images of the moment 0 of the $NH_3(1,1)$ emission (contours) over the temperature image (colors). The solid contours trace the emission integrated in the velocity range from 5 to 8 km s^{-1}, while the dashed contours are integrated in the velocity range from 9 to 13 km s^{-1}. Contour levels are 30, 50, 100 and 200 mJy beam^{-1} km s^{-1}. The color scale indicates the rotational temperature, as derived from the $(2,2)/(1,1)$ ratio. The crosses mark the positions of the five continuum sources. The beam $(4\rlap{.}''1 \times 3\rlap{.}''$; PA $= -18°)$ is shown in the bottom left corner of the image.

condensation.

In Figure 5.6 we show, on the left panel, the velocity field (moment 1) from the (2,2) transition. On the center we show the velocity dispersion (moment 2) from the (2,2) transition. For a Gaussian profile the full width at half power equals the dispersion multiplied by 2.35. Finally, on the right panel we show the rotational temperature of the gas. The region with
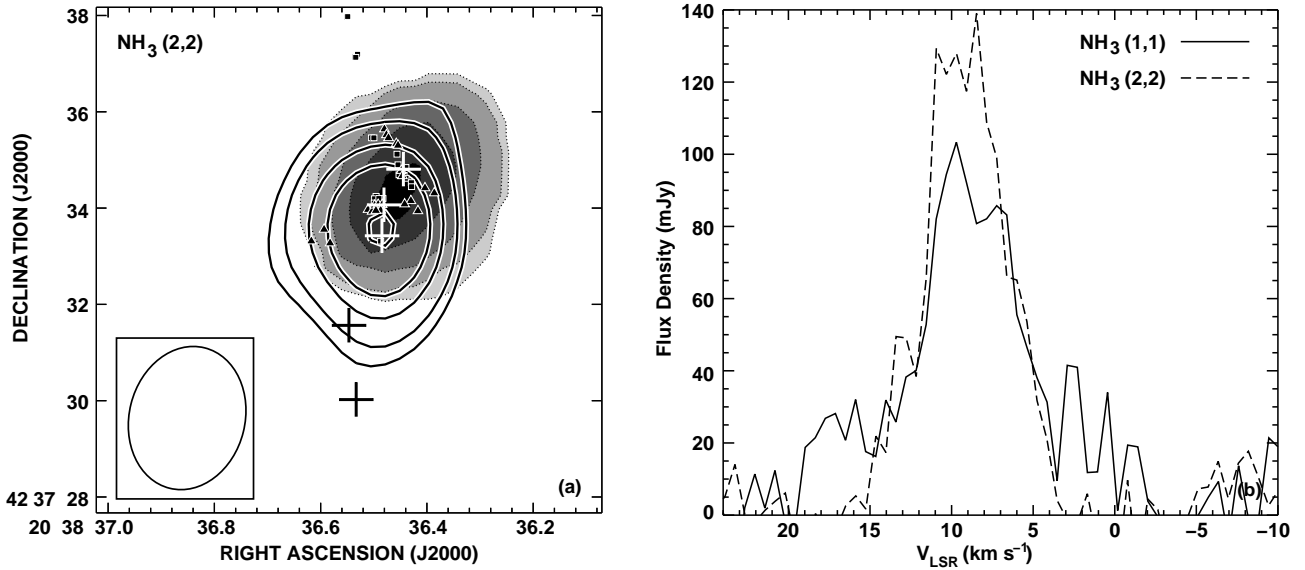
Figure 5.5 **(a)** In greyscale levels we show the velocity-integrated (moment 0) emission from the (2,2) transition of ammonia. Levels are 50, 100, 200, 300, and 400 mJy beam^{-1} km s^{-1}. The thin contours show the 1.3 cm emission continuum from the region (obtained from the line-free channels). Contours are -3, 3, 4, 6, 8, and 12 times 1.7 mJy beam^{-1}, the rms of the continuum image. The five crosses mark the positions of the continuum sources. The squares are the positions of the H_2O masers from Torrelles et al. (1997) and the triangles the OH masers from Hutawarakorn et al. (2002). The beam ($2''97 \times 2''43$; PA $= -13°$) is shown in the bottom left corner. **(b)** Spectra of the (1,1) and (2,2) transitions of ammonia integrated over the region of emission. Lines are broad, and in the (1,1) spectrum the emission of the main line appears blended with that of the inner satellites.

ammonia emission shows a velocity shift of about 2 km s^1 over a region of $\sim3''$. This velocity shift could be arising from different gas components associated with the multiple sources (VLA1, VLA2, VLA3) within the NH3 beam. The central panel of Figure 6 indicates that the broadest emission overlaps the position of the sources VLA 1, 2, and 3. The right panel of Figure 6 indicates that the coolest parts of the ammonia cloud, with temperatures of about 35 K, overlaps the position of VLA 1.

5.4   Discussion

5.4.1   Bc: a radio HH object

As commented in Section 2.1, the source Bc shows changes in its position, flux density and morphology. The source seems to be moving to the south with a velocity larger than 200 km s^{-1} while it breaks into two components and dramatically increases its total flux density. This behavior is similar to that observed in optical (Devine et al. 2009) and radio (Curiel et al. 1993) Herbig-Haro objects, and, therefore, we interpret source Bc as an obscured radio HH object. Its radio luminosity (3.3 mJy in 2006, at a distance of 2 kpc) makes it one of the brightest HH objects detected in the radio. It is comparable to, but significantly above, HH 80 and HH 81 that have centimeter flux densities of 1-2 mJy at a distance of 1.7 kpc (Martí
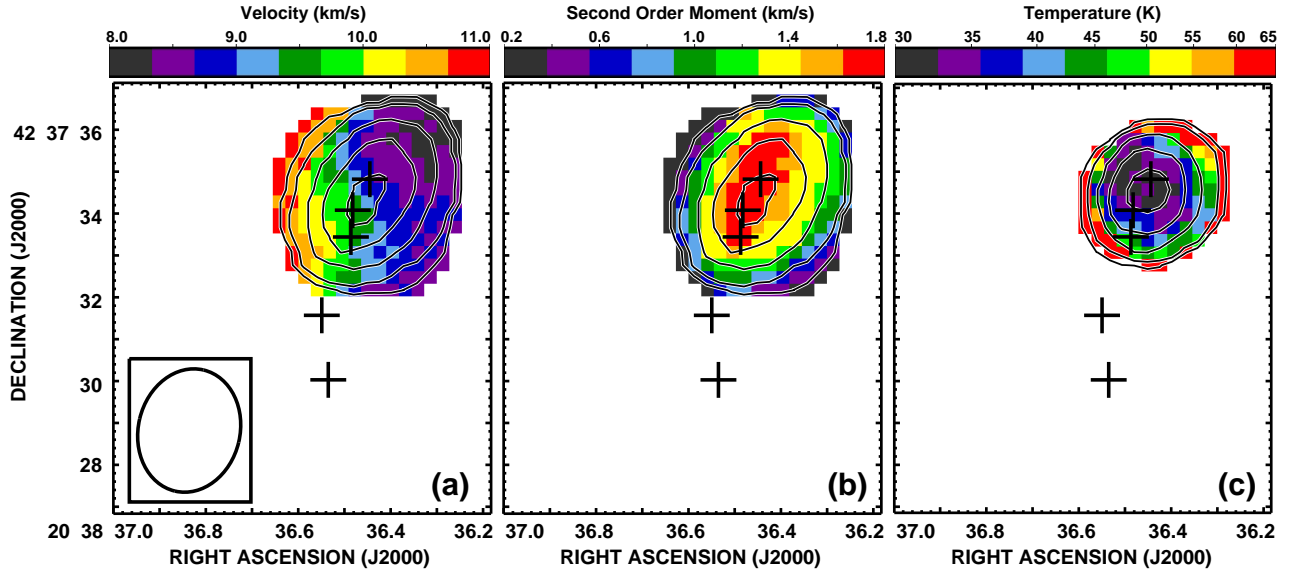
Figure 5.6 **(a)** Velocity field (moment 1) from the (2,2) transition of ammonia. The color wedge at the top gives the LSR radial velocity in km s^{-1}. The beam ($2\rlap{.}''97 \times 2\rlap{.}''43$; PA $= -13°$) is shown in the bottom left corner. In all panels the contours mark the integrated emission (moment 0) of the (2,2) emission, contours are 50, 100, 200, 300, and 400 mJy beam^{-1} km s^{-1}. The crosses mark the positions of the five radio sources. **(b)** Velocity dispersion (moment 2) of the (2,2) emission. For a Gaussian line the FWHM is 2.35 times the value of the velocity dispersion. **(c)** Rotational temperature of the gas, estimated from the (2,2)/(1,1) ratio, assuming optically thin emission and constant excitation conditions along the line of sight.

et al. 1993). The radio luminosity of source Bc is exceeded only by the radio HH objects associated with the luminous protostar IRAS 16547−4247, that with flux densities of ∼3-4 mJy at a distance of 2.9 kpc (Rodríguez et al. 2008) are the brightest known.

The radio flux density from source Bc allows to make an estimate of the mechanical luminosity of the jet that drives this source. Assuming that the continuum emission is optically-thin free-free at an electron temperature of 104 K, and taking into account that the source is at a distance of 2 kpc, in the order of ∼1.1×10^{45} ionizations per second are needed to maintain the source ionized. If these ionizations have a collisional origin and assuming that a minimum energy of 13.6 eV is needed per ionization, a mechanical luminosity of L$_{mech}$ ≥ 6 L$_{\odot}$ is estimated. Finally, assuming that the jet has a velocity of ∼200 km s^{-1}, a mass loss rate of order 10^{-6} M$_{\odot}$ yr^{-1} is inferred for the jet that is producing source Bc.

5.4.2   VLA 2, VLA 3, and VLA 4

These results lead to a revision of the nature of the radio sources in W75N. As commented above, Source Bc is most probably a bow shock produced by a jet. Several arguments suggest that this jet is driven by VLA 3: i) the source Bc and possibly VLA 4 move away from VLA 3, and this source is elongated in the direction of motion, ii) the spectral index is consistent with that expected for a radio jet, and iii) VLA 3 is the only source that has associated SiO emission (presumably tracing an outflow) and associated 7 mm (Shepherd et al. 2004) and 1

mm (Shepherd 2001) continuum emission, suggesting association with a disk or envelope.

VLA 4 is either an independent star or could be a previous ejection from VLA 3. Unfortunately, VLA 4 is not detected at 3.6 cm in 1992 or 1998, but a comparison of the 3.6 cm data from 2006 and of the 2 cm data from 2001 suggests a small displacement to the south. New sensitive observations are needed to test this hypothesis.

Finally, VLA 2 is most probably an independent, very young star. This source was associated with the very strong OH flare emission that reached in 2003 an emission of about 1000 Jy to become the brightest galactic OH maser in history (Alakoz et al. 2005; Slysh & Migenes 2006).

5.4.3   What is the nature of VLA 1?

Under the light of these results, one could propose that VLA 1 is the northern bow shock produced by the VLA 3 jet. However, in contrast to source Bc, VLA 1 does not show detectable proper motions along the axis of the VLA 3 jet. This behavior could be due to the existence of dense gas to its north that blocks motion along tha direction. In fact, as shown previously, VLA 1 is associated with dense gas traced by the NH3 observations. VLA 1 does show, however, a displacement in the peak of emission from east to west (see Fig. 5.2), nearly perpendicular to the axis of VLA 3 and similar to that observed in the radio HH objects associated with IRAS 16547−4247 (Rodríguez et al. 2008). In this latter source, this kinematic behavior has been interpreted as working surfaces where a precessing jet is interacting with a very dense medium. In this case, the HH objects would trace the present point of interaction between the jet and the dense medium.

We think, however, most likely that VLA 1 simply traces an independent young massive star. This source is known to be associated with intense maser emission from several molecules: water vapor (e.g., Lekht et al. 2009), methanol (e.g., Surcis et al. 2009), and hydroxil (e.g. Fish & Reid 2007). Intense maser emission is usually tracing the nearby presence of a young high-mass star. The proper motions observed in the water masers along the major axis of the VLA 1 source also favor this scenario (Torrelles et al. 2003). The linear polarization of the methanol masers revealing a tightly ordered magnetic field over more than 2000 AU around VLA 1 with a strength of 50 mG gives further support to the hypothesis that VLA 1 harbors a massive young star (Surcis et al. 2009). It is relevant to note that the flux density of VLA 1 remained constant within the noise during the three epochs of 3.6 cm observations, with all values consistent with 4.0±0.2 mJy.

5.5   Conclusions

We have analyzed VLA archive data of the W75N region. In the radio continuum, we detect five sources: VLA1, VLA2, VLA3, Bc, and VLA4, from north to south respectively. Our main conclusions are:

1. We detect important changes in total flux density, morphology, and position in the source Bc, suggesting that it is not tracing an independent star but actually is a radio HH object

powered by VLA 3. Its average velocity in the plane of the sky is 220±70 km s^{-1}. If our interpretation is correct, this is one of the brightest radio HH objects known.

2. We detect J = 1→0; v = 0 emission of SiO centered on VLA 3, probably tracing the inner parts of an outflow associated with this radio jet. Our results strongly support the identification of VLA 3 as a radio jet.

3. The large scale ammonia emission shows that the W75N region contains two filamentary molecular clouds with different radial velocities. The star formation is taking place at the intersection of these two filaments, which is also the hottest region. This suggests that the star formation could be triggered by the collision of the two filamentary clouds.

4. Strong and broad (1,1) and (2,2) ammonia emission is detected from the region containing the radio sources VLA 1, VLA 2, and VLA 3.

5. We detected a new radio continuum component, VLA 4, a few arcsec to the south of the group of previously known sources.

Bibliography

Alakoz, A. V., Slysh, V. I., Popov, M. V., Val'ts, I. E. 2005, Astronomy Letters, 31, 375

Anglada, G., Estalella, R., Mauersberger, R., Torrelles, J. M., Rodríguez, L. F., Cantó, J., Ho, P. T. P., D'Alessio, P. 1995, ApJ, 443, 682

Baart, E. E., Cohen, R. J., Davies, R. D., Rowland, P. R., Norris, R. P. 1986, MNRAS, 219, 145

Ballesteros-Paredes, J., Hartmann, L., Vázquez-Semanedi, E. 1999, ApJ, 527, 285

Beltrán, M. T., Estalella, R., Anglada, G., Rodríguez, L. F., Torrelles, J. M. 2001, AJ, 121, 1556

Carrasco-González, C., López, R., Gyulbudaghian, A., Anglada, G., Lee, C. W. 2006, A&A, 445, L43

Choi, M. 2005, ApJ, 630, 976

Curiel, S., Rodríguez, L. F., Moran, J. M., Cantó, J. 1993, ApJ, 415, 191

Devine, D., Bally, J., Chiriboga, D., Smart, K. 2009, AJ, 137, 3993

Eisloffel, J., Mundt, R., Ray, T. P., Rodríguez, L. F. 2000, Protostars and Planets IV, 815

Feigelson, E. D., Montmerle, T. 1999, ARA&A, 37, 363

Fischer, J., Sanders, D. B., Simon, M., Solomon, P. M. 1985, ApJ, 293, 508

Fish, V. L., & Reid, M. J. 2007, ApJ, 656, 952

Galván-Madrid, R., et al. 2010, in preparation

Garay, G., Ramírez, S., Rodríguez, L. F., Curiel, S., Torrelles, J. M. 1996, ApJ, 459, 193

Haschick, A. D., Reid, M. J., Burke, B. F., Moran, J. M., Miller, G. 1981, ApJ, 244, 76

Henriksen, R. N., Mirabel, I. F., Ptuskin, V. S. 1991, A&A, 248, 221

Ho, P. T. P., & Townes, C. H. 1983, ARA&A, 21, 239

Hunter, T. R., Taylor, G. B., Felli, M., Tofani, G. 1994, A&A, 284, 215

Hutawarakorn, B., Cohen, R. J., Brebner, G. C. 2002, MNRAS, 330, 349

Lekht, E. E., Slysh, V. I., Krasnov, V. V. 2009, Astronomy Reports, 53, 420

Martí, J., Rodríguez, L. F., Reipurth, B. 1993, ApJ, 416, 208

O'Dell, C. R., & Wong, K. 1996, AJ, 111, 846

Persi, P., Tapia, M., Smith, H. A. 2006, A&A, 445, 971

Rodón, J.A., Beuther, H., Megeath, S.T., Van der Tak, F.F.S. 2008, A&A, 490, 213

Rodríguez, L. F., Moran, J. M., Franco-Hernández, R., Garay, G., Brooks, K. J., Mardones, D. 2008, AJ, 135, 2370

Shepherd, D. S. 2001, ApJ, 546, 345

Shepherd, D. S., Testi, L., Stark, D. P. 2003, ApJ, 584, 882

Shepherd, D. S., Kurtz, S. E., Testi, L. 2004, ApJ, 601, 952

Slysh, V. I., Migenes, V. 2006, MNRAS, 369, 1497

Surcis, G., Vlemmings, W. H. T., Dodson, R., Van Langevelde, H. J. 2009, A&A, 506, 757

Torrelles, J. M., Gómez, J. F., Rodríguez, L. F., Ho, P. T. P., Curiel, S., Vázquez, R. 1997, ApJ, 489, 744

Torrelles, J. M., et al. 2003, ApJ, 598, L115

Vázquez-Semanedi, E., Gómez, G.C., Jappsen, A.K., Ballesteros-Paredes, J., González, R.F., Klessen, R.S. 2007, ApJ, 657, 870

Zapata, L. A., Rodríguez, L. F., Kurtz, S. E., O'Dell, C. R. 2004, AJ, 127, 2252

6

A Resolved Circumstellar Disk Around the Massive Protostar IRAS 18162−2048*

In this chapter we present new high angular resolution VLA observations at 1.3 cm and 7 mm, as well as SMA observations of the SO molecule towards the driving source of the HH 80-81 jet. At 1.3 cm the emission seems to be tracing the part of the radio jet closest to the origin, while the emission at 7 mm has a quadrupolar morphology and seems to be a combination of free-free and thermal dust emission. After substraction of the free-free emission we obtain an elongated structure, perpendicular to the jet. We modeled this structure as a circumstellar accretion disk with a radius of ∼400 AU and a mass of 14 $M_\odot$ around a star of 10 $M_\odot$. The submillimeter SO observations suggest the presence of molecular gas orbiting the massive star.

6.1   Introduction

The highly collimated HH 80-81 jet is driven by a massive protostar (IRAS 18162−2048), with a luminosity of $\sim 1.7 \times 10^4$ $L_\odot$ (equivalent to that of a B0 zero-age main sequence star; Aspin & Geballe 1992). It is located at a distance of 1.7 kpc (Rodríguez et al. 1980), and with a total extension of 5.3 pc, this is the largest and most collimated protostellar radio jet known so far (Martí et al. 1993). The thermal radio jet associated with HH 80-81 terminates to the south in the extremely bright optical HH objects 80 and 81 (Reipurth & Graham 1988; Martí et al. 1993, 1995; Heathcote, Reipurth, & Raga 1998) and to the north in the radio source HH 80 North (Martí et al. 1993; Girart et al. 1994, 2001).

Since the HH 80-81 jet very well collimated, it is expected that its driving source is associated with an accretion disk. However, until now there has been no clear evidence for the existence of this disk. Dense molecular gas traced by NH_3 (1,1) emission was reported by Torrelles et al. (1986) from single-dish observations. A CS molecular clump with an elongated structure ($\sim 60'' \times 25''$) has also been observed toward the exciting source of HH 80-81, and has been interpreted as a molecular disk (Yamashita et al. 1989). Gómez et al. (2003) detected thermal

dust continuum emission at 7, 3 and 1 mm associated with the exciting source. However, all those observations lack the angular resolution required to resolve the structure of a compact disk.

In order to study the dust emission of the circumstellar structure around the driving source of the HH 80-81 jet, we carried out 1.3 cm and 7 mm observations with the VLA. Additionally, we analysed VLA data at other wavelengths as well as SMA archive data.

6.2   Observations

6.2.1   VLA Observations

Observations at 1.3 cm and 7 mm continuum were carried out using the VLA in its A configuration. The same phase center (α(J2000) = $18^h19^m12.10^s$, δ(J2000) = $-20°47'31.0''$), phase calibrator (1820−254) and flux calibrator (3C286) were used at both wavelengths.

Data editing and calibration were performed using the AIPS package of NRAO, following the standard high-frequency VLA procedures. We made cleaned maps at 1.3 cm and 7 mm applying a tapering of 1750 kλ and 2100 kλ, respectively, in order to emphasize extended emission from the disk and the jet. We also analysed VLA A configuration archive data at 3.6 cm continuum. These data were obtained in 7 epochs from February 24, 1990 to May 18, 2006. We calibrated the data following standard VLA procedures. At each wavelength, we concatenated the data from the different epochs in order to improve the sensitivity of the maps. We made natural weighting maps at each wavelength. Additionally, we made uniform weighting maps from the concatenated data, giving higher weight to the long baselines visibilities in order to obtain higher angular resolution.

6.2.2   SMA Observations

Data in the 0.8 mm band were taken from the SMA (Ho et al. 2004) data archive. The observations were carried out during 2006 June 13 and 22. The first observation used the array in its Extended configuration, and the second observation was done in the Compact configuration. Both runs covered two sidebands spanning the frequency ranges 342.6-344.6 GHz and 352.6-354.6 GHz. The visibilities of each observation were calibrated separately using the SMA's data calibration program, MIR. For both runs, quasars 3C454.3 and 1924-292 served as bandpass and phase calibrators, respectively. The absolute flux scale was derived from observations of Callisto, and is accurate to better than $\sim 15\%$. Further processing and imaging was done in MIRIAD, AIPS, and IDL. In addition to the continuum emission, we detected line emission from the SO 8(8)-7(7) (ν_0 = 344.31061 GHz) transition.

The final continuum map was done from the Extended Configuration data with a uniform weighting (parameter ROBUST = -5; synthesized beam = $0\rlap{.}''97 \times 0\rlap{.}''70$, P.A.= -26°). The final SO maps were made from the concatenated Compact+Extended data with the parameter ROBUST set to 0 (synthesized beam = $1\rlap{.}''20 \times 0\rlap{.}''99$, P.A.= -34°).
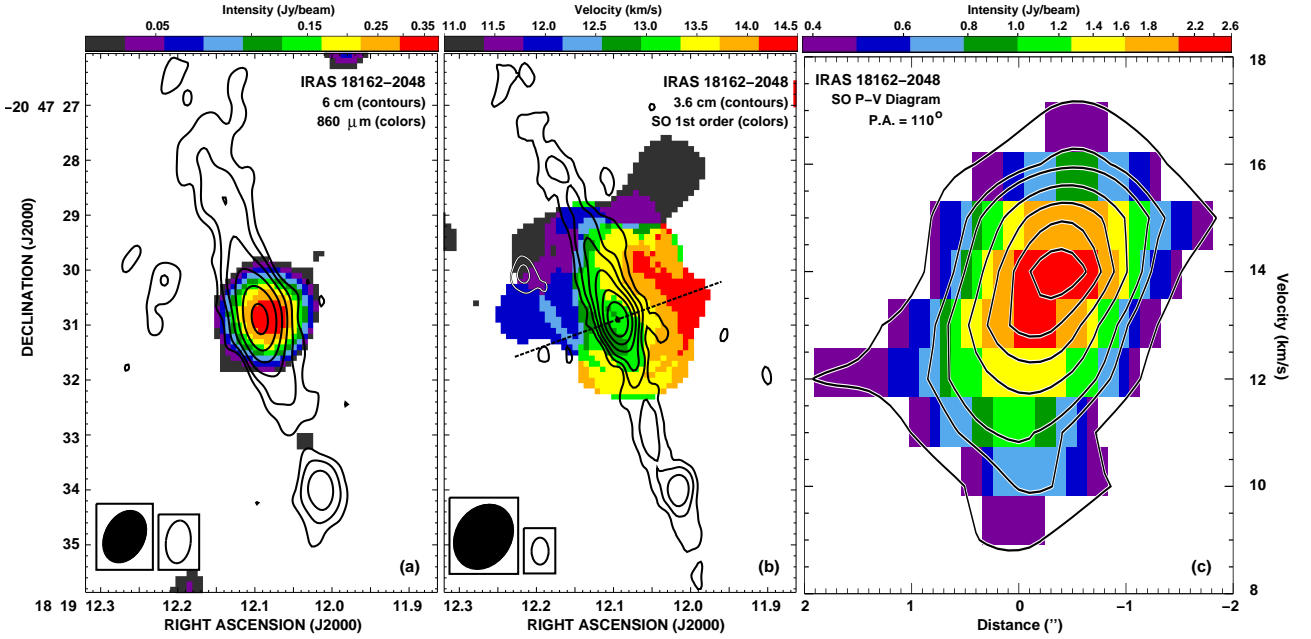
Figure 6.1 **(a)** Superposition of the 6 cm VLA natural weighting map (contours) over the 860 μm continuum SMA map (color scale; Extended Configuration, uniform weighting). Contours are 3, 6, 12, 25, 50, 100, and 200 times the rms of the VLA map, 15 μJy beam^{-1}. Color scales ranges from 0.02 to 0.4 Jy beam^{-1}. The rms of the SMA map is 5.8 mJy beam^{-1} **(b)** Superposition of the 3.6 cm VLA contour map over the SMA 1st order moment (velocity) map of the SO molecule emission. Contours are 3, 6, 12, 25, 50, 100, and 200 times the rms of the VLA map, 10 μJy beam^{-1}. Color scale ranges from 11.0 to 14.5 km s^{-1}. **(c)** Position-Velocity diagram (contours and color scale) obtained at the position of the star at a P.A. of 110° (perpendicular to the radio jet). Levels are 0.4, 0.8, 1.0, 1.4, 1.8, 2.2 and 2.6 Jy beam^{-1}.

6.3   Results and Discussion

In Figures 6.1a and 6.1b we show the VLA maps at 6 and 3.6 cm, as well as the 860 μm continuum map and the first order moment of the SO molecule emission obtained with the SMA. Our 6 and 3.6 cm maps are very similar to those previously obtained by Martí et al. (1995) at the same wavelengths. However, since we have concatenated data from several epochs, our maps are more sensitive. At both wavelengths, the radio jet appear with an elongated morphology along a P.A. of 20°.

Located 2″ to the NE of the center of the radio jet is a weak and compact source (VLA 2), previously detected by Gómez et al. (1995). For this source, we measured flux densities of 0.13 ± 0.03 mJy at 6 cm, and 0.12 ± 0.03 mJy at 3.6 cm. These flux densities imply a flat spectral index, which is indicative of thermal free-free emission. This source and the driving source of the radio jet coud be a binary system of YSOs, but with a large separation, since the projected separation is 3400 AU (370 stars are in binary systems wider than 2000 AU; Close et al. 1990)

We only detected 860 μm continuum emission towards the center of the radio jet (see Figure 6.1a). This emission appears compact, with a deconvolved size of ~0.7″ (~1200 AU) and a flux density of 580±10 mJy. As will be discussed in the next section, this emission is most probably

Table 6.1.   Parameters of 1.3 cm components

| Component | Position (J2000)[a] | | Flux Density | Deconvolved |
	RA	DEC	(mJy)	Angular Size[b]
North	18 19 12.098	−20 47 30.46	0.7 ± 0.2	0.″30 × 0.″11 ; 40° ± 20°
Central	18 19 12.094	−20 47 30.91	1.7 ± 0.2	0.″23 × 0.″07 ; 10° ± 7°
South	18 19 12.084	−20 47 31.11	1.2 ± 0.2	0.″33 × 0.″09 ; 24° ± 10°

[a]Units of right ascension are hours, minutes, and seconds and units of declination are degrees, arcminutes, and arcseconds. The absolute positional accuracy is estimated to be 0.″02.

[b]Major axis × minor axis; positon angle of major axis. Uncertainty in major and minor axis is estimated to be 0.″05.

thermal dust emission.

The SO molecule emission shows an extended morphology with the driving source of the radio jet located in its center (see Figure 6.1b). This suggests that the SO emission is tracing a dense envelope of molecular gas around IRAS 18162−2048. The position of the source VLA 2 appears in projection near the edge of the SO molecule emission, however, it is unclear if this source is also physically associated with the molecular gas.

As can be seen in Figure 6.1b, the SO emission shows a velocity gradient, roughly perpendicular to the radio jet. We interpret this velocity gradient as due to gravitationally bound rotational motions. We can infer the dynamical mass enclosed within a radius r using the equation

$$\left(\frac{M}{M_\odot}\right) = 1.13 \times 10^{-3} \left(\frac{v_r}{\mathrm{km\ s^{-1}}}\right)^2 \left(\frac{r}{\mathrm{AU}}\right),\tag{6.1}$$

where, v_r is the rotation velocity of the gas at radius r. In Figure 6.1c, we show a position-velocity diagram along a direction perpendicular to the radio jet. From this diagram we measure a velocity gradient of ∼3 km s^{-1} over ∼1″ (≃1700 AU). If we assume an inclination angle of 90° (the HH 80-81 jet is almost in the plane of the sky), we obtain a minimum binding mass of 17 M$_\odot$. This implies that the observed motions can be bound if the central protostar is a B0, the same spectral type inferred by the bolometric luminosity of IRAS 18162−2048. Since the molecular gas seems to be rotating around the driving source of the radio jet, our results strongly suggests that effectively, the HH 80-81 jet is driven by a massive protostar.

In Figure 6.2a, we show the superposition of our VLA 7 mm (contours) and 1.3 cm (color scale) maps covering the central region of the radio jet. The higher angular resolution of these maps (∼0.″15 at 1.3 cm; ∼0.″10 at 7 mm) allow us to resolve the structure of the core of the radio jet. The 1.3 cm emission shows a jet-like morphology, consisting in a bright central source and two weaker sources to NE and SW. The positions, flux densities and deconvolved sizes of each 1.3 cm sources are given in Table 6.1. The global orientation of the 1.3 cm emission is similar to that of the larger scale radio jet detected at 6 and 3.6 cm. However, the central
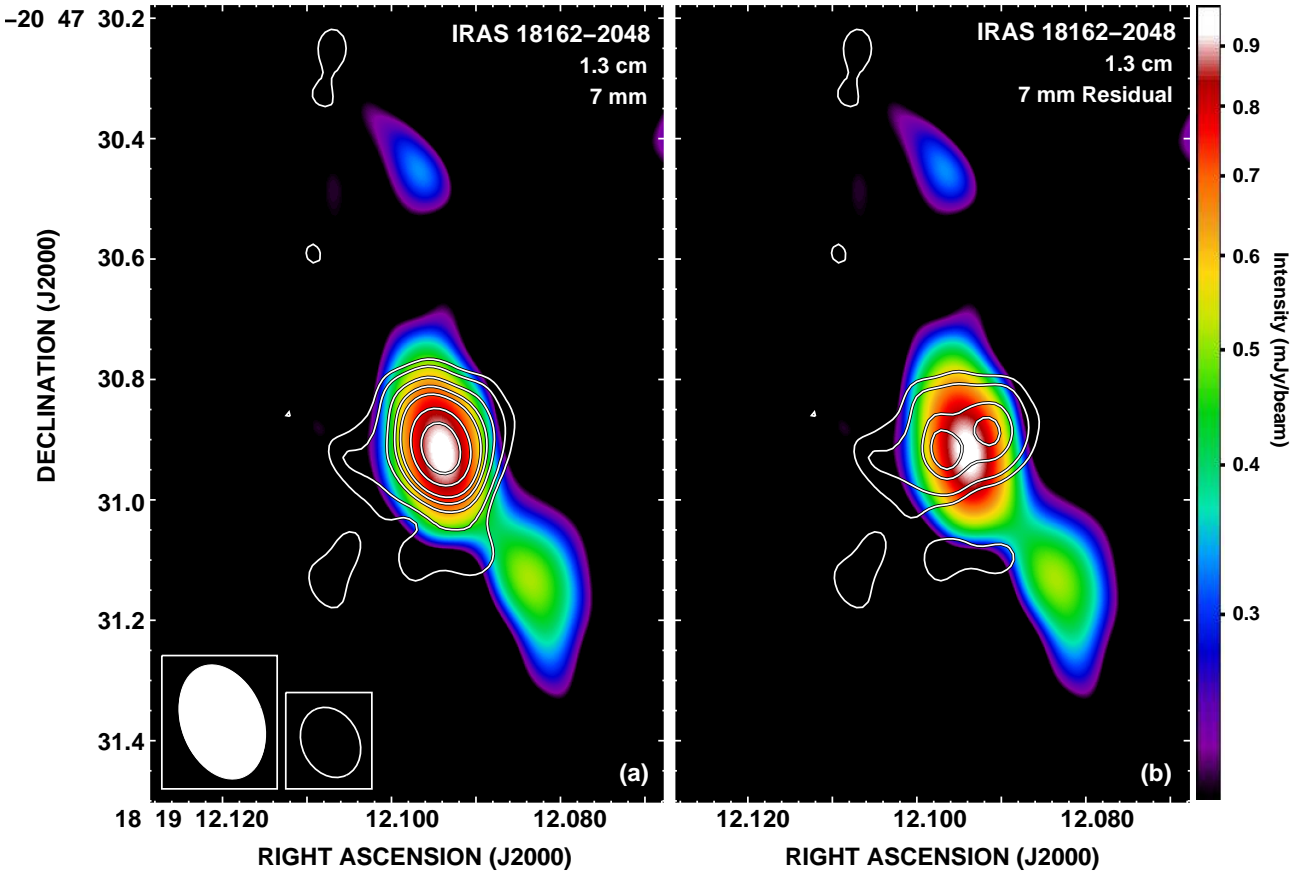
Figure 6.2 **(a)** Superposition of the 7 mm VLA contour map over the 1.3 cm VLA map (colors). Contours are 3, 4, 6, 8, 10, 14 and 18 times the rms of the map, 120 μJy beam^{-1}. **(b)** Same as a, but after substraction of the free-free contribution at 7 mm.

1.3 cm source is oriented at a P.A.$\simeq$10° at scales of $\sim$0$''$1-0$''$2, while at larger scales ($\sim$0$''$5) the jet is oriented at P.A.$\simeq$20°. This suggests a precession of the jet axis.

Emission at 7 mm is detected only towards the center of the radio jet and shows a quadrupolar morphology which can be described as the superposition of two overlapping, elongated sources. We have fitted the 7 mm source with two Gaussian ellipsoids using the task JMFIT of the AIPS package. The positions, flux densities and deconvolved sizes obtained for each component are shown in Table 6.2. Both components are extended with perpendicular orientations (roughly N-S and E-W) and similar flux densities ($\sim$3 mJy; see Table 6.2).

Similar quadrupolar morphologies have been observed in other radio jets of low-mass stars at wavelengths where comparable contributions of free-free emission from the radio jet and thermal dust emission from a perpendicular disk are present (e.g., HL Tau at 1.3 cm: Carrasco-González et al. 2009; HH 111 at 7 mm: Rodríguez et al. 2008). In Figure 6.3a, we show the SED of the source IRAS 18162−2048 in the range from 6 cm to 860 μm. As can be seen in this figure, the extrapolation of the free-free emission detected at cm wavelengths cannot account for the total flux density detected at 7 mm, suggesting that an additional contribution from thermal dust emission is present. Therefore, we interpret the morphology of the 7 mm emission as the result of a combination of free-free emission from an ionized jet (N-S component) and thermal dust

Table 6.2.   Decomposition of the 7 mm Continuum Emission in Two Components

Component	Position (J2000)[a]		Flux Density	Deconvolved
	RA	DEC	(mJy)	Angular Size[b]
N-S (Jet)	18 19 12.094	−20 47 30.92	2.7 ± 0.3	0″.12 × 0″.02 ; 11° ± 7°
E-W (Disk)	18 19 12.096	−20 47 30.90	3.6 ± 0.5	0″.23 × 0″.13 ; 110° ± 10°

[a]Units of right ascension are hours, minutes, and seconds and units of declination are degrees, arcminutes, and arcseconds. The absolute positional accuracy is estimated to be 0″.02.

[b]Major axis × minor axis; positon angle of major axis. Uncertainty in major and minor axis is estimated to be 0″.02.

emission from a perpendicular circumstellar disk (E-W component). In Figure 6.2b we show a superposition of the 7 mm emission of the disk over the 1.3 cm emission of the radio jet. In what follows, we discuss the validity of our interpetation.

The 7 mm N-S component is oriented in the same direction that the radio jet, and therefore, this emission is most likely tracing the innermost part of the thermal radio jet. From the model of Reynolds (1986) it is found that the flux density (S_ν) and angular size (θ_ν) of the radio continuum emission from a thermal jet, with constant velocity, temperature, and ionization fraction, are functions of the frequency, with the form $S_\nu \propto \nu^{1.3-0.7/\epsilon}$ and $\theta_\nu \propto \nu^{-0.7/\epsilon}$, respectively, where ϵ is the power-law index that describes how the width of the jet varies with the distance from the central object ($\epsilon =1$ corresponds to a conical, constant opening angle, jet). In Figures 6.3a and 6.3b we show least squares fits of the flux densities and deconvolved sizes of the core of the radiojet obtained from Gaussian fits to the 6, 3.6, and 1.3 cm maps and to the 7 mm N-S component. From these fits, we obtained $S_\nu \propto \nu^{0.7 \pm 0.1}$ and $\theta_\nu \propto \nu^{-0.5 \pm 0.1}$, which, within the uncertainties, are in good agreement with the model of Reynolds (1986) for a thermal jet with ϵ in the range 1.2-1.4.

The 7 mm E-W component, oriented in the direction perpendicular to the radio jet, traces a structure with a size of ∼400 AU centered on the driving source (see Figure 6.2b). We interpret this structure as tracing thermal dust emission from a circumstellar accretion disk. In order to test this possibility, we modeled the VLA 7 mm and SMA 850 μm emission, using physically self-consistent α-disk models (D'Alessio et al 1998, 1999, 2001, 2006). These models have successfully reproduced the SED and spatial intensity profiles of disks in low- and intermediate-mass protostars. We assumed that contamination from a possible infalling envelope is negligible at 7 mm since the interferometer resolved out the large scale structures. However, at 850 μm, since we are detecting emission from a more extended region, a contribution from the envelope could be important, and thus, the flux density at this wavelength is considered as an upper limit to the flux density of the disk. The disk model assumes the α prescription for the viscosity (Shakura & Sunyaev 1973). In these models the disk structure is solved for a given mass acrecion rate, mass of the central star, and viscosity parameter α. Once the disk structure is
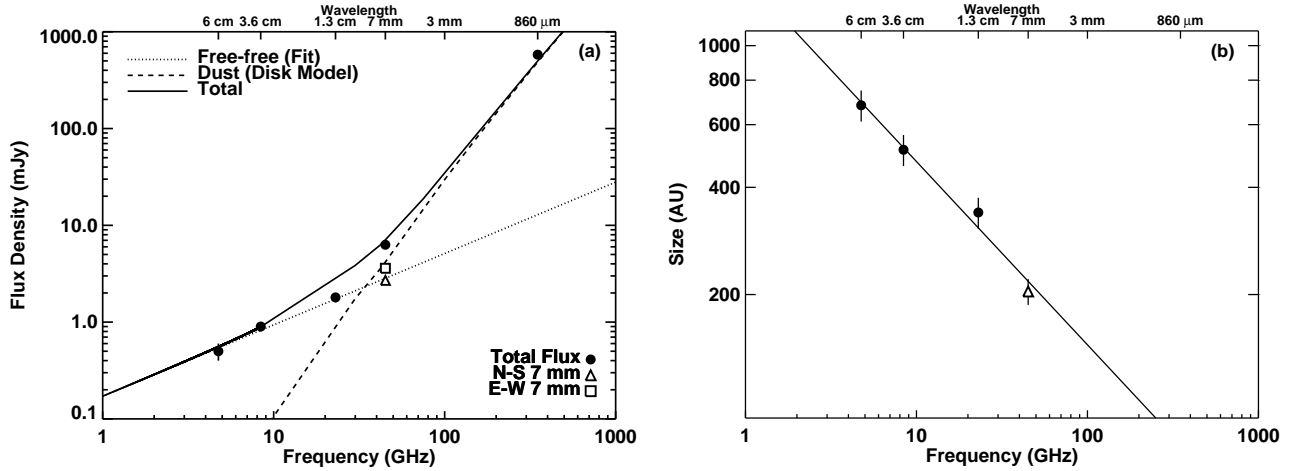
Figure 6.3 **(a)** Spectral Energy Distribution of IRAS 18162−2048 in the wavelength range from 6 cm to 860 μm. Black circles correspond to the total flux density obtained at each wavelength. The flux densities at 6 and 3.6 cm were obtained from uniform weighting maps made including the visibilities of the longest baselines (see Section 2). The triangle corresponds to the flux density of the 7 mm N-S component. The box corresponds to the flux density of the 7 mm E-W component. The dotted line is a least squares fit to the cm wavelength data. Dashed line corresponds to a disk model for a central stellar mass of 10 $M_\odot$, an accretion rate of 7×10^{-6} $M_\odot$ yr^{-1}, and a disk radius of 420 AU (see text). Solid line corresponds to the sum of the free-free and thermal dust emission contributions. **(b)** Deconvolved size of the radio jet as a function of the frequency. The triangle corresponds to the deconvolved size of the 7 mm N-S component. The solid line is a least squares fit to the data.

obtained, the monochromatic radiative transfer equation is integrated through the disk and the flux density is calculated.

According to Panagia (1973), a B0 spectral type star with a mass of 10 $M_\odot$, radius of 5 $R_\odot$ and effective temperature of 26000 K provides a central luminosity of 11000 $L_\odot$, similar to the bolometric luminosity observed in the region. We assumed that the dust composition of the disk is similar to the Draine & Lee (1984) mixture, with compact spherical grains whose maximum size is 1 mm. The dust properties correspond to an absorption coefficient κ (7mm) = 0.005 cm^2 g^{-1}.

We constructed a grid of models varying the mass accretion rate from 10^{-6} to 3×10^{-5} $M_\odot$ yr^{-1}, the α viscosity parameter from 0.1 to 0.01, the inclination angle of the disk (angle between the line of sight and the polar axis) in the range 40°-80°, and the radius of the disk in the range 200-500 AU. We consider as valid those models that simultaneously fit the observed SED and spatial profile (after convolution with the synthesized beam of our observations) of the 7 mm source.

Although several models explain the integrated flux density, only a few of them are able to reproduce the size of the 7 mm emission. In Figure 6.3a, we show the SED of a model that corresponds to a circumstellar disk with a radius of 420 AU and a mass of 14 $M_\odot$. Note that from the SO observations discussed in section 6.3.1, we estimated a lower limit to the central binding mass of 17 $M_\odot$, which is in good agreement with the 24 $M_\odot$ (star+disk) that we obtain

by the modeling of the disk. The required accretion rate (7×10^{-6} M$_\odot$ yr^{-1}) for this model implies a luminosity of the disk of 200 L$_\odot$, that is negligible in comparison with the stellar luminosity, which is one of the main sources of irradiation of the disk.

Up to date, several disks around massive stars have being found (see review of Cesaroni et al 2006). Some of them are classified as rotating toroids, with sizes of the order of several thousands of AU and masses several orders of magnitude higher than that of the central stellar mass. The disk associated to IRAS 18162−2048 does not appear to be similar to these structures, but it is more similar to the small and less massive "true" disks frequently found around low- and intermediate-mass stars.

6.4   Conclusions

We performed high angular resolution observations with the VLA and SMA towards the driving source of the HH 80-81 radio jet. We detected continuum emission at 6 cm, 3.6 cm, 1.3 cm, 7 mm, and 860 μm, and SO 8(8)-7(7) line emission associated with driving source of the radio jet. Our main conclusions can be summarized as follows:

1. The SO emission traces molecular gas orbiting around the driving source of the radio jet. From the velocity gradient of the SO emission, we estimate a lower limit to the central binding mass of 17 M$_\odot$.

2. The 1.3 cm emission shows a jet-like morphology, and it is most likely tracing the innermost part of the radio jet.

3. The flux density and quadrupolar morphology detected at 7 mm suggests that the emission at this wavelength is a combination of free-free emission from the radiojet, and thermal dust emission from a perpendicular disk.

4. After substraction of the free-free emission, we successfully modeled the flux density and size of the 7 mm emission as arising from an accretion disk with a radius of 420 AU, an accretion rate of 7×10^{-6} M$_\odot$ yr^{-1}, and a mass of 14 M$_\odot$, orbiting around a 10 M$_\odot$ protostar.

Bibliography

Aspin, C., Geballe, T.R. 1992, A&A, 266, 219

Carrasco-González, C., Rodríguez, L.F., Anglada, G., Curiel, S. 2009, ApJL, 693, 86

Cesaroni, R., Galli, D., Lodato, G., Walmsley, M., Zhang, Q. 2006, Nature, 444, 703

Close, L.M., Richer, H.B., Crabtree, D.R. 1990, AJ, 100, 1968

D'Alessio, P., Calvet, N., Hartmann, L., Lizano, S., Cantó, J. 1999, ApJ, 527, 893

D'Alessio, P., Calvet, N., Hartmann, L. 2001, ApJ, 553, 321

D'Alessio, P., Calvet, N., Hartmann, L., Franco-Hernández, R., Servín, H. 2006, ApJ, 638, 314

D'Alessio, P., Cantó, J., Calvet, N., Lizano, S. 1998, ApJ, 500, 411

Girart, J.M., Rodríguez, L.F., Anglada, G., Estalella, R., Torrelles, J.M., Martí, J., Pena, M., Ayala, S., Curiel, S., Noriega-Crespo, A. 1994, ApJ, 435, 145

Girart, J.M., Estalella, R., Viti, S., Williams, D.A., Ho, P.T.P. 2001, ApJ, 562, 91

Gómez, Y., Rodríguez, L. F., Girart, J. M., Garay, G., Martí, J. 2003, ApJ, 597, 414

Gómez, Y., Rodríguez, L.F., Martí, J. 1995, ApJ, 453, 268

Heathcote, S., Reipurth, B., Raga, A.C. 1998, AJ, 116, 1940

Ho, P.T.P., Moran, J.M., Lo, K.Y. 2004, ApJ, 616, 1

Martí, J., Rodríguez, L.F., Reipurth, B. 1993, ApJ, 416, 208

Martí, J., Rodríguez, L.F., Reipurth, B. 1995, ApJ, 449, 184

Reipurth, B., Graham, J.A. 1988, A&A, 202, 219

Reynolds, S.P. 1986, ApJ, 304, 713

Rodríguez, L.F., Moran, J.M., Ho, P.T.P., Gottlieb, E. W. 1980, ApJ, 235, 845

Rodríguez, L.F., Torrelles, J.M., Anglada, G., Reipurth, B. 2008, AJ, 136, 1852

Shakura, N.I. & Sunyaev, R.A. 1973, A&A, 24, 337

Siess, L., Dufour, E., Forestini, M. 2000, A&A, 358, 593S

Torrelles, J.M., Ho, P.T.P., Moran, J.M., Rodríguez, L.F., Cantó, J. 1986, ApJ, 307, 787

Yamashita, T., Suzuki, H., Kaifu, N., Tamura, M., Mountain, C.M., Moore, T.J.T. 1989, ApJ, 347, 894

7

A Magnetized Jet from the Massive Protostar IRAS 18162−2048*

In this chapter we report the first definitive evidence of synchrotron emission arising from the jet of a young stellar object. We detected linearly polarized radio emission that allowed us to measure the strength and direction of the magnetic field. We find that the characteristics of the synchrotron emission and the configuration of the magnetic field in this jet are strikingly similar to those of AGN jets, suggesting that the flow carries large-scale helical magnetic fields. This is the first time that the structure and strength of the magnetic field have been observationally studied in a jet from a protostar, and represents an important step in the unification of the collimated outflow phenomena observed in many astrophysical contexts.

7.1   Introduction

It is though that the magnetic field should play an important role in the star formation process. The accretion disk drags magnetic field lines onto the protostar increasing the magnetic pressure in the accretion disk. A fraction of the accreting material is launched as a collimated jet via magnetocentrifugal forces in the disk (e.g., Blandford & Payne 1982; Kigure & Shibata 2005). This jet carries out part of the magnetic flux, thus decreasing the magnetic pressure in the disk. However, despite its important role in the formation of stars, the magnetic field remains the poorest known ingredient, mainly because of the difficulty to be observed and measured at the small scales that characterize star formation. Some recent works (e.g., Girart et al. 2006, 2009) have succeeded in observing, through dust polarization, the magnetic field at scales small enough to appreciate the distortion of the magnetic field lines due to the gravitational contraction process in the immediate environment of protostars. Also, certain maser transitions from molecules, in particular OH (hydroxyl), H_2O (water vapor), and CH_3OH (methanol), have been used to study magnetic fields in regions of star formation (e.g. Fish & Reid 2007; Sarma

et al. 2008; Vlemmings 2008). However, these masers trace neutral molecular components that are very different in nature to the high excitation collimated outflows. So far, there have been no direct observations of both the magnetic field direction and strength in these jets.

A very powerful method to simultaneously obtain the structure and strength of the magnetic field is through observations of the synchrotron emission from jets. When electrons move at relativistic velocities in the presence of a magnetic field, they radiate linearly polarized light at radio wavelengths. The spectrum of the synchrotron emission in the centimeter wavelength range is characterized by a negative spectral index, and it is related to the strength of the magnetic field. Additionally, the direction of the polarization is perpendicular to the direction of the magnetic field. This method has been the most successful in the study of the magnetic field in jets from AGNs (Fanaroff & Riley 1974; Bridle & Perley 1984) and microquasars (Mirabel & Rodríguez 1994; Brocksopp et al. 2007) where the ejected material moves at relativistic velocities. In contrast, protostellar jets, where the bulk of the material moves at much smaller velocities (200-1000 km s^{-1}; Martí et al. 1995, Curiel et al. 2006, Pech et al. 2010) apparently would lack relativistic electrons that can provide information on the magnetic field, and the emission is usually dominated by a different mechanism (free-free emission originated from the thermal motions of the electrons, characterized by a positive spectral index). Intriguingly, in a few protostellar jets (Serpens: Rodríguez et al. 1989; HH 80-81: Martí et al. 1993; Cepheus A: Garay et al. 1996; W3(H$_2$O): Wilner et al. 1999; IRAS 16547−4247: Rodríguez et al. 2005), emission with negative spectral indices, that could correspond to non-thermal synchrotron emission from relativistic electrons, has been reported. In this case, the acceleration of particles would be most likely produced where the fast thermal jet impacts on the surrounding medium and a strong shock wave is formed. Thus, particles might be accelerated up to relativistic energies by the Fermi mechanism (e.g. Bell 1978). In order to confirm the presence of synchrotron radiation in these protostellar jets, a clear detection of linearly polarized radio emission is required.

In this chapter, we present new 6 cm VLA observations of the HH 80-81 jet. We detected linearly polarized emission associated with the knots of the radio jet. This confirms that the emission is of synchrotron nature, and has allowed us to study, for the first time in a protostellar jet, the structure of the magnetic field.

7.2   Observations

Continuum observations at 6 cm were made using the VLA in its C Configuration. The observations were performed with the VLA in its C configuration on August 12nd and 22nd, 2009. The total observation time was 12 hours. The data were calibrated in amplitude, phase, and linear polarization. The flux calibrator was 3C286, while phase and linear polarization calibration was achieved by observing 1751-253. Data editing and calibration were carried out using the AIPS package of NRAO, following the standard VLA procedures.

Images at 6 cm continuum and linear polarization were made using a tapering of 20 kλ in order to emphasize extended emission. The rms of the maps is 0.013 mJy beam^{-1}, and the

synthesized beam is 13" × 8" with a position angle of 2°.

7.3   Results and Discussion

Figure 7.1a shows our radio continuum image of the HH 80-81 jet. The radio jet consists of a chain of radio sources aligned in a SW-NE direction. The brightest radio knot is associated with the central protostar, IRAS 18162−2048. To the SW, the radio jet terminates in the optical/radio Herbig-Haro objects HH 80 and HH 81, while to the NE, it terminates in the radio Herbig-Haro object HH 80 N. Early radio observations (Martí et al. 1993) showed that the emission from the central source is characterized by a positive spectral index, suggesting that it is dominated by thermal free-free emission. In contrast, the Herbig-Haro objects HH 80-81, HH 80 N, as well as some of the knots nearer to the protostar showed evidence of negative spectral indices, suggesting the presence of an additional non-thermal emission component.

In Figure 7.1b, we show the linear polarization intensity image of the HH 80-81 radio jet. As can be seen in this figure, linearly polarized emission is clearly detected in the knots of the radio jet located $\sim 1'$ from the driving source. This detection of linearly polarized radiation in the HH 80-81 radio jet is the first observational confirmation that an important contribution of synchrotron emission is present in the knots of a jet from a protostar. There are two other mechanisms (besides synchrotron radiation) that could produce the linear polarization observed in the jet of HH 80-81. However, it can be seen that they are insufficient since their optical depths are negligible at radio wavelengths. A first possibility is that we are observing Thomson (i.e. electron) scattering of the radio emission from the central source. This mechanism would produce a polarization pattern similar to that observed. Assuming that part of the radio continuum emission is thermal, optically-thin free-free, and that the region is at a distance of 1.7 kpc (Rodríguez et al. 1980) an upper limit of $n_e \leq 10^3$ cm^{-3} is obtained for the electron density in the polarized lobes of the radio jet. From the observed source size of $R \sim 10^{17}$ cm, and since the Thomson cross section is $\sigma_T = 6.65 \times 10^{-25}$ cm^2, we obtain an upper limit of $\tau_T = n_e\, R\, \sigma_T \leq 7 \times 10^{-5}$, for the Thomson opacity, clearly insufficient to produce the observed polarized emission, since an opacity several orders of magnitude higher is required to produce the observed polarized intensity in the lobes of the radio jet. A second mechanism that produces a polarization pattern similar to that observed in the jet of HH 80-81 is dust dispersion. The region surrounding IRAS 18162−2048 has large dust extinction. Gómez et al. (2003) estimate an H_2 column density of $\sim 3 \times 10^{22}$ cm^{-2}, that translates into a visible opacity of $\tau_V \simeq 30$. However, the cross section for dust scattering scales as λ^{-4} (Draine 2003) and its effect is negligible at centimeter wavelengths.

The observed polarization vectors are perpendicular to the direction of the jet, with a degree of polarization of the order of 10-30%. The direction of the apparent magnetic field (the component in the plane of the sky averaged over the line-of-sight; Laing 1981, Lyutikov et al. 2005) is taken to be perpendicular to the polarization vectors (this is correct for a non-relativistically moving source, such as the HH 80-81 jet; for relativistic jets, such as AGN jets, additional assumptions on the velocity field are required; Laing 1981, Lyutikov et al. 2005).
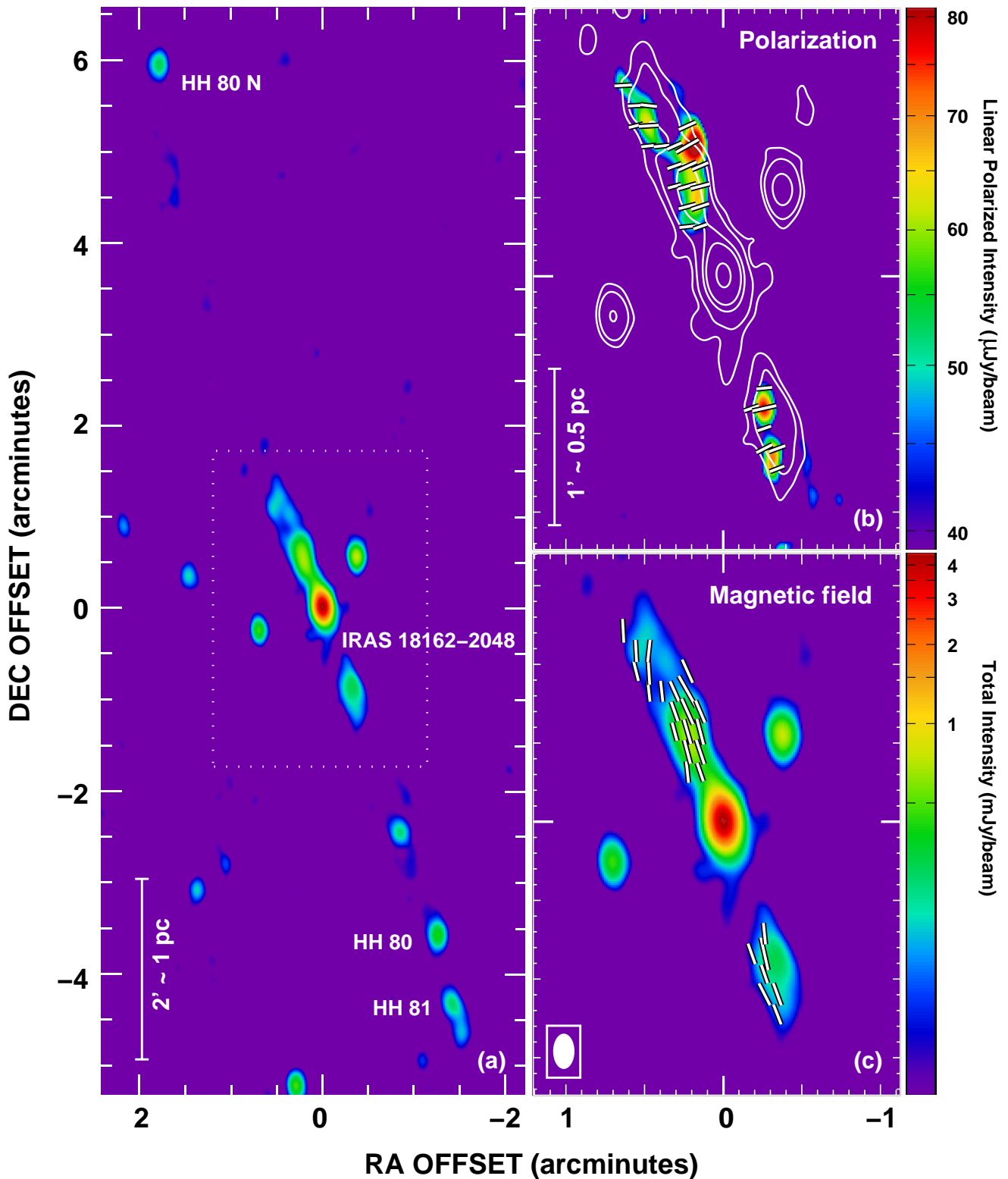
Figure 7.1 Maps of the HH 80-81 jet region at 6 cm wavelength. (see Martí et al. 1993 for a complete description of the radio sources shown in this region) **(a)** Image of the total continuum intensity, showing the whole extension of the HH 80-81 jet. The rectangle marks the central region of the jet, which is shown in the other two panels. **(b)** Linearly polarized continuum intensity image (color scale). The direction of the polarization is shown as white bars. The total continuum intensity is also shown (contours). Contours levels are 40, 100, 400, 850, and 3300 μJy beam^{-1}. **(c)** Magnetic field vectors (white bars) superposed with the total continuum intensity image (color scale). The (0,0) offset position corresponds to the phase center of the observations, at right ascension (J2000) = $18^h\,19^m\,12.102^s$, declination (J2000) = $-20°\,47'\,30.61"$.

As can be seen in Figure 7.1c, the apparent magnetic field appears very well aligned with the direction of the HH 80-81 radio jet.

Once we have confirmed with the detection of polarization that the radio emission is of synchrotron nature, we can derive the minimum total energy in the radiating region of the jet and the corresponding equipartition magnetic field using the equations of Pacholczyck (1970):

$$E = c_{13}(1+k)^{4/7}\phi^{3/7}R^{9/7}L_R^{4/7}, \tag{7.1}$$

$$B = (4.5c_{12}(1+k)/\phi)^{2/7}R^{-6/7}L_R^{2/7}, \tag{7.2}$$

where ϕ is the filling factor of the emitting region, R is the source size, L_R is the integrated radio luminosity, k is the ratio between the heavy particle energy and the electron energy, and c_{12} and c_{13} are functions of the spectral index, and of the minimum and maximum frequencies considered in the integration of the spectrum. To obtain the radio luminosity, we integrated the radio spectrum in the range between 20 and 2 cm using the flux density measurements of Martí et al. (1993). We used a filling factor of $\phi=0.5$, and $k=40$ (which is appropriate for acceleration in a non-relativistic shock; Beck & Krause 2005). With these parameters, we obtain typical values for the knots of the radio jets of $B \simeq 0.2$ mG, and $E \simeq 8 \times 10^{43}$ erg.

The good alignment between the HH 80-81 jet and the magnetic field inferred from the synchrotron emission contrasts with the results obtained from dust polarization (Curran et al. 2007). The observations of Curran et al. (2007) reveal that the direction of the magnetic field near the protostar shows considerable scatter with respect to the direction of the jet. This is illustrated in Figure 7.2, where we show a histogram of the difference between the position angle of the jet and the measured direction of the magnetic field. As can be seen from the figure, while the direction of the magnetic field obtained from the synchrotron emission is strongly concentrated in a direction very close to the jet axis (typically within ~ 15 degrees), the direction of the magnetic field inferred from dust polarization spreads over a much more wide range of values (typically within ~ 60 degrees). These results strongly suggest that while dust polarization traces the magnetic field associated with the ambient material close to the protostar, the synchrotron emission traces the magnetic field intrinsically associated with the jet.

The magnetic field observed in the jet is most likely being carried by the outflow and not due to the ambient medium. Curran et al. (2007) estimate values of 0.2 mG for the magnetic field in the region $\sim 0.2'$ around IRAS 18162−2048, the driving source of the HH 80-81 jet. If we assume that this field behaves like a dipole, it should drop with distance cubed along the axis of the outflow. However, even at $\sim 1'$ from IRAS 18162−2048 the magnetic field in the jet remains comparable to that observed in the core by Curran et al. (2007), when it should have decreased by more than a factor of 100. Additional evidence that the observed magnetic field is intrinsic to the jet and most probably comes from the disk is that the outflow remains very fast and does not appear to entrain large amounts of matter from the interstellar medium as it travels away from the central source. Martí et al. (1998) determine velocities in the
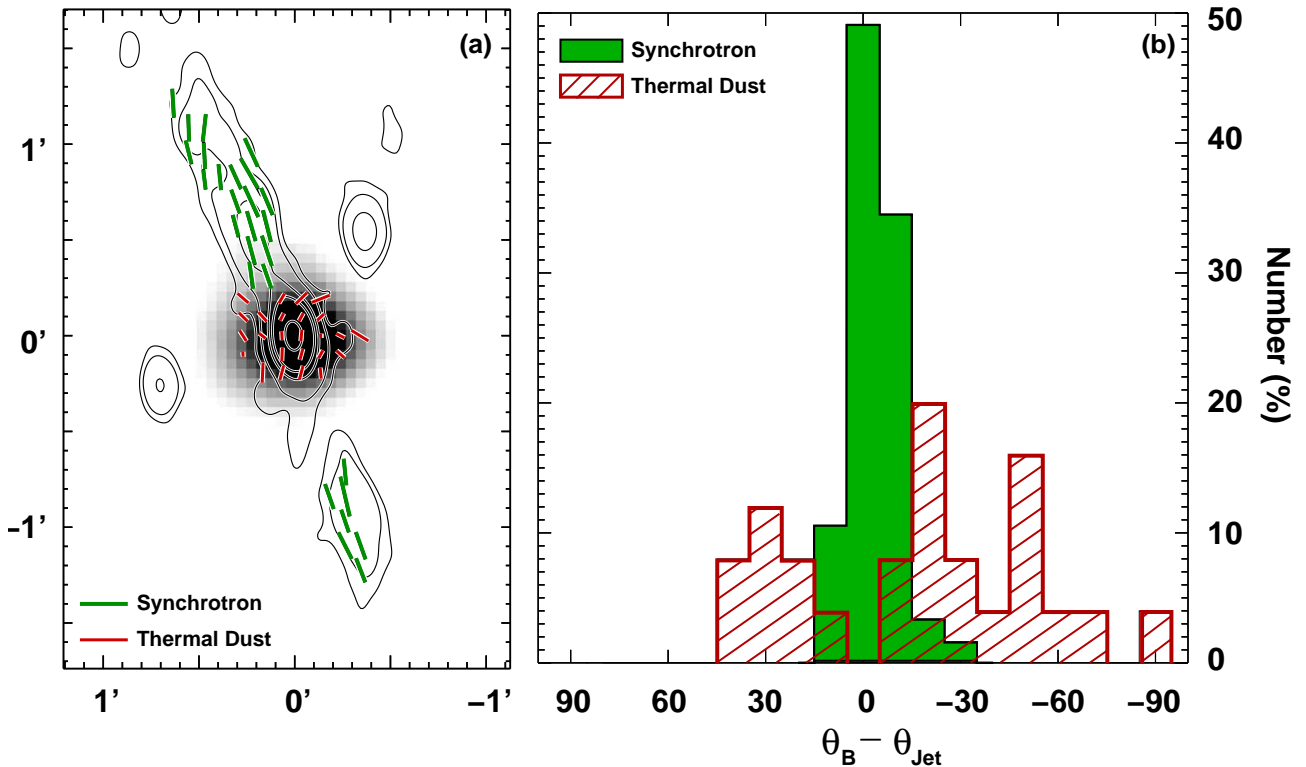
Figure 7.2 **(a)** Map of the continuum emission of the HH 80-81 jet, at 6 cm (contours; this paper) superposed with the dust continuum emission at 850 μm (grey scale; Curran et al. 2007). Green bars mark the direction of the magnetic field inferred from the polarized synchrotron emission detected in our VLA observations. Red bars mark the magnetic field inferred from the dust polarization emission detected by Curran et al. (2007). **(b)** Histograms of the difference between the position angle of the jet and the measured direction of the magnetic field. The green histogram shows the results obtained from the synchrotron emission, while the red dashed histogram shows the results obtained by Curran et al. (2007) from dust polarization. Note that while the direction of the magnetic field obtained from the synchrotron emission is strongly concentrated in a direction very close to the jet axis (typically within ~ 15 degrees), the direction of the magnetic field inferred from dust polarization spreads over a much wider range of values (typically within ~ 60 degrees).

plane of the sky of $\sim$500 km s^{-1} for the motion of newly ejected condensations within 100 AU from IRAS 18162−2048. At a distance of a few pc (thousands of times larger than the scale where the new condensations were observed), Heathcote et al. (1998) find proper motions of $\sim$350 km s^{-1} for the HH objects 80 and 81. The similar velocities found at these two very different scales suggests that the bulk of the jet does not decelerate significantly and retains the magnetic field it had close to the protostar.

The polarization properties and the magnetic field configuration in the HH 80-81 jet are very similar to those observed in AGN jets. In AGN jets the polarization is always observed either perpendicular or parallel to the axis of the jet (e.g., Lyutikov et al. 2005). When jets are transversally resolved, the degree of linear polarization reaches a minimum towards the jet axis and increases towards the jet edges (e.g., Figure 4a in Gómez et al. 2008). Our Figure 7.1a shows that the linear polarization in HH 80-81 is perpendicular to the jet axis, and Figure
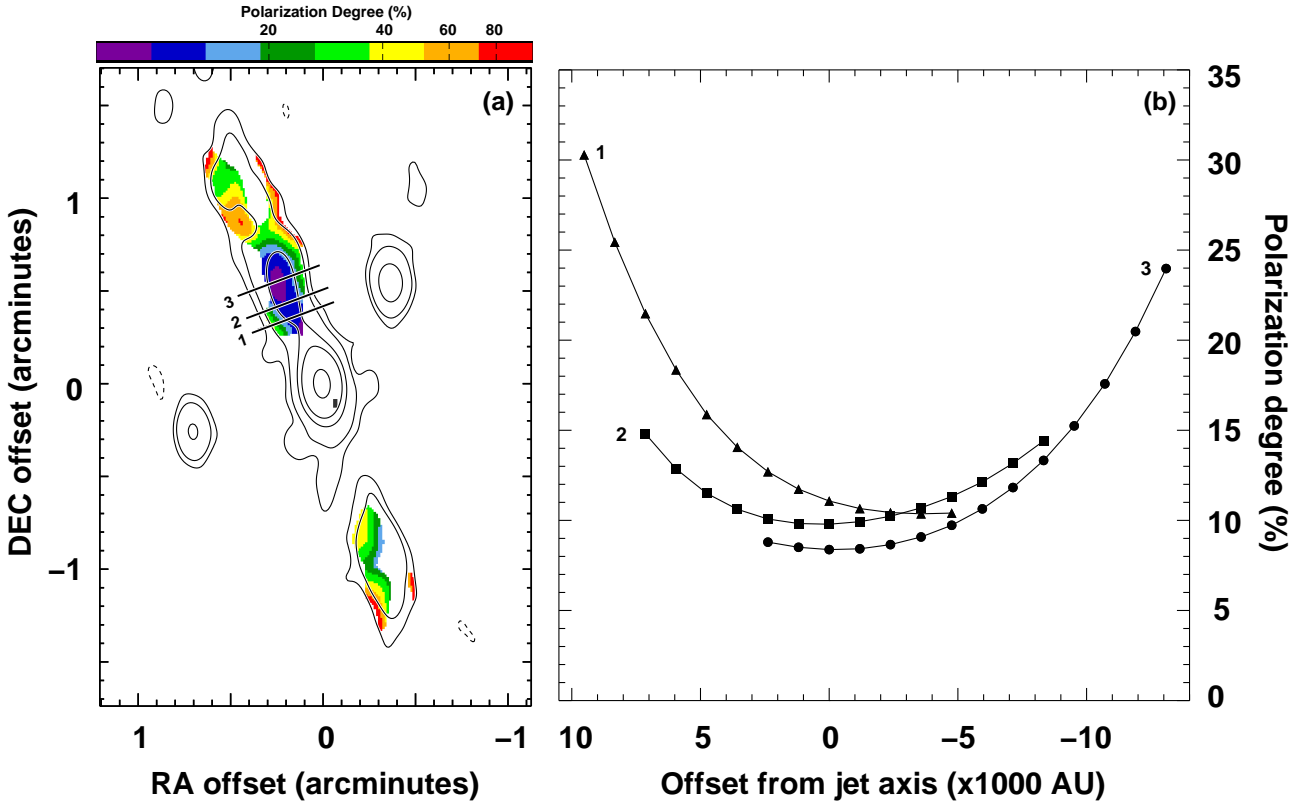
Figure 7.3 **(a)** Image of the continuum emission of the HH 80-81 jet, at 6 cm (contours) superposed with the map of polarization degree (colors), obtained as the ratio of the polarized emission over the total continuum emission. Contour levels are 40, 100, 400, 850, and 3300 μJy beam^{-1}. The color scale ranges from 5 to 100%. Black lines mark the direction of the slices shown in panel b. **(b)** Polarization degree for different slices across the jet.

7.3 shows that the degree of linear polarization increases as a function of the distance from the jet axis. In AGN jets, this configuration of the polarization has been interpreted as indicative of a large-scale helical magnetic field (Laing 1981; Lyutikov et al. 2005; Gómez et al. 2008).

Recent theoretical works (e.g. Bosch-Ramon et al. 2010), suggest that protostellar jets could be a source of gamma rays. These models postulate, as a working hypothesis, the presence of relativistic electrons in such jets. Our discovery of synchrotron emission in the HH80-81 jet demonstrate the presence of relativistic electrons in the jets from massive protostars, providing an observational ground to the theoretical conjecture, making these objects a potential target for future high-energy studies. Therefore, protostellar jets may play an unexpected important role in high-energy astrophysics.

The advent of high-sensitivity radio interferometers (EVLA, e-MERLIN, and SKA precursors) will greatly facilitate high sensitivity polarization studies in all kinds of jets, even in the weakest ones. Our detection of linearly polarized synchrotron emission in the HH 80-81 jet opens the possibility to carry out detailed studies of the magnetic field structure in the large number of jets known to be associated with young stellar objects. This would certainly be most helpful to characterize the role that magnetic fields play in the formation and collimation of protostellar jets, and to investigate the differences and similitudes with the jets driven by other

kind of astronomical objects, in order to better understand this universal phenomenon.

7.4 Conclusions

We performed sensitive VLA observations at 6 cm wavelength of the HH 80-81 jet. Our conclusions can be summarized as follows:

- We detected linearly polarized emission from the lobes of the radio jet located at ∼0.5 pc from the driving source.

- The detection of linearly polarized emission confirms its synchrotron nature, implying the presence of relativistic electrons and a magnetic field associated with the radio jet.

- We estimated a magnetic field strenght of 0.2 mG in the knots of the radio jet. The direction of the apparent magnetic field is very well aligned with the direction of the radio jet.

- We found that the polarization degree increases as a function of the distance from the jet axis. We interpret this characteristic as indicative of a large-scale helical magnetic field.

- Synchrotron emission is frequently observed in extragalactic and microquasar jets, but this is the first time that its presence in a jet from a YSO is confirmed. Our discovery represents an important step in the unification of the collimated outflow phenomena observed in many astrophysical contexts.

Bibliography

Aspin, C., Geballe, T.R. 1992, A&A, 266, 219

Beck, R. & Krause, M. 2005, Astron. Nachr., 326, 414

Bell, A.R. 1978, MNRAS, 182, 147

Blandford R.D. & Payne, D.G., 1982, MNRAS, 199, 883

Bosch-Ramon, V., Romero, G.E., Araudo, A.T., Paredes, J. M. 2010, A&A, 511, 8

Bridle, A. H., & Perley, R. A. 1984, ARA&A, 22, 319

Brocksopp, C., Miller-Jones, J. C. A., Fender, R. P., & Stappers, B. W. 2007, MNRAS, 378, 1111

Cabrit, S. 2007, Star-Disk Interaction in Young Stars (Proc. IAU Symp. 243), ed. J. Bouvier & I. Appenzeller (Cambridge: Cambridge Univ. Press), 203

Curiel, S., Ho, P.T.P., Patel, N.A., Torrelles, J.M., Rodríguez, L.F., Trinidad, M.A., Cantó, J., Hernández, L., Gómez, J. F., Garay, G., Anglada, G. 2006, ApJ, 638, 878

Curran, R. L., Chrysostomou, A. 2007, MNRAS, 382, 699

Dineen, P., & Coles, P. 2005, MNRAS, 362, 403

Draine, B. T. 2003, ARAA, 41, 241

Fanaroff, B. L., & Riley, J. M. 1974, MNRAS, 167, 31

Fish, V. L., & Reid, M. J. 2007, ApJ, 670, 1159

Garay, G., Ramírez, S., Rodríguez, L.F., Curiel, S., Torrelles, J.M. 1996, ApJ, 459, 193

Girart, J.M., Beltrán, M.T., Zhang, Q., Rao, R., Estalella, R. 2009, Science, 324, 1408

Girart, J.M., Rao, R., Marrone, D.P. 2006, Science, 313, 812

Gómez, J.L., Marscher, A.P., Svetlana, G.J., Agudo, I. & Roca-Sogorb, M. 2008, ApJ, 681, L69

Gómez, Y., Rodríguez, L. F., Girart, J. M., Garay, G., Martí, J. 2003, ApJ, 597, 414

Heathcote, S., Reipurth, B., & Raga, A. C. 1998, AJ, 116, 1940

Kigure, H., & Shibata, K. 2005, ApJ, 634, 879

Laing, R.A. 1981, ApJ, 248, 87

Lyutikov, M., Pariev, V.I. & Gabuzda, D.C. 2005 MNRAS, 360, 869

Martí, J., Rodríguez, L.F., Reipurth, B. 1993, ApJ, 416, 208

Martí, J., Rodríguez, L.F., Reipurth, B. 1995, ApJ, 449, 184

Martí, J., Rodríguez, L.F., Reipurth, B. 1998, ApJ, 502, 337

Mirabel, I. F., & Rodríguez, L. F. 1994, Nature, 371, 46

Pacholczyck, A.G. 1970, Radio Astrophysics (San Francisco: Freeman)

Pech, G., Loinard, L., Chandler, C. J., Rodríguez, L. F., D'Alessio, P., Brogan, C. L., Wilner, D. J., & Ho, P. T. P. 2010, ApJ, 712, 1403

Rodríguez, L.F., Moran, J.M., Ho, P.T.P., Gottlieb, E. W. 1980, ApJ, 235, 845

Rodríguez, L.F., Curiel, S., Moran, J.M., Mirabel, I.F., Roth, M., Garay, G. 1989, ApJ, 346, 85

Rodríguez, L.F., Garay, G., Brooks, K., Mardones, D. 2005, ApJ, 626, 953

Sarma, A. P., Troland, T. H., Romney, J. D., & Huynh, T. H. 2008, ApJ, 674, 295

Shu, F. H., Najita, J. R., Shang, H., Li, Z.-Y. 2000, Protostars and Planets IV. eds Mannings, V., Boss, A.P., Russell, S.S. (Tucson: University of Arizona Press), p. 789

Vlemmings, W.H.T., Diamond, P.J., Imai, Hiroshi 2006, Nature, 440, 58

Vlemmings, W. H. T. 2008, A&A, 484, 773

Wilner, D.J., Reid, M.J., Menten, K.M. 1999, ApJ, 513, 775

Zensus, J. A. 1997, ARAA, 35, 607

8

Conclusions

In this thesis, we present an observational, high angular resolution study of the earliest stages of the star formation process, with a special emphasis in the phenomena of jets and protoplanetary disks. This study has been performed mainly from observations carried out with the radio interferometers Very Large Array (VLA), Combined Array for Research in Millimeter-wave Astronomy (CARMA), and Sub-Millimeter Array (SMA), reaching typical angular resolutions of $0.1''$-$1''$. Specifically, we have studied five star-forming regions: two regions of low-mass star formation (L723 and HL/XZ Tau), one region of intermediate-mass star formation (NGC 2071), and two regions of massive star formation (W 75 N and HH 80-81). In the following, we summarize the main conclusions obtained.

- Our study of the radio continuum emission towards the core of the L723 star-forming region reveals a group of at least four young stellar objects (YSOs) deeply embedded within a region of only $\sim 4''$ (1200 AU) in size. Two of these objects (VLA 2A and VLA 2B) form a close radio binary whose components are separated by ~ 90 AU.

- We propose that the multipolar CO molecular outflow observed in L723 could result from the superposition of at least three independent bipolar outflows, driven by three different YSOs. Our observations suggest that VLA 2A is associated with an ionized radio jet, and that it is the driving source of the system of Herbig-Haro (HH) objects previously detected in the region, as well as of one of the bipolar CO outflows. We propose VLA 2B as the driving source of the second CO outflow. Finally, the third CO outflow, seems to be a "fossil" outflow whose exciting source has not been very active in the recent past.

- We observed the dust emission at 7 mm associated with the young star HL Tau. This emission seems to be arising in a clumpy disk with radius of ~ 25 AU. The disk shows a density gap at a radius of ~ 10-15 AU (similar to the radius of the orbit of Saturn) that may be the signpost of a growing protoplanet. Our results allow us to discard that the 1.3 cm emission feature found by Greaves et al. at a radius of ~ 65 AU corresponds to dust emission from a protoplanet.

- The young star XZ Tau, known to be a binary with 42 AU separation from previous optical/IR observations, is actually a triple star system, since our radio observations reveal that one of the two components is resolved, in its turn, into a 13 AU binary. We propose that the remarkable ejection of gas from the XZ Tau system observed with the HST may be related to a periastron passage of this newly discovered close binary system.

- We studied the centimeter (free-free) and millimeter (dust) emission of the IR sources at the center of the NGC 2071 star-forming region. We detected a new embedded YSO and we resolved the emission of IRS 2 into two components, suggesting that this source is actually a binary system.

- The centimeter emission of source IRS 1 in NGC 2071 presents an elongated morphology with protuberances at both edges. We interpret this source as a radio jet with strong interactions with the ambient medium or, alternatively, as two radio jets emerging from a close binary. Our highest angular resolution image of the core of the emission shows a hint of a double source, suggesting that a binary system could be present.

- The centimeter emission of source IRS 3 in NGC 2071 traces an ionized radio jet, while the millimeter emission traces a circumstellar disk of dust oriented perpendicular to the jet. The orientation of the millimeter emission coincides with that of the maser spots previously observed by Torrelles et al., that were also interpreted as tracing a circumstellar accretion disk. A modelling of the dust emission as an accretion disk allowed us to constrain the radius of the disk in the range 150-175 AU, the mass of the central star in the range 3-6 $M_\odot$, and the accretion rate in the range 2-4$\times 10^{-7}$ $M_\odot$ yr^{-1}.

- We studied the nature and molecular environment of five radio sources (one of them is a new detection) in the W 75N region. Our results strongly support that source VLA 3 is a radio jet associated with a YSO. We detect important changes in total flux density, morphology, and position in the source Bc, suggesting that it is not tracing an independent star but actually is a radio HH object powered by VLA 3. Its average velocity in the plane of the sky is 220$\pm$70 km s^{-1}. If our interpretation is correct, this is one of the brightest radio HH objects known so far.

- The large-scale molecular ammonia emission shows that the W 75N region contains two filamentary molecular clouds with different radial velocities. The YSOs are found at the intersection of these two filaments, which is also the hottest region. This suggests that the star formation could be triggered by the collision of the two filamentary clouds.

- Submillimeter observations of the SO molecule emission towards the massive protostar that drives the HH 80-81 jet suggest the presence of orbiting molecular gas from which we estimate a lower limit to the central binding mass of 17 $M_\odot$.

- The flux density and quadrupolar morphology of the 7 mm emission associated to the driving source of the HH 80-81 jet suggests that it is a combination of free-free emission

from the radio jet, and thermal dust emission from a perpendicular, circumstellar disk. We successfully modeled the 7 mm emission as arising from an accretion disk with a radius of 420 AU, an accretion rate of 7×10^{-6} M$_\odot$ yr^{-1}, and a mass of 14 M$_\odot$, orbiting around a 10 M$_\odot$ protostar.

- We performed sensitive observations at 6 cm wavelength of the HH 80-81 jet that reveal that the emission in the jet lobes, at $\sim$0.5 pc from the driving source, is linearly polarized. The detection of linearly polarized emission confirms its synchrotron nature, implying the presence of relativistic electrons and a magnetic field associated with the radio jet. Synchrotron emission is frequently observed in extragalactic and microquasar jets, but this is the first time that its presence in a jet from a YSO is confirmed. Our observations allow us to infer the structure of the magnetic field in the HH 80-81 jet. Theoretical models suggest that magnetic fields should play an important role in the launching, collimation, and propagation of protostellar jets. However, despite its importance, there are very few direct measurements of magnetic fields strenghts, and this is the first measure of the direction in a jet from a YSO. Our discovery represents an important step in the unification of the collimated outflow phenomena observed in many astrophysical contexts.